



**COMPUTATIONAL FLUID DYNAMICS
INVESTIGATION OF VORTEX BREAKDOWN
FOR A DELTA WING AT HIGH ANGLE OF ATTACK**

THESIS

Jacob A. Freeman, Captain, USAF

AFIT/GAE/ENY/03-3

**DEPARTMENT OF THE AIR FORCE
AIR UNIVERSITY
AIR FORCE INSTITUTE OF TECHNOLOGY**

Wright-Patterson Air Force Base, Ohio

APPROVED FOR PUBLIC RELEASE; DISTRIBUTION UNLIMITED.

The views expressed in this thesis are those of the author and do not reflect the official policy or position of the United States Air Force, Department of Defense, or the United States Government.

AFIT/GAE/ENY/03-3

COMPUTATIONAL FLUID DYNAMICS INVESTIGATION OF VORTEX
BREAKDOWN FOR A DELTA WING AT HIGH ANGLE OF ATTACK

THESIS

Presented to the Faculty

Department of Aeronautics and Astronautics

Graduate School of Engineering and Management

Air Force Institute of Technology

Air University

Air Education and Training Command

In Partial Fulfillment of the

Requirements for the Degree of

Master of Science in Aeronautical Engineering

Jacob A. Freeman, BS

Captain, USAF

March 2003

APPROVED FOR PUBLIC RELEASE; DISTRIBUTION UNLIMITED.

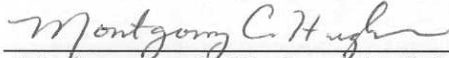
AFIT/GAE/ENY/03-3

COMPUTATIONAL FLUID DYNAMICS INVESTIGATION OF VORTEX
BREAKDOWN FOR A DELTA WING AT HIGH ANGLE OF ATTACK

Jacob A. Freeman, BS

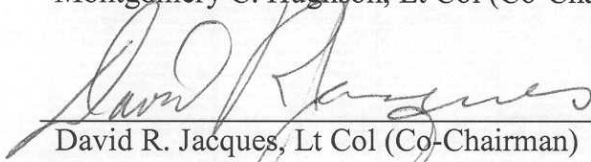
Captain, USAF

Approved:



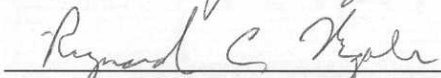
Montgomery C. Hughson, Lt Col (Co-Chairman)

10 MAR 03
Date



David R. Jacques, Lt Col (Co-Chairman)

10 MAR 03
Date



Raymond C. Maple, Lt Col (Member)

10 Mar 03
Date

Acknowledgments

I am foremost grateful to God who inspires the minds of men and women to strive for accomplishment and continual improvement and who certainly inspired me to carry this research effort to its completion. Next I owe my dear wife an immeasurable debt of gratitude for her unending patience, endearing encouragement, and unwearying care for our children during these 18 months of graduate fun.

I am indebted to my thesis advisors, Lt Col Monty Hughson who encouraged me and provided wise CFD course adjustments throughout my efforts, and Lt Col Dave Jacques who assured me these CFD results provide useful information to the collaborative, multi university-and-agency research group. I am also indebted to Lt Col Ray Maple for his computing and CFD knowledge and experience.

Lastly, Mr Cameron May (UC), Dr Effie Gutmark (UC), Dr Doug Lawrence (OU), Mr James Myatt (AFRL/VA), and Dr Jim Zhu (OU) provided me with information and guidance which were critical to this CFD research effort.

Jacob A. Freeman

Table of Contents

	Page
Acknowledgments.....	iv
List of Figures.....	vii
List of Tables.....	x
List of Symbols.....	xi
List of Abbreviations.....	xiii
Abstract.....	xiv
I. Introduction.....	1-1
Objectives and Scope.....	1-2
Delta Wing Background.....	1-4
Delta Wing Lift.....	1-5
Vortex Breakdown.....	1-7
Prediction of Vortex Breakdown Position.....	1-11
Control of Vortex Breakdown.....	1-12
Previous and Current Work on Vortex Breakdown Control.....	1-13
Computational Fluid Dynamics Background.....	1-15
Mesh Generation.....	1-16
Numerical Modeling and Computation.....	1-17
Turbulence Models.....	1-19
Solution Analysis and Evaluation.....	1-24
Previous Work on Numerical Simulation of Vortex Breakdown Control.....	1-24
II. Delta Wing Model and Computational Facilities.....	2-1
Delta Wing Model and Facilities.....	2-1
Computational Facilities.....	2-5
Hardware.....	2-5
Software.....	2-6
III. Numerical Simulation without Flow Control.....	3-1
Mesh Generation.....	3-1
Solver Parameters and Turbulence Models.....	3-23
Import Numerical Mesh.....	3-23
Solver Initialization.....	3-24
Computational Plan of Attack.....	3-30

	Page
Has It Converged Yet?.....	3-30
Determination of “Correct” Initial Conditions.....	3-33
Selection of Freestream Velocity.....	3-34
Selection of Wing Angle of Attack.....	3-34
Results.....	3-40
Effect of Model Geometry.....	3-40
Effect of Turbulence Model with Time Averaged Flow.....	3-55
Mesh Adaptation.....	3-67
Effect of Turbulence Model with Time Accurate Flow.....	3-78
IV. Numerical Simulation with Flow Control.....	4-1
Mesh Generation and Adaptation.....	4-1
Solver Parameters.....	4-4
Computational Plan of Attack.....	4-7
Results.....	4-7
V. Conclusions.....	5-1
Final Configuration.....	5-1
Conclusions.....	5-2
Future Work.....	5-3
Appendix A: Experimental Data.....	A-1
Appendix B: Traub’s Simple Prediction of Vortex Breakdown Location.....	B-1
Appendix C: Gridgen Lessons.....	C-1
Appendix D: Matrix of Transformation to Determine Jet Blowing Angles.....	D-1
Bibliography.....	BIB-1
Vita.....	VIT-1

List of Figures

Figure	Page
1.1 Flow over a Highly Swept Delta Wing with Sharp Leading Edge.....	1-4
1.2 Vortex Breakdown Visualization.....	1-8
1.3 Photographs of Vortex Breakdown in Cylindrical Water Tunnel: (a) Spiral Form, (b) Bubble Form.....	1-9
1.4 Time-Average Streamlines in Longitudinal Slice of Bubble Form Vortex Breakdown, Revealing Two-Celled Structure.....	1-10
1.5 Transverse Cross Sections of Primary Vortex for (a) No Blowing and (b) Along-Core Steady Blowing from Port at $x/c = 0.30$	1-15
2.1 Image of Half Delta Wing Test Article.....	2-1
2.2 Jet Blowing Angle: a) Azimuthal, b) Pitch Directions.....	2-2
2.3 Half Delta Wing with Boundary Layer Refresher Plate.....	2-3
2.4 Partial Isometric View of Wing and Boundary Layer Refresher Plate.....	2-4
2.5 Boundary Layer Refresher Plate and Wind Tunnel Test Section.....	2-4
3.1 Mesh Generation, Revision A: Farfield Model with One Tunnel Wall....	3-4
3.2 Mesh Generation, Revision B: Upper and Downstream Extensions.....	3-5
3.3 Mesh Generation, Revision B: Closer View of Region around Wing.....	3-6
3.4 Mesh Generation, Rev C: More Upper and Downstream Extensions.....	3-6
3.5 Mesh Generation, Revision D: Spanwise Extension.....	3-7
3.6 Mesh Generation, Revision E: Upstream and Lower Extensions.....	3-8
3.7 Mesh Generation, Revision E: Closer View of Region around Wing.....	3-9
3.8 Mesh Generation, Revision F: Parabolic Upstream Extent.....	3-10
3.9 Mesh Generation, Revision G: Hybrid Grid Including Wind Tunnel Model.....	3-11
3.10 Mesh Generation, Revision H: Enhanced Boundary Layer Resolution (Features Some Nodal Dimensions for Revision L).....	3-12
3.11 Mesh Generation, Revision I: Truncated Distance to Inlet.....	3-13
3.12 Mesh Generation, Revision J: More Truncated Distance to Inlet.....	3-14
3.13 Mesh Generation, Revision K: Wing Flush Against Wall.....	3-15
3.14 Mesh Generation, Revision L: Tunnel with Nodal Dimensions.....	3-16
3.15 Mesh Generation, Revision L: Nodal Dimensions for Tunnel Wing Section.....	3-17
3.16 Mesh Generation, Revision L: Profile View of Wing Mounted to Wall...	3-18
3.17 Mesh Generation, Revision L: Upper Surface of Wing.....	3-19
3.18 Mesh Generation, Revision L: Close-Up View of Wing Blowing Port....	3-19
3.19 Wall y^+ Values along Wing Surface in x -Direction, Rev L, Steady S-A...	3-20
3.20 Wall y^+ Values along Tunnel Walls in x -Direction, Rev L, Steady S-A...	3-21
3.21 Mesh Generation, Revision O: Boundary Layer Plate Separated from Tunnel Wall, Plus Wing and Transition Refinements.....	3-22
3.22 FLUENT <i>Define</i> → <i>Models</i> → <i>Viscous</i> Menu.....	3-25
3.23 Drag, Lift Convergence for Rev L, $\alpha = 18^\circ$, $V_\infty = 16$ m/s, Steady S-A....	3-31
3.24 Angle Selection Data at $x/c = 0.35$ (Mesh Revision L, Steady S-A).....	3-37
3.25 Angle Selection Data at $x/c = 0.55$ (Mesh Revision L, Steady S-A).....	3-38
3.26 Angle Selection Data at $x/c = 0.75$ (Mesh Revision L, Steady S-A).....	3-38

Figure	Page
3.27 Angle Selection Data at $x/c = 0.95$ (Mesh Revision L, Steady S-A).....	3-39
3.28 C_p Comparison of Initial through Mesh Revision F at $x/c = 0.35$ (Steady S-A, $\alpha = 15^\circ$, $V_\infty = 15$ m/s).....	3-41
3.29 C_p Comparison of Initial through Mesh Revision F at $x/c = 0.55$	3-43
3.30 C_p Comparison of Initial through Mesh Revision F at $x/c = 0.75$	3-44
3.31 C_p Comparison of Initial through Mesh Revision F at $x/c = 0.95$	3-44
3.32 C_p Comparison of Mesh Revision H through L at $x/c = 0.35$ (Steady S-A, $\alpha = 15^\circ$, $V_\infty = 15$ m/s (except for RevL, $V_\infty = 16$ m/s)).....	3-48
3.33 C_p Comparison of Mesh Revision H through L at $x/c = 0.55$ (Steady S-A, $\alpha = 15^\circ$, $V_\infty = 15$ m/s (except for RevL, $V_\infty = 16$ m/s)).....	3-49
3.34 C_p Comparison of Mesh Revision H through L at $x/c = 0.75$ (Steady S-A, $\alpha = 15^\circ$, $V_\infty = 15$ m/s (except for RevL, $V_\infty = 16$ m/s)).....	3-49
3.35 C_p Comparison of Mesh Revision H through L at $x/c = 0.95$ (Steady S-A, $\alpha = 15^\circ$, $V_\infty = 15$ m/s (except for RevL, $V_\infty = 16$ m/s)).....	3-50
3.36 C_p Comparison of Revs K and L (Steady S-A, $\alpha = 18^\circ$, $V_\infty = 16$ m/s).....	3-51
3.37 C_p Comparison of Revs L and O (Steady RSM, $\alpha = 18^\circ$, $V_\infty = 16$ m/s)....	3-52
3.38 Boundary Layer Effects with Refresher Plate Flush with Tunnel Wall....	3-53
3.39 Boundary Layer Effects with Refresher Plate Offset from Tunnel Wall...	3-53
3.40 Streamlines of Benign Effect of Refresher Plate Offset from Wall.....	3-54
3.41 C_p Comparison of Steady Turbulence Models at $x/c = 0.35$ (Mesh Revision L, $\alpha = 18^\circ$, $V_\infty = 16$ m/s).....	3-57
3.42 C_p Comparison of Steady Turbulence Models at $x/c = 0.55$ (Mesh Revision L, $\alpha = 18^\circ$, $V_\infty = 16$ m/s).....	3-58
3.43 C_p Comparison of Steady Turbulence Models at $x/c = 0.75$ (Mesh Revision L, $\alpha = 18^\circ$, $V_\infty = 16$ m/s).....	3-58
3.44 C_p Comparison of Steady Turbulence Models at $x/c = 0.95$ (Mesh Revision L, $\alpha = 18^\circ$, $V_\infty = 16$ m/s).....	3-59
3.45 Nondimensional Velocity Contours through Vortex Center, Predicted by Steady Turbulence Models (Mesh Revision L, $\alpha = 18^\circ$, $V_\infty = 16$ m/s).....	3-60
3.46 Blue Streamlines through Vortex and Red Vortex Core, Predicted by Steady Turbulence Models (Mesh Revision L, $\alpha = 18^\circ$, $V_\infty = 16$ m/s).....	3-62
3.47 Contours of Total Pressure over Wing Surface for Steady, Laminar Model (Mesh Revision L, $\alpha = 18^\circ$, $V_\infty = 16$ m/s).....	3-64
3.48 Contours of Nondimensional Velocity over Wing Surface for Steady, S-A Turbulence Model (Mesh Revision L, $\alpha = 18^\circ$, $V_\infty = 16$ m/s).....	3-65
3.49 Iso-Surface Helicity Contours for Steady S-A and Laminar Models (Mesh Revision L, $\alpha = 18^\circ$, $V_\infty = 16$ m/s).....	3-66
3.50 Mesh Adapt in Vortex Core (Rev L, Steady S-A, $\alpha = 18^\circ$, $V_\infty = 16$ m/s)..	3-68
3.51 Mesh Adapt - Leading Edge (Rev L, Steady S-A, $\alpha=18^\circ$, $V_\infty = 16$ m/s)...	3-70
3.52 Mesh Adaptation: Revision N (Steady S-A, $\alpha = 18^\circ$, $V_\infty = 16$ m/s).....	3-71
3.53 Nondimensional Velocity within Vortex Core for Rev L and Adaptation by Turb Viscosity Iso-Contours (Steady S-A, $\alpha = 18^\circ$, $V_\infty = 16$ m/s).....	3-70
3.54 Wing Surface-Restricted Flow for Mesh Revision L, Adaptation along Leading Edge, and Revision N (Steady S-A, $\alpha = 18^\circ$, $V_\infty = 16$ m/s).....	3-73

Figure	Page	
3.55	Contours of Total Pressure over Wing Surface for Mesh Revision L, Adaptations, and Revision N (Steady S-A, $\alpha = 18^\circ$, $V_\infty = 16$ m/s).....	3-74
3.56	C_p Comparison of Mesh Revision N and Adaptations of Mesh Revision L at $x/c = 0.35$ (Steady S-A, $\alpha = 18^\circ$, $V_\infty = 16$ m/s).....	3-76
3.57	C_p Comparison of Mesh Revision N and Adaptations of Mesh Revision L at $x/c = 0.55$ (Steady S-A, $\alpha = 18^\circ$, $V_\infty = 16$ m/s).....	3-76
3.58	C_p Comparison of Mesh Revision N and Adaptations of Mesh Revision L at $x/c = 0.75$ (Steady S-A, $\alpha = 18^\circ$, $V_\infty = 16$ m/s).....	3-77
3.59	C_p Comparison of Mesh Revision N and Adaptations of Mesh Revision L at $x/c = 0.95$ (Steady S-A, $\alpha = 18^\circ$, $V_\infty = 16$ m/s).....	3-77
3.60	Streamlines through Vortex from Unsteady RSM Turbulence Model.....	3-79
3.61	Streamlines through Vortex from Unsteady RNG k- ϵ Turb Model.....	3-80
3.62	C_p Plots from Unsteady RSM Turb Model for $t = 1.52$ - 2.08 sec.....	3-81
3.63	C_p Plots from Steady and Unsteady RSM Turbulence Models for $t = 1.52$ - 2.08 sec at $x/c = 0.95$ (Revision L, $\alpha = 18^\circ$, $V_\infty = 16$ m/s).....	3-81
3.64	C_p Plots from Unsteady S-A Turbulence Model for $t = 1.44$ - 2.00 sec.....	3-83
3.65	C_p Plots from Unsteady RNG k- ϵ Turbulence Model for $t = 1.44$ - 2.00 sec (Revision L, $\alpha = 18^\circ$, $V_\infty = 16$ m/s).....	3-84
3.66	Total Pressure Contours from Steady and Unsteady RSM Turbulence Models (Revision L, $\alpha = 18^\circ$, $V_\infty = 16$ m/s).....	3-86
3.67	Nondimensional Velocity Contours through Vortex Core from Steady and Unsteady RSM Turb Models (Rev L, $\alpha = 18^\circ$, $V_\infty = 16$ m/s).....	3-87
3.68	Nondimensional Velocity Contours through Vortex Core from Steady and Unsteady RNG k- ϵ Turb Models (Rev L, $\alpha = 18^\circ$, $V_\infty = 16$ m/s).....	3-88
3.69	Nondimensional Velocity Contours at $x/c = 0.35$ and 0.95 from Unsteady RSM Turbulence Model (Revision L, $\alpha = 18^\circ$, $V_\infty = 16$ m/s) ...	3-89
3.70	C_p Plots from Unsteady Turbulence Models at $t = 2.00$ sec.....	3-91
4.1	Mesh Adaptation to Revision L in Jet Blowing Region.....	4-3
4.2	Mesh Generation, Rev M: Views of Recessed, Angled Blowing Port.....	4-3
4.3	C_p Comparison from Velocity and Pressure Inlet at Blowing Port 1 (Revision L, Steady S-A, $\alpha = 18^\circ$, $V_\infty = 16$ m/s).....	4-6
4.4	Two-Dimensional Solution with and without Blowing at Port 1 (Steady S-A, $\alpha = 15^\circ$, $V_\infty = 15$ m/s).....	4-8
4.5	Vortex Breakdown via Streamlines for Unsteady RSM Model at No Blowing and Blowing Configurations (Rev L, $\alpha = 18^\circ$, $V_\infty = 16$ m/s).....	4-9
4.6	Effect of Port 1+2+3 Sonic Blowing on Unsteady RSM Solution (Revision L, $\alpha = 18^\circ$, $V_\infty = 16$ m/s).....	4-10
4.7	C_p Comparison of No Blowing vs Sonic Blowing at Ports 1, 2 and 3 at $t = 0.24$ sec (Revision L, Unsteady RSM, $\alpha = 18^\circ$, $V_\infty = 16$ m/s).....	4-11
4.8	Contours of Total Pressure for Cases with No Blowing and Sonic Blowing at All Ports (Revision L, Unsteady RSM, $\alpha = 18^\circ$, $V_\infty = 16$ m/s)	4-12
4.9	Effect of Port 1 Sonic Blowing on Unsteady RSM Solution for $M_\infty = 0.04$ and 0.3 (Revision L, $\alpha = 18^\circ$).....	4-13
4.10	Port 1 Sonic Blowing for $M_\infty = 0.01$ (Steady S-A, Rev L, $\alpha = 18^\circ$).....	4-14

List of Tables

Table	Page
3.1 Pressure Inlet and Reference Values for Various Freestream Velocities.....	3-27
3.2 Comparison of C_L Resulting from Various Angles of Attack.....	3-35
3.3 Comparison of C_L Resulting from Various Mesh Adaptations and Using Steady S-A Model with $\alpha = 18^\circ$ and $V_\infty = 16$ m/s.....	3-72
3.4 Comparison of C_L for Steady and Unsteady (at $t = 2.0$ sec) Turbulence Models (Revision L, $\alpha = 18^\circ$, $V_\infty = 16$ m/s).....	3-90
4.1 Comparison of C_L from Varied Inlet Specification and Port Blowing Velocity.....	4-6
A.1 Baseline C_p Data over Wing Surface, No Blowing.....	A-1
A.2 Normalized Baseline C_p Data over Wing Surface, No Blowing.....	A-2

List of Symbols

Symbol	Definition	Units
α	angle of attack	deg
α_{BD-TE}	angle of attack where vortex breakdown occurs at wing trailing edge	deg
b	wing span	cm
C_D	wing total coefficient of drag	-
CFL	Courant-Friedrichs-Lewy number	-
C_L	wing total coefficient of lift	-
$C_{L,P}$	coefficient of potential lift	-
$C_{L,V}$	coefficient of vortical lift	-
C_P	local coefficient of pressure	-
c	wing root chord length	cm
Γ	circulation ratio	-
ε	turbulence dissipation rate	m ² /s ³
ε	wing apex half angle	deg
θ	pitch angle	deg (rad)
θ_{az}	azimuthal angle of blowing jet	deg (rad)
θ_{el}	elevation angle of blowing jet	deg (rad)
K_P	potential lift constant	-
K_P'	potential lift constant, corrected for compressibility effects	-
K_V	vortical lift constant	-
K_V'	vortical lift constant, corrected for compressibility effects	-
k	turbulent kinetic energy	m ² /s ²
Λ	delta wing sweep angle	deg
λ_{max}	maximum of local flow eigenvalues	-
M_∞	freestream Mach number	-
μ	fluid viscosity	kg/m·s
P_{DYN}	dynamic pressure	Pa
P_{INIT}	initial or freestream pressure	Pa
P_{TOT}	total pressure	Pa
p	local static pressure	Pa
ρ	local fluid density	kg/m ³
ρ_∞	freestream fluid density	kg/m ³
Re	Reynold's number	-
S	wing planform area	cm ²
s	half wing span	cm
T	local temperature	K
t	time	s
Δt	time step size	s
τ_w	wall shear stress	Pa
u	x-component of jet blowing velocity	m/s

Symbol	Definition	Units
u_τ	friction velocity	m/s
V	local velocity	m/s
V_∞	freestream velocity	m/s
V_{jet}	blowing jet velocity	m/s
v	y-component of jet blowing velocity	m/s
w	z-component of jet blowing velocity	m/s
w_i	induced velocity	m/s
ϕ	roll angle	deg (rad)
x	wing position along chordwise axis	cm
Δx	spatial step size	cm
y	wing position along spanwise axis	cm
y^+	wall y-plus	-
ψ	yaw angle	deg (rad)
z	wing position along vertical axis	cm
ω	specific turbulence dissipation rate	-

List of Abbreviations

AFIT	Air Force Institute of Technology
AFRL	Air Force Research Laboratory
CFD	Computational Fluid Dynamics
DAGSI	Dayton Area Graduate Studies Institute
DNS	Direct Numerical Simulation
FV	Finite Volume
GB	Giga-Byte
GHz	Giga-Hertz
LES	Large-Eddy Simulation
LSU	Louisiana State University
MB	Mega-Byte
MHz	Mega-Hertz
RAM	Random Access Memory
RNG	Renormalization Group
RSM	Reynolds Stress Model
S-A	Spalart-Allmaras
SST	Shear-Stress Transport
TVR	Turbulent Viscosity Ratio
UC	University of Cincinnati (Ohio)
WPAFB	Wright-Patterson Air Force Base

Abstract

Using the commercially available FLUENT 3-D flow field solver, this research effort investigated vortex breakdown over a delta wing at high angle of attack (α) in preparation for investigation of active control of vortex breakdown using steady, along-core blowing. A flat delta-shaped half-wing with sharp leading edge and sweep angle of 60° was modeled at $\alpha = 18^\circ$ in a wind tunnel at Mach 0.04 and Reynolds number of 3.4×10^5 . A hybrid (combination of structured and unstructured) numerical mesh was generated to accommodate blowing ports on the wing surface. Results for cases without and with along-core blowing included comparison of various turbulence models for predicting both flow field physics and quantitative flow characteristics. FLUENT turbulence models included Spalart-Allmaras (S-A), Renormalization Group k- ϵ , Reynolds Stress (RSM), and Large Eddy Simulation (LES), as well as comparison with laminar and inviscid models. Mesh independence was also investigated, and solutions were compared with experimentally determined results and theoretical prediction. These research results show that, excepting the LES model for which the computational mesh was insufficiently refined and which was not extensively investigated, none of the turbulence models above, as implemented with the given numerical grid, generated a solution which was suitably comparable to the experimental data. Much more work is required to find a suitable combination of numerical grid and turbulence model.

COMPUTATIONAL FLUID DYNAMICS INVESTIGATION OF VORTEX BREAKDOWN FOR DELTA SHAPED WING AT HIGH ANGLE OF ATTACK

I. Introduction

While physical experimentation gives more accurate, realistic results which include nonlinear effects, it is often laborious, costly and time-consuming, and this is where computational fluid dynamics (CFD) and numerical modeling and testing enter the picture. While computer processors will likely never be fast enough to meet everyone's desires, today's numerical processing capability lends itself to more complex solvers and accordingly more accurate solutions, with lower cost and eventually less labor and time.

This research effort consists of using commercial software to generate a numerical mesh and flow field model which accurately simulates and provides quantitative and qualitative predictions comparable to results obtained from wind tunnel testing of a half delta wing at high angle of attack and low Mach number. This is part of a larger research effort to possibly eliminate the need for conventional control surfaces – namely ailerons, flaps, elevator, and rudder – by providing closed-loop control of a delta wing's vortex-dominated flight dynamics; this is done specifically by using jets on the wing surface to control vortex breakdown (discussed later in this chapter). CFD results may contribute to development of that closed-loop control system and substantially decrease efforts in wind tunnel testing. Such control potentially leads to increased lift, reduced drag, attached flow, and more favorable pressure gradients on the wing surface at

higher angles of attack, all of which enhance aircraft performance (particularly for fighter aircraft) and extend aircraft structural longevity. Fewer control surfaces also result in reduced size, weight, and radar cross-section, among other benefits. Such benefits have pertinence and obvious value to the warfighter (Gutmark et al, 2000). This thesis does not include investigation of different types of vortex breakdown control but focuses rather on the method of choice for control jets – along-core, steady blowing.

This research effort works in concert with current wind tunnel testing at the University of Cincinnati (UC), Ohio, from which aerodynamic data describing the flow field and evolution of vortex breakdown on an instrumented delta-shaped half-wing test article were obtained. Control jets along the mean trajectory of the primary vortex have been fixed to give system control (along-core blowing). For this testing, the 60-degree swept wing was fixed at approximately 15 degrees angle of attack and Reynolds number, $Re = 3.4 \times 10^5$ (based on root chord length). Effect of continuous blowing into the vortex core has been characterized and quantified for different blowing momenta. Periodic blowing is still under investigation.

Collaborative parties include UC, Ohio University (Athens), Air Vehicles Directorate of the US Air Force Research Laboratory or AFRL/VACA (Wright-Patterson Air Force Base, Ohio (WPAFB)), Dayton Area Graduate Studies Institute or DAGSI (Kettering, Ohio), and Air Force Institute of Technology or AFIT (WPAFB).

Objectives and Scope

The three objectives of this research effort were: first, develop a three-dimensional numerical mesh and flow model (specifying turbulence model, order of

accuracy, unsteady or steady flow assumption, and other model parameters) which adequately and accurately represent the physical model and wind tunnel test data and are simple enough to limit the amount of computation time for obtaining a solution; second, generate numerical data/solutions which correlate as much as possible with the experimental data; and third, vary parameters such as jet angle, jet location, jet momentum, wing angle of attack, and freestream velocity, to assess vortex breakdown control sensitivity and optimization. The CFD arm of this project was intended to enhance, not replace, the physical wind tunnel experimentation.

To summarize the results of this CFD research effort, a numerical mesh was developed and shown to be adequate though not optimal, in order to minimize computer processing time at this stage of research. While some mesh optimization was performed, more refinement is necessary for greater solution fidelity. Using this sub-optimal numerical mesh and carefully selected boundary conditions and solver parameters, none of the flow models investigated in this study, excepting the Large Eddy Simulation model for which the computational mesh was insufficiently refined and which was not extensively investigated, predicted quantitatively acceptable proximity with experimental data or qualitatively accurate representation of flow physics. Numerical modeling of vortex breakdown control using along-core blowing was the primary objective of this study. While along-core blowing was shown to have an effect in a two-dimensional CFD model, attempts to achieve similar effects in the three-dimensional case with these grid and turbulence model combinations were unsuccessful. Further investigation is required to find an optimal combination of grid and turbulence model for the numerical modeling of steady along-core blowing jets and vortex breakdown control.

Delta Wing Background

Leading-edge separation and vortex generation are aerodynamic characteristics of flow over a delta-shaped wing with an angle of attack greater than 5 degrees, sharp leading edge, and no camber (Rusak, Lamb, 1998: 2). Boundary layers from the windward (lower) and leeward (upper) wing surfaces separate at the leading edge, and these shear layers roll into a primary or leading-edge vortex pair above the upper wing surface, shown as item 1 in Figure 1.1. For a wing of geometry similar to that used for this study, the boundary layers were observed to shed at a frequency of 5 Hz (Mitchell, Délerly, 2001: 409).

The leading-edge vortex, which is characterized by high velocities and low static pressure, increases in diameter and intensity as the core follows a path downstream and

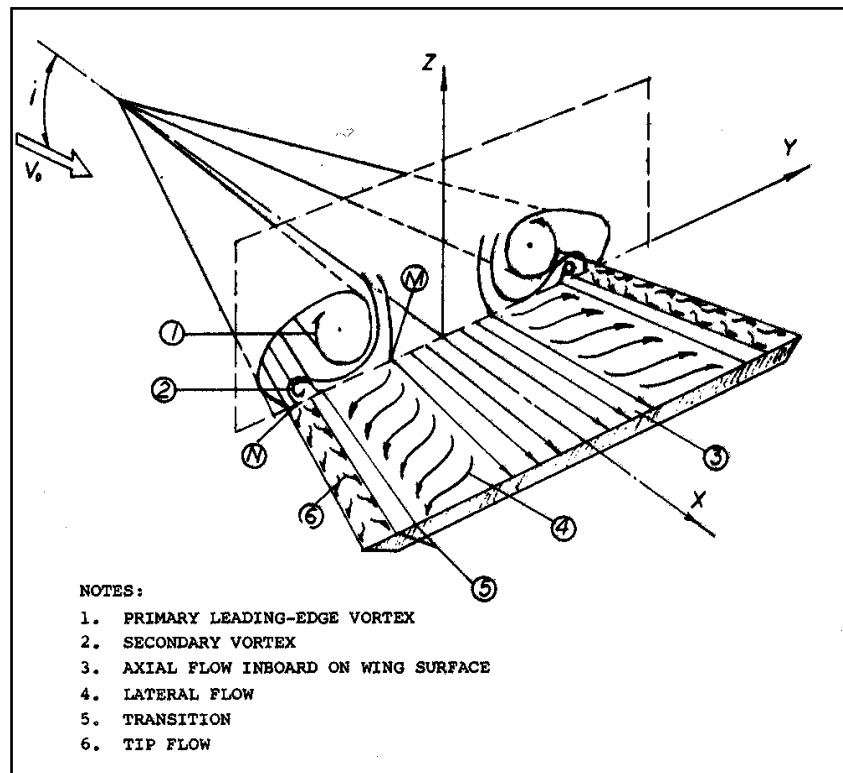


Figure 1.1 – Flow over a Highly Swept Delta Wing with Sharp Leading Edge (Hoerner, Borst, 1985: 18.3)

inboard at an angle slightly greater than the sweep angle. As the wing's angle of attack increases, the vortex axial and rotational velocities increase and the vortex core height above the wing increases and the core moves inboard (Hoerner, Borst, 1985: 18.2-3; Ekaterinaris, Schiff, 1990:1). Primary vortex generation is nearly independent of Reynolds number due to the miniscule effective length, or radius of curvature, of the leading edge; however, high Reynolds number flow does decrease vortex diameter because it effectively adds energy and velocity to the core resulting in a more tightly wrapped core (Mitchell, Délerly, 2001: 388; Novak, Sarpkaya, 1999: 831).

The primary vortex pair creates lateral, outboard boundary-layer flow on the wing surface, which collides with the primary separation and results in additional separation and a corresponding secondary vortex pair. This lateral flow and secondary vortex pair are shown as items 2 and 4 in Figure 1.1. The secondary vortex pair is weaker, is located outboard of and rotates in a direction opposite to the primary vortices. Unlike the primary pair, the secondary vortex pair's strength and size are dependent on Reynolds number. Strength of the secondary vortex is then a function of area covered by and velocity of the lateral boundary layer flow (Hoerner, Borst, 1985: 18.2; Mitchell, Délerly, 2001: 389).

Delta Wing Lift

While slender delta wings with sharp leading edges have agreeable performance characteristics in supersonic flight, the highly swept delta wing also generates additional – albeit nonlinear – lift at high angles of attack and subsonic speeds due to vortex generation and the resultant lower pressure on the leeward surface. For subsonic flow, a combination of potential and vortex lift then comprises the delta wing's total lift.

Potential lift may be determined by applying linear lifting surface theory, assuming that flow remains attached over a sharp edge, as it does over a round edge. The potential lift coefficient is

$$C_{L,P} = K_p \cdot \sin \alpha \cdot \cos^2 \alpha \quad (1.1)$$

where α is *angle of attack*, and K_p is *constant of potential lift* defined by

$$K_p = \frac{2 \cdot b \cdot \Gamma}{S \cdot V_\infty \cdot \sin \alpha} \quad (1.2)$$

where b is *wing span*, S is *wing area*, V_∞ is *freestream velocity*, and Γ is *effective circulation* or ratio of rotational and axial velocity (Kuethe, Chow, 1998: 498-500).

As for vortex lift, Polhamus' theory states that vortex formation causes the stagnation line to move from the wing's leading edge to its leeward surface, resulting in a suction force, which then increments the net lifting force (Polhamus, 1971). The vortex lift coefficient is defined by

$$C_{L,V} = K_v \cdot \sin^2 \alpha \cdot \cos \alpha = \left(1 - \frac{w_i}{V_\infty \cdot \sin \alpha} \right) \cdot K_p \cdot \sin^2 \alpha \cdot \frac{\cos \alpha}{\cos \Lambda} \quad (1.3)$$

where K_v is *constant of vortex lift* (and can be determined by the relationship in Equation 1.3), w_i is *induced velocity*, and Λ is *delta wing sweep angle* (Kuethe, Chow, 1998: 500). Total lift coefficient for a delta wing becomes the sum of the potential and vortex lift coefficients.

$$C_L = C_{L,P} + C_{L,V} \quad (1.4)$$

Polhamus' theoretical curves hold only for a freestream Mach number, $M_\infty \approx 0$.

The corrected K_P and K_V values for a subsonic Mach number become

$$K'_P = \frac{K_P}{\sqrt{1-M_\infty^2}} \quad (1.5)$$

$$K'_V = K_V \cdot \sqrt{1 + \tan^2 \frac{\Lambda}{\sqrt{1-M_\infty^2}} + \tan^2 \Lambda} \quad (1.6)$$

(Hoerner, Borst, 1985: 18.19). Compressibility effects may be neglected for this study, where $M_\infty = 0.0445$ (for $V_\infty = 15.4$ m/s). Polhamus' K_P and K_V curves, generated from Equations 1.2 and 1.3, provide a reasonably accurate analytical prediction of lift coefficient, but they overestimate for angles of attack greater than five or six degrees, due primarily to a phenomenon known as vortex breakdown, which is addressed in the next section (Guillot, 1999: 8-9). The overestimation also comes from an assumption that the vortices stream perpendicular to the wing's trailing edge, which is a valid approximation only for delta wings with sweep angle greater than 65 degrees (Wentz, Kohlman, 1971: 159).

Vortex Breakdown

As first identified in the 1950s, highly swept delta wings lose lift once they exceed a critical angle of attack, due to vortex breakdown. As previously noted for increasing angle of attack, vortex energy and velocities increase and vortex static pressure decreases (while total pressure increases), resulting in greater lift; however, as with all good things, it has its limitations. At the critical angle of attack, inner core rotation has been observed to reach about 1,000 Hz, at which point the vortex bursts or

experiences breakdown – rapidly expanding in diameter and decelerating axially and rotationally (Novak, Sarpkaya, 1999: 825). This breakdown causes a decrease in lift due to increased static pressure and because the vortex effectively separates from the wing surface and flow reattachment fails (Hoerner, Borst, 1985: 18.15).



Figure 1.2 – Vortex Breakdown Visualization
(Office National d'Etudes et Recherches Aéronautiques)

The flow field about the delta wing now assumes the following three divisions. First, approach flow is laminar and approximately irrotational. Second, flow within the breakdown region is typically stagnated, reversed, then restored to its original direction (for Reynolds number less than 6,000) with large fluctuations in velocity; it transitions to turbulent flow, and its size has been observed to be about five vortex-core diameters in length and several diameters across. Third, a follow-on vortex structure with a larger core radius continues downstream. Increasing angle of attack beyond the critical angle causes the breakdown zone to advance toward the wing apex. Reynolds number has virtually no effect on the occurrence of vortex breakdown, but it does affect the breakdown's form. (Rusak, Lamb, 1998: 2; Leibovich, 1978: 221-223; Mitchell, Détery, 2001: 386; Faler, Leibovich, 1977: 1385)

Six distinct breakdown forms have been observed and classified (Faler, Leibovich, 1977). More recent research has shown that five of these forms are transient, unstable stages of the most stable and repeatable spiral form, shown in Figure 1.3a. Further, vortex breakdown is being redefined, or more generalized, as “the transformation of a slender vortex into three-dimensional forms.... Neither a stagnation point, nor a region of reversed flow, nor the bridging of laminar-turbulent states is necessary;” neither is the flow axisymmetric or laminar (Novak, Sarpkaya, 1999: 825, 833). Reversed flow, which causes the bubble-type breakdown, shown in Figure 1.3b, and which causes the presence of two internal cells, depicted in the longitudinal cross-section of a burst vortex

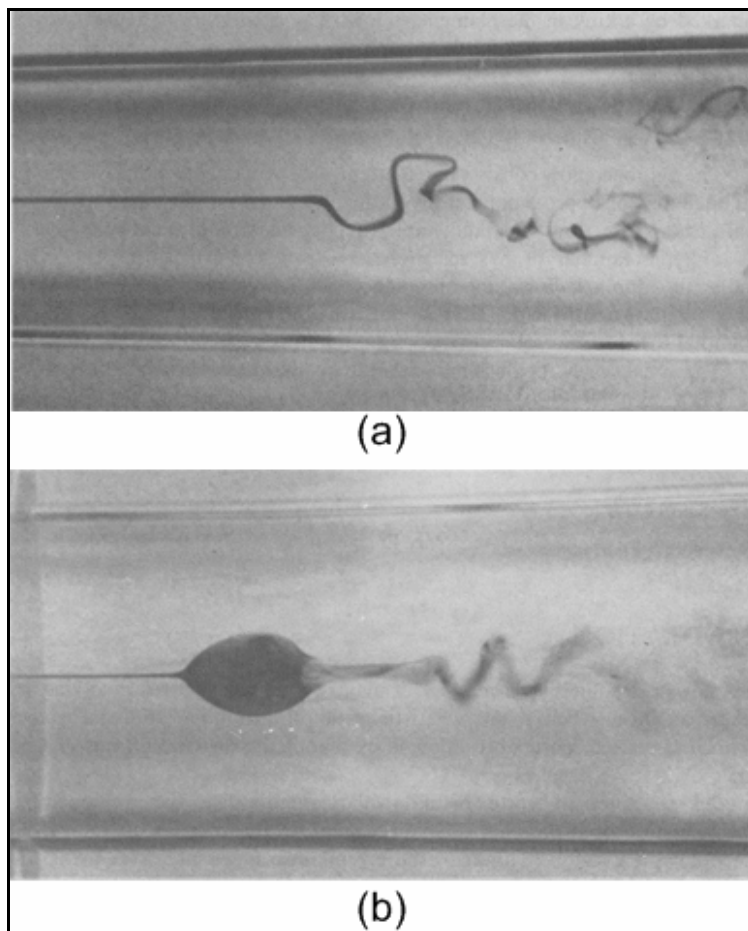


Figure 1.3 – Photographs of Vortex Breakdown in Cylindrical Water Tunnel:
(a) Spiral Form, (b) Bubble Form (Leibovich, 1978: 222)

in Figure 1.4, are not observed in high-Reynolds-number cases ($Re > 3 \times 10^5$), though this structure was predicted by the numerical models used in this investigation. A stagnation point in the axial flow may or may not be present, and when present it rotates around the centerline. Bubble-type breakdown and four other types all give way to the spiral-type vortex breakdown at high Reynolds number (Novak, Sarpkaya, 1999).

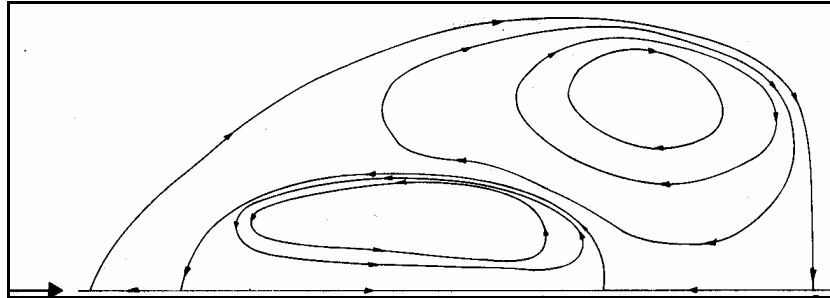


Figure 1.4 – Time-Average Streamlines in Longitudinal Slice of Bubble Form Vortex Breakdown, Revealing Two-Celled Structure (Leibovich, 1978: 230)

Flow with vortex breakdown is inherently unsteady – in vortex frequency, in vortex breakdown or stagnation point position, in vortex centerline location, in primary vortex winding, and in breakdown form or type. While the boundary-layer shedding frequency may remain relatively steady, core frequencies vary in a seemingly random, not periodic, nature. Decreased frequency is conducive to breakdown, and randomness in vortex frequency leads then to shifting of both breakdown and centerline locations. Variations in these positions range from one to several vortex core radii, and vortex breakdown position rotates about the centerline at a frequency of about 2 Hz (for low Reynolds number). Primary vortex winding has been observed in most cases to arbitrarily reverse sense. For low Reynolds number, the spiral form was observed to change to bubble form after 3-5 minutes, then back again to a spiral, further indicating the transient and unsteady nature of the bubble breakdown type. Additional unsteadiness

comes from rotation of the entire vortex/vortex breakdown form, where it rotates at about 1.5 Hz (observed for $Re = 3,120$); that frequency changes, however, with changes in rotational or swirl velocity of the vortex, which is also unsteady. For high Reynolds number ($Re \geq 2.3 \times 10^5$), the core rotates sufficiently rapidly that the human eye cannot discern the spiral breakdown but rather sees a conical shape. Thus time-averaged solutions cannot accurately depict every aspect of the highly unsteady physics of instantaneous vortex breakdown flows. (Novak, Sarpkaya, 1999; Leibovich, 1978; Faler, Leibovich, 1977)

Prediction of Vortex Breakdown Position. “The embarrassing number of different theoretical notions has not, it must be admitted, led to satisfactory understanding of the flows observed” (Faler, Leibovich, 1977: 1385). Research and hypothesizing in the ensuing 25 years have not refuted this statement, though vortex breakdown continues to become better characterized.

Numerous models have been developed to predict location of vortex breakdown, and this is not a trivial task, given the numerous unsteady and nonlinear conditions described above (Rusak, Lamb, 1998: 2; and numerous numerical studies described and cited by Rusak and Lamb). For this study, the author has chosen to use a model proposed by Lance Traub that relies heavily on empirical data rather than theoretical understanding, since no one has yet developed a theoretical model to account for all, or even the most significant, unsteady effects in vortex breakdown.

Traub’s method uses data from thirteen different experimental studies with delta wings of various sweep angles and at various angles of attack and provides equations to curve-fit the data. The simple model, which consists of stepping through three algebraic

equations, predicts vortex breakdown location within the scatter of data for four different sweep angles (Traub, 1996). The model is based on sweep angles of 65, 70, 75 and 80 degrees, and thus does not necessarily provide accurate prediction for $\Lambda = 60^\circ$ (as in this study); however, the model suffices for purposes of approximation considering that precise identification of breakdown location remains largely subjective (generally a visual observation).

Control of Vortex Breakdown

Some key observations about delta wing vortices and vortex breakdown, which pertain particularly to control of the phenomenon, include the following. Increased angle of attack and larger sweep angle produce greater rotational velocity and when the ratio of swirling to axial velocity exceeds about 1.3 breakdown occurs. Decreased rotational velocity (from decreased angle of attack) and/or increased axial velocity of the vortex cause breakdown to propagate downstream of the wing apex, or even delay breakdown. Pressure reduction also stabilizes the vortex (Faler, Leibovich, 1977: 1398; Mitchell, Détery, 2001: 386). Thus, ways to inhibit or delay vortex breakdown include decreasing angle of attack, increasing wing sweep angle, or increasing swirling and axial velocities forward of breakdown position and within the constraining ratio noted above. Conversely of these abet vortex breakdown.

Controlling vortex breakdown, whether delaying or encouraging it, has numerous positive effects on aircraft handling and performance. By delaying or preventing it, body lift increases, drag decreases, flow remains attached (or re-attaches), favorable pressure gradients abound, structural cyclic fatigue abates, and aircraft stability is augmented. By provoking vortex breakdown on one wing, the resultant asymmetry may enhance the

maneuvering performance of a combat aircraft (Mitchell, Délerly, 2001: 387-388). For these reasons, a significant number of control studies have been completed over the past four decades.

Previous and Current Work on Vortex Breakdown Control. Again, since this effort does not include investigation of different types of breakdown control, following is a summary of methods used, focusing more detail on the method of choice for control jets – along-core, steady blowing.

Two general categories of vortex breakdown control are via mechanical structures and via pneumatic methods. Anthony Mitchell and Jean Délerly provide an excellent summary of research efforts in their recent article in *Progress in Aerospace Sciences* (Mitchell, Délerly, 2001). Mechanical structures include “strakes, canards, fillets, leading-edge extensions, flaps and vortex fences,” while pneumatic methods include steady and periodic “spanwise blowing, tangential blowing, leading-edge blowing, along-the-vortex-core blowing, trailing-edge blowing, leeward surface suction, leading-edge suction, and suction along the vortex core” (390). While mechanical devices are generally more robust, they add weight and drag; and while pneumatic techniques have shown greater benefit than mechanical devices, they are more subject to contamination (particles clogging the injection/suction ports) (391-395).

Suction and blowing both provide the same result – to reduce static pressure along the vortex core, increasing its stability – though they accomplish it differently. Studies have shown that each suction or blowing technique enhances aerodynamic performance of the wing, but “none of these techniques has clearly demonstrated a superior efficiency or effectiveness in controlling either the vortical flow structure or the vortex breakdown

location” (415). Nevertheless, the more promising of the pneumatic techniques and more subject to current research are along-core and periodic blowing (395-416).

Along-core blowing, whose magnitude is a function of blowing mass flow rate and freestream velocity, adds momentum to the vortex core and increases both axial and rotational velocities, allowing for a more stable pressure gradient along the wing surface and for a more steady vortex core. In most investigations, steady blowing has required a great deal of energy to affect the vortex breakdown location, but a recent study at Louisiana State University (LSU) has shown that breakdown location manipulation may be accomplished with smaller flow rates (Guillot, 1999). For even less mass addition, as with pulsed blowing, vortex breakdown delay and lift augmentation have been demonstrated. Since periodic blowing appears to be most effective at the natural shedding frequency of the shear layers, difficulty lies in identifying and matching this unsteady characteristic (Mitchell, Délery, 2001: 409-411, 415).

Figure 1.5 shows flow visualization results from the LSU study without (column a) and with along-core steady blowing (column b) from a surface port at $x/c = 0.30$ and angled to intersect the vortex core centerline (Guillot, 1999: 54). In column a of the figure, the vortex core expands or bursts aft of $x/c = 0.30$, and the core progressively becomes more turbulent downstream of that point; column b shows the effect of along-core blowing into the vortex, where the vortex core maintains its integrity.

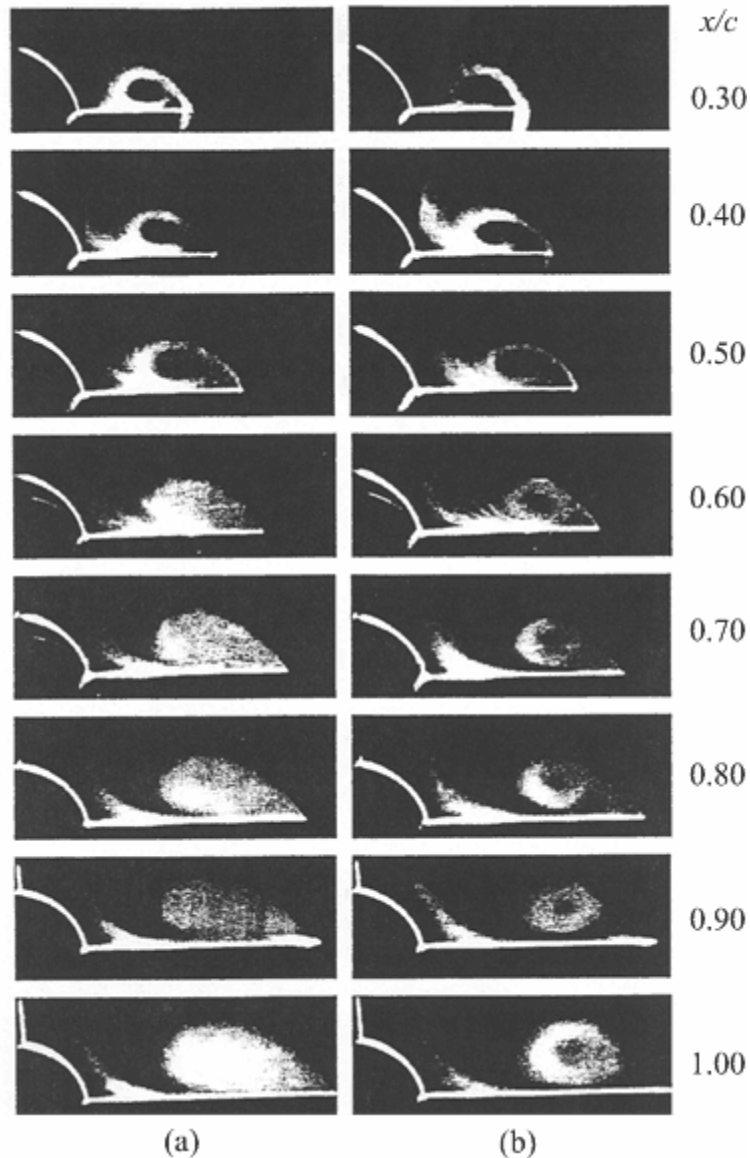


Figure 1.5 – Transverse Cross Sections of Primary Vortex for (a) No Blowing and (b) Along-Core Steady Blowing from Port at $x/c = 0.30$ (Guillot, 1999: 54)

Computational Fluid Dynamics Background

Conservation of mass, momentum and energy constitute the equations of fluid motion, and the Navier-Stokes equations represent those conservation laws in partial differential form (Hoffman, Chiang, 2000.I: 274). These partial differential equations, in integral form, are then approximated as finite-volume (FV) expressions and reformed into

algebraic equations to allow for numerical computation within a specified physical/computational domain (Hoffman, Chiang, 2000.I: 358). To reduce computational time and complexity, simplifications of these governing equations can include assuming one- or two-dimensional flow, inviscid flow, steady flow, incompressible flow, and/or first-order solution accuracy. For this study, cases of interest included preliminary use of simplified forms, but ultimately focused on three-dimensional, viscous, second-order accurate, compressible, unsteady flow – as vortices and vortex breakdown are inherently unsteady.

Analysis of fluid flow using computational fluid dynamics (CFD) is an iterative process consisting of three basic steps: mesh generation, numerical modeling and computation, and solution analysis and evaluation.

Mesh Generation

Mesh or grid generation consists of creating a set of grid points along the boundaries and throughout the domain of interest. For simple three-dimensional geometries, a structured mesh may be generated, where all volumetric cells are hexahedrons. Often the physical domain involves geometry which is not rectangular, such that coordinate transformation must be performed to convert to a computational domain which is rectangular for a structured mesh approach. However, since few problems involve such simple geometry, an unstructured mesh approach is often preferred, where volumetric cells may be tetrahedrons, pyramids, or any three-dimensional polyhedrons, and where the domain is already in a computationally suitable form, such that no transformation is necessary (Hoffman, Chiang, 2000.II: 356-357). In some cases and for this effort, structured and unstructured regions of a domain may be

combined into a hybrid mesh. While unstructured meshes require greater computational effort and memory, fewer cells are generally required within a given domain.

Numerical Modeling and Computation

Once a suitable mesh has been generated, a computational algorithm numerically solves the FV equations for fluid values at each volumetric cell center, from which these values can be interpolated to cell faces (FLUENT, 2001: 22.2). Computations may cease once the solution has converged or has come to fully developed flow. Normally, convergence is achieved when the FV approximation approaches the partial derivative solution, and may be detected when error residuals (function of difference between previous and current computed values) are sufficiently reduced, when some integrated value (such as lift coefficient) becomes steady for a steady-state solution, and/or when flux (such as mass flow) is conserved (Hoffman, Chiang, 2000.I: 26; FLUENT, 2001: 22.16).

Solution accuracy and convergence are a function of temporal step size, flow model (for example, order of accuracy, under-relaxation, viscous model, and equation coupling), and mesh. Steady-state solutions converge more quickly with local time-stepping, where step size (Δt) is determined and updated based on local values within each FV of the domain. Local time-stepping also maintains greater solution stability within the domain. However, time accurate or unsteady solutions must use either a global time step or a combination of global and local time steps, where the time step must lend stability to the numerical scheme and suit the physical requirements related to the problem (such as to not exceed the vortex frequencies if they are to be accurately

evaluated in time). Time step may be defined as either one global value or by the following,

$$\Delta t = (CFL) \cdot \frac{\Delta x}{\lambda_{\max}} \quad (1.7)$$

where Δx is *spatial step size*, λ_{\max} is *maximum of local eigenvalues* (function of flow velocities in three dimensions, fluid density, and speed of sound in air; refer to FLUENT User Guide for further detail), and *CFL* is *Courant-Friedrichs-Lewy condition* (a specified value). In the combined case (used for unsteady solutions in this study), the solution is driven to convergence at each global time step or physical time level. (Hoffman, Chiang, 2000.II: 146-149, 266; FLUENT, 2001: 22.4.3-4)

Flow model order of accuracy in space and time also affects the solution accuracy. While the governing equations of fluid mechanics may be discretized only spatially for steady-state solutions, they must be discretized both temporally and spatially for time accurate solutions. First-order discretization gives an accurate solution for cases with simple physical and flow geometries, but for most cases second-order accurate solutions are more desirable (or required). Second-order discretization requires values at previous, current and next time steps for an unstructured mesh. The under-relaxation parameter scales or controls updated values for each iteration, thereby stabilizing the solution but slowing convergence. An implicit scheme (where all flow variables are solved simultaneously) and coupled equations lead to convergence in fewer iterations than an explicit scheme and segregated equations, respectively, but require greater computational resources and cannot normally be run in a parallel computing fashion. Current state-of-the-art flow solvers use dual time-stepping, implicit-explicit schemes to

take advantage of parallel computing. (FLUENT, 2001: 22.2.8, 22.4, 22.7.1, 22.9; Hoffman, Chiang, 2000.II: 290)

CFD solutions are highly mesh-dependent. A tradeoff must be made between overall computation time and solution accuracy; an extremely fine mesh will typically give an accurate solution but will be computationally time-intensive, while a coarse mesh computes quickly but may give an inadequate or inaccurate solution. An intermediate approach is to use a coarse mesh which may be adapted by redistributing nodes or by adding more nodes to a particular region for better resolution. For this case, FLUENT's flow software provides the ability to use a roughly converged solution to determine where best to refine or coarsen the mesh, based on appropriate flow gradients, distance from the wall, user-specified volumetric regions, etc. The flow solver then continues toward convergence and a more accurate solution with this modified or adapted mesh, thus optimizing solution accuracy and computational efficiency (FLUENT, 2001: 23.1).

Turbulence Models. Turbulence is an age-old problem that is relatively easily observed, as noted by wise King Solomon, but not easily modeled. He wrote, “The wind goeth toward the south, and turneth about unto the north; it whirleth about continually, and the wind returneth again according to his circuits” (*The Holy Bible*, 1979: Ecclesiastes 1:6).

While direct numerical simulation (DNS) best predicts turbulence effects, its very fine mesh requirements remain too computationally demanding – given today's computing capabilities – for problems with complex flow. The onus is on the user to select a turbulence model which gives the most accurate approximation for the flow physics in a specific application. Thus for this application, Ekaterinaris and Schiff

observed that “bursting point location and the extent of the vortex breakdown region are seen to be sensitive to the turbulence modeling” (61). As part of this study, numerous turbulence models were investigated. These models include Spalart-Allmaras (S-A), Renormalization Group (RNG) k - ϵ , Reynolds Stress (RSM), and Large-Eddy Simulation (LES), as well as comparison with inviscid and laminar flow solutions. It must be noted that in general these turbulence models have been validated for cases with simple flow features and simple model geometry (Kral, 1998: 484); while this case involves simple model geometry, the flow field is complex so careful attention must be afforded in selecting an appropriate model.

While it is included for comparison and has shown to predict a relatively accurate solution, the laminar case underestimates the strength of the primary and secondary vortices and certainly inaccurately models the region of high turbulence within and following vortex breakdown (Ekaterinaris, Schiff, 1990: 61; Murayama, Nakahashi, Sawada, 2001: 1311).

Designed for aerospace applications, the one-equation S-A turbulence model solves the transport equation for turbulent or kinematic eddy viscosity. It predicts solutions best for cases involving wall-bounded flow and adverse pressure gradients, both of which are part of this study. The S-A model has great computational efficiency and has been shown to converge on a solution more quickly even than algebraic turbulence models which encounter discontinuities, because it predicts a continuous turbulence viscosity distribution (Mani, Willhite, Ladd, 1995; Kral, 1998: 535). While it is also well suited for meshes with unstructured or hybrid boundary layer, the S-A model was designed for problems with low Reynolds number, attached flow and mild turbulence and

is still relatively new in its validation and verification (FLUENT, 2001: 10.2.4; Spalart, Allmaras, 1992:1, 15). However, it becomes “very complicated and often ambiguous” when attempting to model physics of turbulent flow in a flow field with significant flow separation and unsteady behavior (Hoffman, Chiang, 2000.III: 54).

Other numerical investigations have shown that the S-A turbulence model accurately predicts flow properties for external subsonic, transonic and supersonic attached flow, and for supersonic nozzle and impinging jets flow. It predicted a solution more accurate than the two-equation k - ϵ model for supersonic flow over a flat plate. While the S-A model has successfully predicted qualitative flow physics, its quantitative predictions are considerably less accurate, and it poorly models flow in turbulent wake regions, in boundary layers, and over a backward-facing step or flat trailing edge. (Snyder, Spall, 2000; Kral, 1998; Mani, Willhite, Ladd, 1995; Spalart, Allmaras, 1992: 19)

Accepted nearly industry-wide as an accurate turbulence model because of its strong empirical basis, the two-equation k - ϵ model (k is *turbulent kinetic energy*, modeled theoretically; ϵ is *turbulent dissipation rate*, modeled empirically) solves two independent transport equations and accounts for compressibility effects. This model is valid only for completely turbulent flow, not one with laminar flow in various regions, but the RNG modification reportedly caters to time-dependent turbulent vortex shedding (FLUENT, 2001: 10.2.5, 10.2.11, 10.4.1). Numerical studies have shown that the k - ϵ model more accurately predicts flow in a compressible, turbulent field than does the S-A model and that it is well suited to cases with supersonic attached flow, internal flow and external turbulent boundary layers. Disadvantages include poor accuracy for cases with vortical

and rotating flow and with flow in non-circular ducts and turbulent wakes; also the k- ϵ model requires about 10% more computational memory and 2-7 times more processing time than does the S-A model. (Kral, 1998; Kral, Mani, Ladd, 1996; Versteeg, Malalasekera, 1995: 75)

Similar to k- ϵ is the k- ω turbulence model, which solves the transport equations for k and ω , or *specific dissipation rate*. FLUENT provides two versions of the k- ω model: the Standard k- ω model accounts for effects from compressibility and low Reynolds number; the Shear-Stress Transport (SST) k- ω model accounts for the principal turbulent shear stress and combines benefits of both k- ω and k- ϵ models within the boundary layer (FLUENT, 2001: 10.5, 10.5.1-2). In computational terms, both k- ω models require memory comparable to that required by the k- ϵ model, but the SST k- ω model's processing time per iteration is on the order of that required for S-A computations – due to its limiter on turbulent viscosity. Both k- ω models predict relatively accurately supersonic external flow with an attached boundary layer; the SST version does well also with supersonic separated flow and nozzle flow, but in these cases it does not predict better than does the S-A model. The SST k- ω model poorly predicts flow that is subsonic and highly separated (Kral, 1998: 484, 535-538). Since the k- ω models are only a small improvement over the k- ϵ model, largely comparable to the S-A model, and inferior to the RSM model, they were not evaluated in this research effort.

More complex than the other models, the seven-equation RSM solves seven transport equations – five for the Reynolds stresses and two for k and ϵ . It accounts for flow rotation, compressibility, curved streamlines, the anisotropic or directional characteristic of turbulence in swirling flows, and it does not assume that “turbulent

stresses respond immediately to changes in the mean strain rate” (Kral, 1998: 483). However, it is limited by potential inaccuracies of the empirical ε model, assumes local homogeneity and equilibrium in turbulence, and requires 50-60% more computation time per iteration and 15-20% more memory than the other turbulence models (FLUENT, 2001: 10.2.10-11; Kral, 1998; Versteeg, Malalasekera, 1995: 78). For steady, incompressible flow at $Re = 8.0 \times 10^5$, the RSM model was verified as more quantitatively accurate than the S-A model for flow within the boundary layer and the turbulent vortex structure (Snyder, Spall, 2000).

While the S-A, k- ε and RSM turbulence models use Reynolds-Averaged Navier-Stokes equations, which model mean flow quantities and which generally require less computational time (for steady and unsteady flows) than DNS, LES uses an alternative filtering approach to solving for the flow variables (unsteady flow only). By appropriately modifying the Navier-Stokes equations, turbulent eddies smaller than the filter (or grid cell size) are removed and approximated with an isotropic model, while the large eddies are directly resolved through the discretized Navier-Stokes equations. Small eddies are more universal and depend less on geometry and are thus more easily modeled, whereas large eddies are specific to a problem’s geometry and boundary and initial conditions. Disadvantages of LES include: it requires a fine numerical mesh, which results in high computational cost; along the walls, the mesh must be particularly fine, since LES basically uses direct numerical simulation in this region; it has not been well tested for cases with other than simple geometries; and it does not account for compressible flow, though it allows for variable density. This study used the Smagorinsky-Lilly Model, which is accurate in many cases for flow with high Reynolds

number (that is, flow in regions other than near walls) to model the small or subgrid turbulent eddies. (FLUENT, 2001: 10.2.1, 10.7, 10.7.2; Mathieu, Scott, 2000: 340-353)

Solution Analysis and Evaluation

Once convergence or fully developed flow is realized, solution data may be analyzed and evaluated using any number of visualization software packages. In this case, variables of interest include pressure, velocity, vorticity (rotation measurement), helicity (dot product of vorticity and velocity vector), and turbulence. Flow visualization with such software may be accomplished virtually instantaneously, whereas wind tunnel flow visualization requires injection of smoke or dyes and use of lasers, high-speed cameras, etc., and consumes a good deal of time and resources.

If convergence has not been achieved or if the solution is otherwise deemed inaccurate, possible actions include executing more iterations with smaller required residuals, decreasing the CFL number or time step, decreasing the under-relaxation parameter(s), feeding a converged first-order solution into a second-order computation, refining the mesh, and/or selecting a different turbulence model.

Previous Work on Numerical Simulation of Vortex Breakdown Control

Other numerical studies of vortex breakdown typically assume axisymmetric, laminar, incompressible, steady flow at low Reynolds number (Murayama, Nakahashi, Sawada, 2001; Novak, Sarpkaya, 1999: 825; Ekaterinaris, Schiff, 1990; Leibovich, 1978: 243; and numerous studies described and cited in these sources). While some studies have investigated unsteady flow, one expert who has researched and investigated vortex breakdown for more than 30 years, stated, "...there has not yet been a turbulence model capable of dealing with nonisotropic turbulence in swirling flows ... subjected to

streamline curvature and strong radial pressure gradients” (Novak, Sarpkaya, 1999: 825, 834).

While these studies have, in general, closely matched numerical and experimental results, no numerical study has investigated the specific set of conditions, particularly with along-core blowing, applied to this specific geometry. Also, the studies referenced above modeled the delta wing in farfield, freestream conditions, as opposed to including the wind tunnel geometry as part of the model.

II. Delta Wing Model and Computational Facilities

The scope of this branch of the overall research effort does not include wind tunnel test article data generation and collection, but the physical configuration at UC is described hereafter to show correlation with the numerical representation.

Delta Wing Model and Facilities

The model, pictured in Figure 2.1, is a half-span (port side), aluminum delta wing with sharp leading edge, sweep angle of 60 degrees, flat trailing edge, and no camber. It is 1.27 cm thick with 30-degree leading edge bevel and has a removable top plate and hollow interior to accommodate pressure sensor instrumentation and tubing for the blowing ports. Root chord length (c) measures 34.3 cm and half-span (s , where span, $b =$

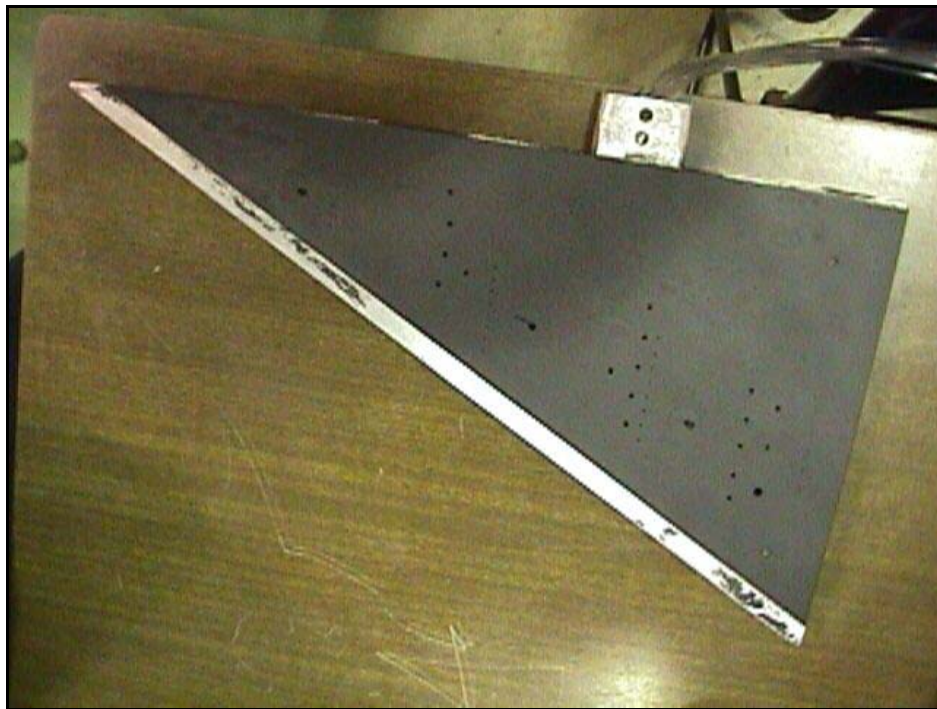


Figure 2.1 – Image of Half Delta Wing Test Article

2s) is 19.8 cm. Wing upper surface (or planform) area is 339.57 cm² and aspect ratio is 2.31. The leading edge is not perfectly sharp, as it appears to have been ground slightly. Further, the wing is many years old and thus has numerous small abrasions, nicks and dents along the leading edge and over the entire surface.

The three blowing ports, located chordwise at $x/c = 0.30, 0.60$ and 0.80 , and spanwise at $y/s = 0.21, 0.41$ and 0.54 were positioned based on visual placement under the observed vortex core centerline. Each blowing port has a straight nozzle drilled in a circular disk, where nozzle dimensions are 0.9525 cm (3/8 in.) in length and 0.0794 cm (1/32 in.) in diameter. Based on results from the study at Louisiana State University, using the same wing, relative optimum blowing angles were established for pitch and azimuthal directions, where pitch angle is 35 degrees, measured from the wing surface, and azimuthal angle is 155 degrees, measured counter-clockwise (positive) from a line parallel to the wing's root, as shown in Figure 2.2 (Guillot, 1999: 21-22). Each blowing port is connected, via 6 m of rubber hose, to a source of compressed air at available values of 586, 483, 345 or 207 kPa (85, 70, 50 or 30 psig, respectively).

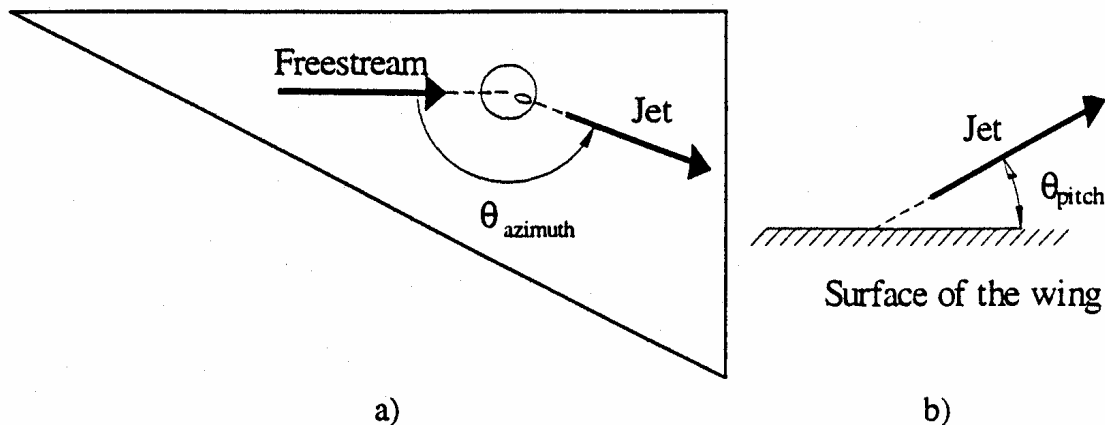


Figure 2.2 – Jet Blowing Angle: a) Azimuthal, b) Pitch Directions (Guillot, 1999: 21)

Thirty pressure taps on the wing surface are located in straight spanwise lines and in chordwise positions along $x/c = 0.35, 0.55, 0.75$ and 0.95 . Tubes from each pressure tap and blowing port exit the test article through a mounting bracket 3.81 cm (1.5 in.) long and 1.27 cm (0.5 in.) thick, with rounded front and back ends of radius 0.635 cm (0.25 in.). Static pressure measurement error on the wing surface is on the order of a few Pascal, based on 0.8 to 0.9 Pa instrument error (maybe more since the transducers are about two decades old), in addition to tube losses. Each pressure measurement was time averaged from 5 seconds of data collected at 100 Hz sampling rate (May, 2002.a).

The wing is mounted at an angle of attack equal to approximately 15 degrees and flush to a boundary layer refreshing plate, 0.635 cm thick, 45.72 cm (18 in.) long, and 30.48 cm (12 in.) high, shown in Figures 2.3 and 2.4. This plate has a 45 -degree bevel and sharp leading edge, where the wing is mounted to the underside; the wing apex is located about 5 cm downstream of the refresher plate's leading edge. The plate is offset from the wind-tunnel wall by 1.27 cm, which effectively compresses into this gap the

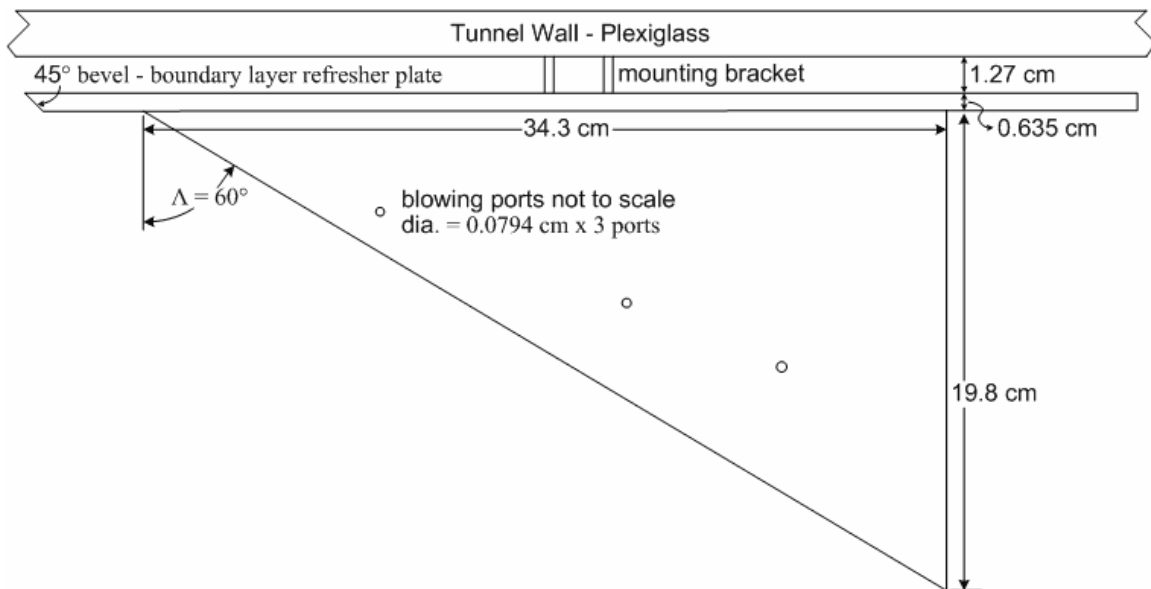


Figure 2.3 – Half Delta Wing with Boundary Layer Refresher Plate

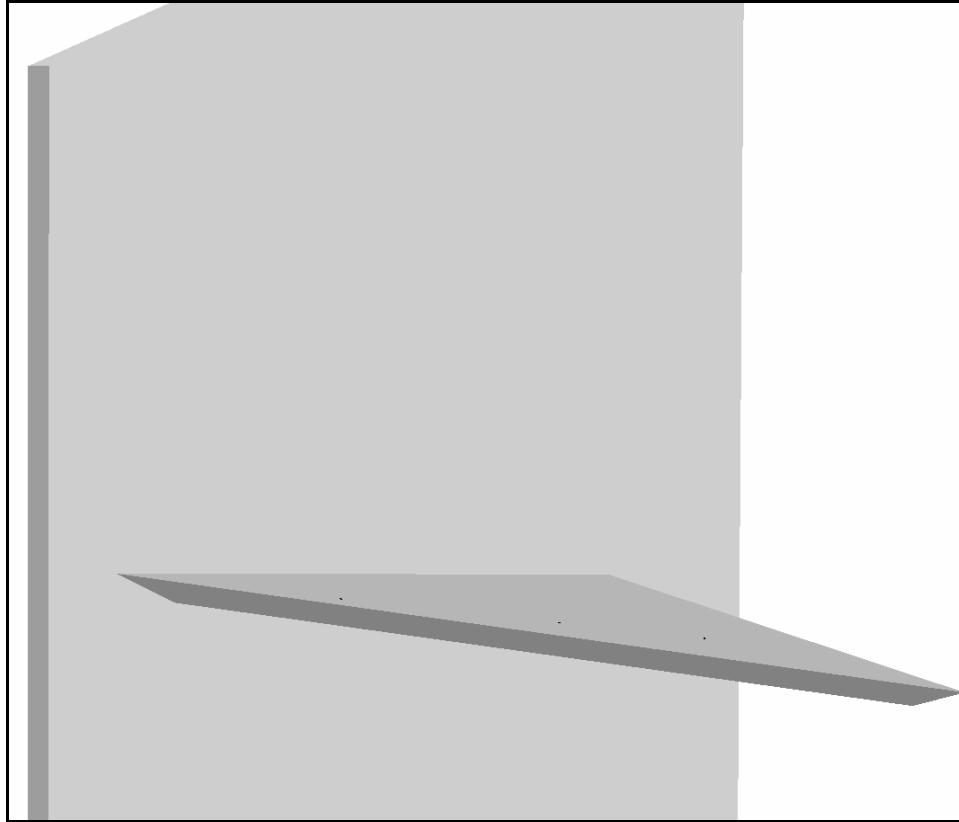


Figure 2.4 – Partial Isometric View of Wing and Boundary Layer Refresher Plate

wind-tunnel wall boundary layer and gives laminar freestream conditions at the wing apex. This serves as an approximation of freestream conditions in unconfined flow.

Wind tunnel test section dimensions are 60.96 cm (24 in.) high by 60.96 cm wide. The test article is mounted about 200 cm downstream of the relatively steady and evenly distributed flow inlet and about 300 cm upstream of the wind tunnel exit/recirculation chamber. Figure 2.5 shows tunnel and boundary layer refresher plate dimensions.

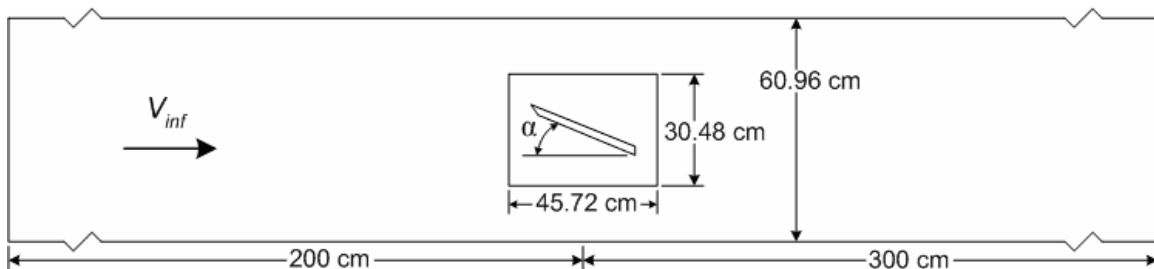


Figure 2.5 – Boundary Layer Refresher Plate and Wind Tunnel Test Section

Test data were generated in a UC lab, where ambient pressure was measured at 99.56 kPa and ambient temperature was 298 K. Dynamic pressure measurements inside the wind tunnel and upstream of the wing averaged about 143 Pa (May, 2002.a). These pressure measurements correspond to an air density of 1.208 kg/m³ and freestream velocity of 15.4 m/s (U.S. Government Printing Office, 1976), which then gives a Reynolds number of 3.56×10^5 , based on root chord length, and a total temperature of 298.12 K inside the wind tunnel. Refer to Appendix A for raw data.

Computational Facilities

Computational research and investigation for this study was performed in the Computational Fluid Dynamics Laboratory (CFD Lab) of the Department of Aeronautics and Astronautics and in the UNIX Computer Lab, both of the Graduate School of Engineering and Management, Air Force Institute of Technology, using the following hardware resources and commercially available software.

Hardware

Mesh generation, early flow solutions and most post-processing were performed on Dell Precision 530 workstations, using Redhat Linux 7.2 or 8.0 operating systems. Two of the three available workstations in the CFD Lab feature dual 1.4 GHz Pentium 4 Xeon processors, 512 MB of RAM and 37 GB of hard disk space, and the third features dual 2.3 GHz Pentium processors, 2,048 MB of RAM and over 120 GB of disk space. They are connected to a 16-node Beowulf processing cluster (also known as the Hydra cluster) by Aspen Systems, Inc. (<http://www.aspsys.com>), where each node has two 1.2 GHz Athlon processors and 1,024 MB of RAM. Computing was also performed on a 64-

node Beowulf cluster (known as the Aspen cluster), where each node has two 1.0 GHz processors and 1,024 MB of RAM. The Aspen cluster was accessed remotely from a Sun Ultra 80 UNIX workstation, using a Sun operating system and featuring 2,048 MB of RAM and 18 GB of hard drive space. Additional post-processing was performed on a Dell Precision 530 workstation, using a Microsoft Windows 2000 Professional operating system and featuring a 1.5 GHz Pentium 4 processor and 512 MB of RAM.

Software

Commercially available software was used for mesh generation, flow initialization and computation, and post-processing. The hybrid mesh, or combination of structured and unstructured grids, was generated using Gridgen Version 14.02 (Pointwise, Inc., <http://www.pointwise.com>). All flow computations were performed with FLUENT Version 6.0.20, which is a general-purpose flow solver (FLUENT, Inc., <http://www.fluent.com>). Since it uses a finite-volume discretization scheme, FLUENT is well suited for solving unstructured or hybrid domains. FLUENT has numerous options for computational schemes, including steady or unsteady flow, first- and second-order spatial and temporal accuracy, incompressible or compressible flow, coupled or segregated equation solver, explicit or implicit numerical scheme, and inviscid or viscous flow, featuring each of the turbulence models discussed in Chapter 1 (FLUENT, 2001). Results from and/or justification for selected options in FLUENT follow in Chapter 3. Post-processing was done both with FLUENT and with FIELDVIEW Version 8.0 (Intelligent Light, <http://www.ilight.com>). FLUENT has an option to export solution data in FIELDVIEW format. Post-processing included generating plots, visualizing isometric contours of various flow variables, generating multiple two-dimensional slices in one

image, creating streamlines, surface flow and surface pressure contours, and identifying vortex core centerline.

III. Numerical Simulation without Flow Control

As discussed in Chapter I, tackling a CFD problem consists of three iterative steps – mesh generation, numerical modeling and computation, and solution analysis and evaluation. As the process is iterative, it also involves mesh refinement and/or adaptation and possible variation of solver parameters, flow models, and initial and boundary conditions. Discussion and comparisons follow, to include parallel computing. Chapters III and IV address these steps for this problem, where Chapter III discusses the baseline case (half delta wing with no along-core blowing) and Chapter IV presents an along-core blowing case.

Mesh Generation

Since the half delta wing test article is a number of years old and was passed from one university to another, the original technical drawing was no longer available resulting in possibly inaccurate measurements of wing dimensions and blowing port locations. Furthermore, the wind tunnel setup was no longer fully assembled or being used during the time of initial mesh development, such that some details of the setup were initially absent, including existence of the boundary layer refreshing plate and precise angle of attack and freestream velocity measurements. Thus the initial mesh and its first 10 revisions all lack inclusion of a refreshed boundary layer about 5 cm upstream of the wing apex. However, some experience was gained in passing through the various mesh iterations, so they are included here for pedagogical edification. Mesh details, including

number of node points, faces and cells, are discussed qualitatively (or approximately) until discussion of the final configuration.

While structured grids traditionally give more accurate solutions for relatively simple geometries, unstructured meshes may achieve a sufficiently accurate solution with fewer cells, less construction effort and hence less computation time. After significant effort to create a structured grid, to include meshing discontinuities caused by introduction of blowing ports, it was determined an unstructured approach would be quicker, more easily revised as needed and would likely provide acceptable results.

The initial mesh consisted of the half delta wing placed flush against a wall which extended one chord length downstream of the trailing edge, one chord length upstream of the apex, and one chord length both above and below the wing in a horseshoe-shaped, C-type grid. It was assumed unnecessary to model the wind tunnel walls, rather model the wing in freestream conditions. For this and with ensuing discussion, a chord length is defined as 25 cm, whereas the root chord is 34.3 cm. The domain extended spanwise about 7 cm beyond the wingtip, where leading and trailing edges meet. All nodes were equally and relatively densely spaced, such that the volume consisted of about 300,000 tetrahedral cells and 60,000 nodes. The wing, which remained virtually unchanged throughout later grid modifications, had the domain's largest concentration of triangular faces, to better capture boundary layer effects and to have higher resolution on the surface where experimental pressure sensors were located. Angle of attack was simulated by setting Cartesian components for the freestream velocity. Thus a new mesh would not need to be generated for variations in angle of attack, rather the initial conditions would be appropriately modified.

The origin was located on the root chord, incident with the upper wing surface, and at $x/c = 0.55$, which is aligned with one of the rows of pressure sensors on the test article. Axes were oriented such that the positive x -axis followed the direction of air flow, positive y -axis traveled outboard of the origin, and positive z -axis pointed downward from or normal to the wing's lower surface. This convention was maintained throughout all later grid revisions.

Impetus for modifying the grid came from the following: comparing plots of the numerically predicted pressure coefficients (C_P) with those determined experimentally at the 30 locations described in Chapter II; viewing surface (two-dimensional, as well as isometric) contours of flow variables along the wall and within the domain to ensure the solution contours were captured and resolved within the domain extents; determining whether the solution was sufficiently converged or flow was fully developed (via error residuals for continuity, velocity, energy and viscosity equations, via mass flow conservation, and via constant (for steady cases) or steady cyclic (for unsteady cases) C_L and C_D); and comparing C_L with experimental and theoretical values. Such plots, contours and other post-processing graphics are compared and evaluated later in this chapter to give justification for grid revisions; thus detailed reasoning for grid modification is not presented in this section.

Another judge of numerical mesh suitability is to compute y^+ (or *y-plus*) values along the walls when using turbulence models. *Y-plus* indicates whether there is adequate grid resolution near the wall and is defined by

$$y^+ = \frac{\rho \cdot u_\tau \cdot y_P}{\mu} \quad (3.1)$$

where $u_\tau = (\tau_w/\rho_w)^{1/2}$ is friction velocity, τ_w is wall shear stress, ρ_w is fluid density at the wall, y_P is distance from point P to wall, ρ is fluid density at point P , and μ is fluid viscosity at point P . The Spalart-Allmaras (S-A), k- ϵ and Reynold Stress (RSM) turbulence models have a desirable wall y^+ range of $30 \leq y^+ \leq 60$, while the Large Eddy Simulation (LES) model requires $y^+ \approx 1$ along the walls (FLUENT, 2001: 10.8.1, 10.9.1-5, 27.4; Hoffman, Chiang, 2000.III: 55).

Revisions are denoted alphabetically, so Revision A, shown in Figure 3.1, extended the domain 20 chord lengths downstream and five chord lengths above and

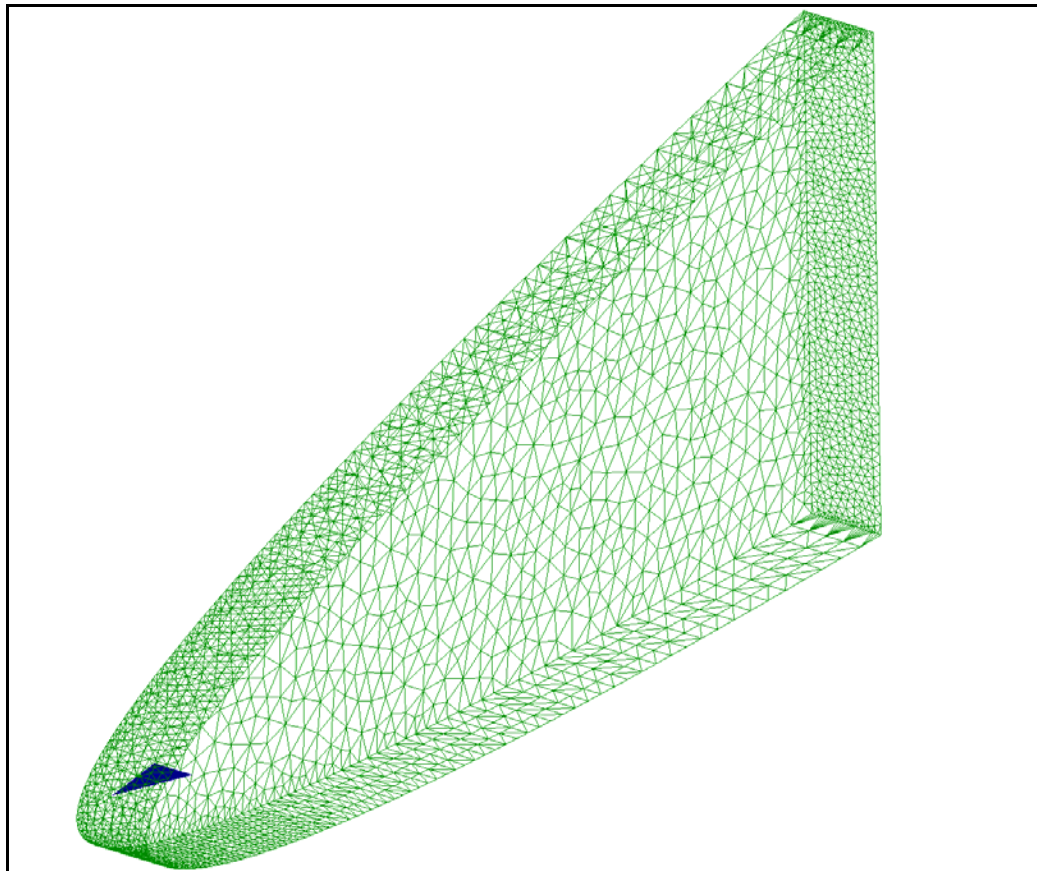


Figure 3.1 – Mesh Generation, Revision A: Farfield Model with One Tunnel Wall

below the wing, but the upper and lower trailing extents were connected via parabola vice the horseshoe shape of the initial mesh. Node distribution on the wing remained unchanged, though the wing was offset 1.27 cm from the wall to account for the mounting bracket and to move the wing farther from the wall boundary layer. The rest of the domain had considerably fewer cells and nodes, reducing to about 80,000 tetrahedral cells and 20,000 nodes. In this revision, nodes were clustered toward the leading end (or parabola base) to give better resolution.

Revision B, shown in Figure 3.2, extended downstream to 100 chord lengths past the wing trailing edge and up an additional 20 chord lengths beyond the wing upper surface – basically enlarging the computational domain to capture the generated vortex. About 58,000 nodes were added, mostly in the region around the wing as seen in Figure 3.3, to further enhance resolution, resulting in a total of about 400,000 cells.

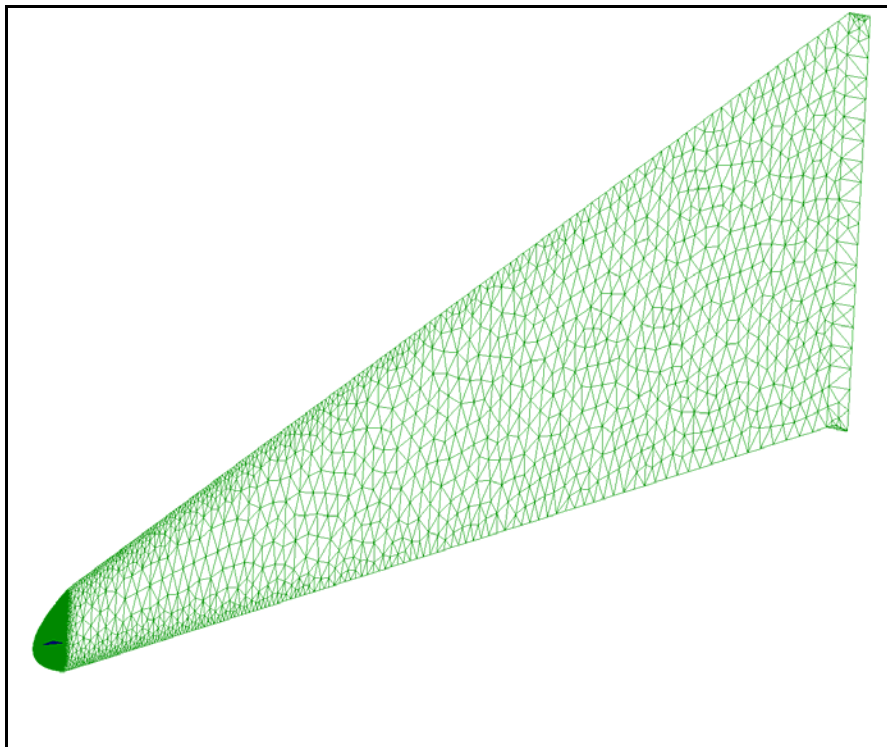


Figure 3.2 – Mesh Generation, Revision B: Upper and Downstream Extensions

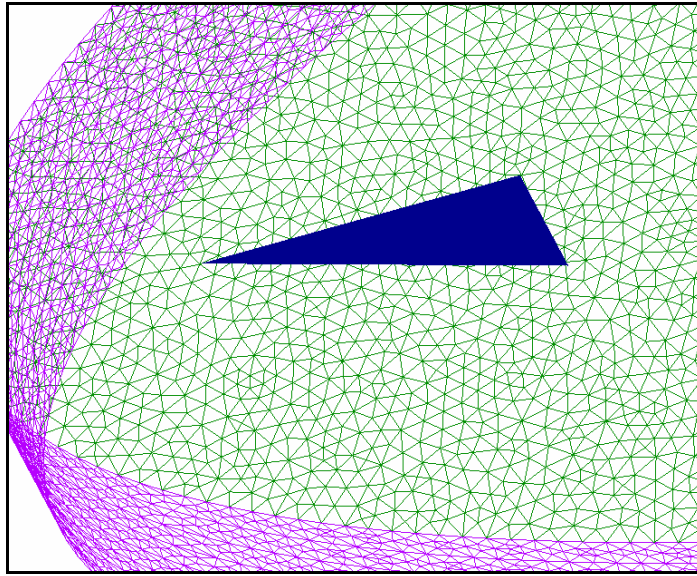


Figure 3.3 – Mesh Generation, Revision B: Closer View of Region around Wing

Revision C expanded the downstream extent to 150 chord lengths (37.5 m) and upper extent to 100 chord lengths (25 m), as seen in Figure 3.4. Number of nodes was

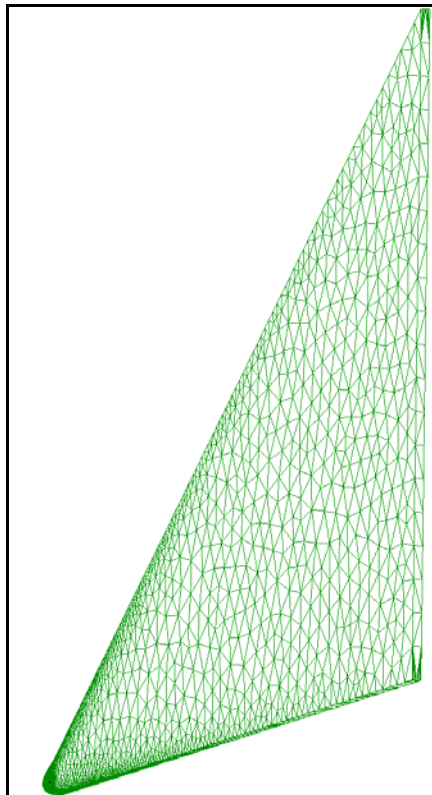


Figure 3.4 – Mesh Generation, Revision C: More Upper and Downstream Extensions

basically maintained in the region around the wing but greatly reduced in the farfield areas, bringing total cell count to 246,000, with 48,000 nodes. Note the relatively minuscule size of the wing in this domain.

Revision D, shown in Figure 3.5, simply extended the spanwise dimension of the domain to 60 chord lengths and nearly maintained the same number of nodes and cells. The parabolic front end was only continued for a few chord lengths in the spanwise direction before it flattened, which is characteristic of the automated grid generation; to obviate this problem, the user would need to generate a more closely ribbed structure (which was done in Revision F) or integrate a structured grid into this portion of the domain. This domain size effectively “captured” all solution contours, but computed data still did not adequately match experimental results.

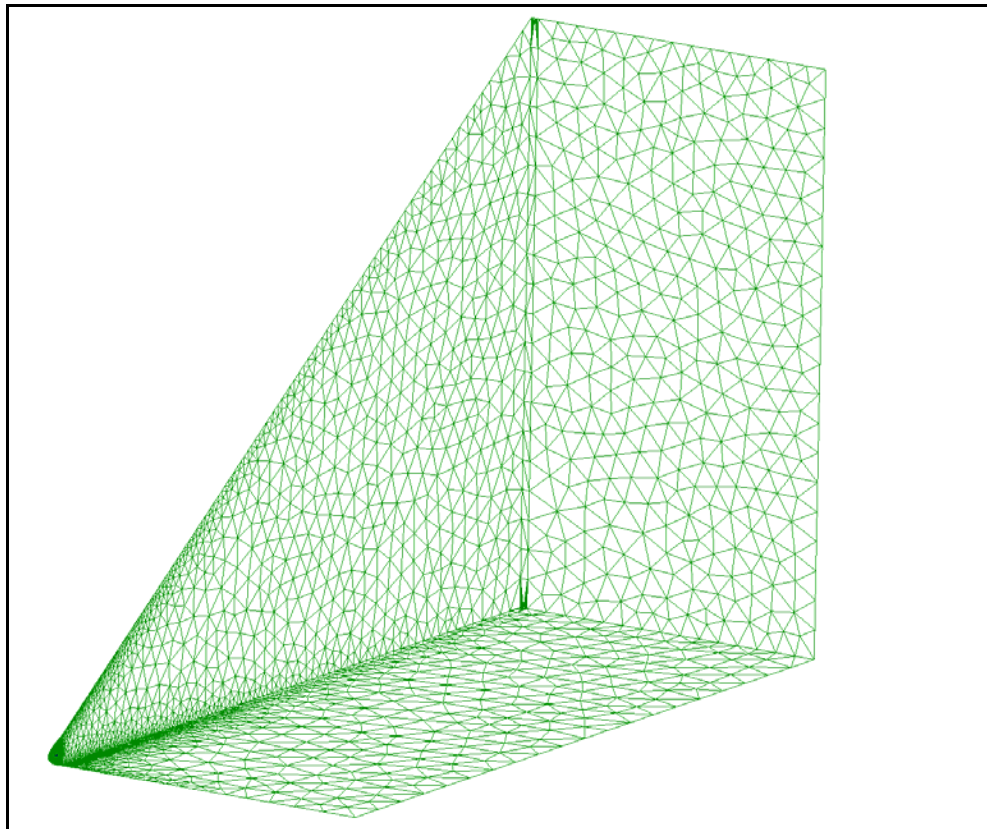


Figure 3.5 – Mesh Generation, Revision D: Spanwise Extension

Meshes to this point had not really accounted for flow disturbances which may propagate upstream of the wing, since flow was low subsonic in this case. Thus Revision E extended the domain 20 chord lengths upstream of the wing, added another 10 chord lengths to the extent below the wing, as shown in Figure 3.6, and dramatically increased the number of nodes in the wing region, as shown in Figure 3.7. Further, the wing was separated as an entity to allow for calculation of C_L and C_D . These changes brought the number of tetrahedral cells to 523,000 and number of nodes to 100,000.

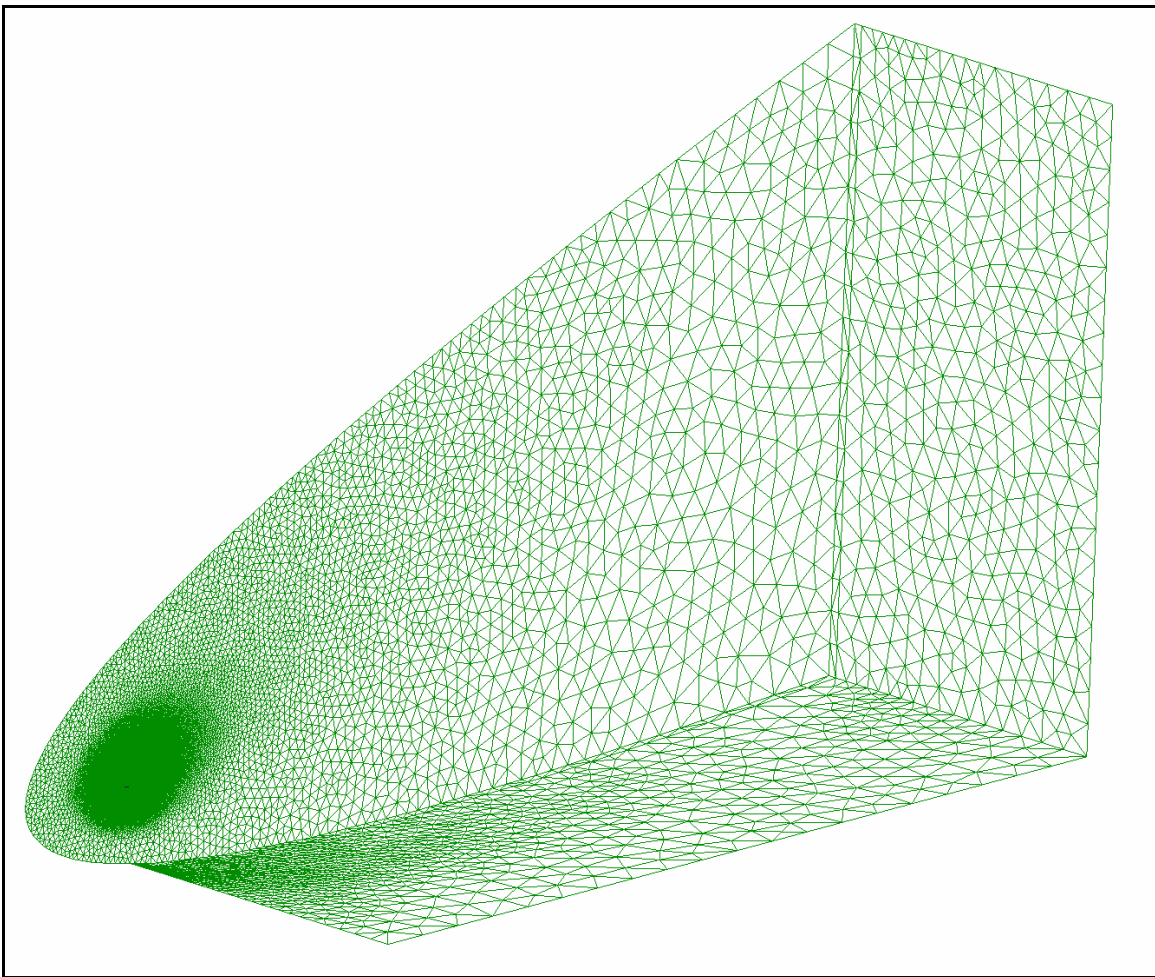


Figure 3.6 – Mesh Generation, Revision E: Upstream and Lower Extensions

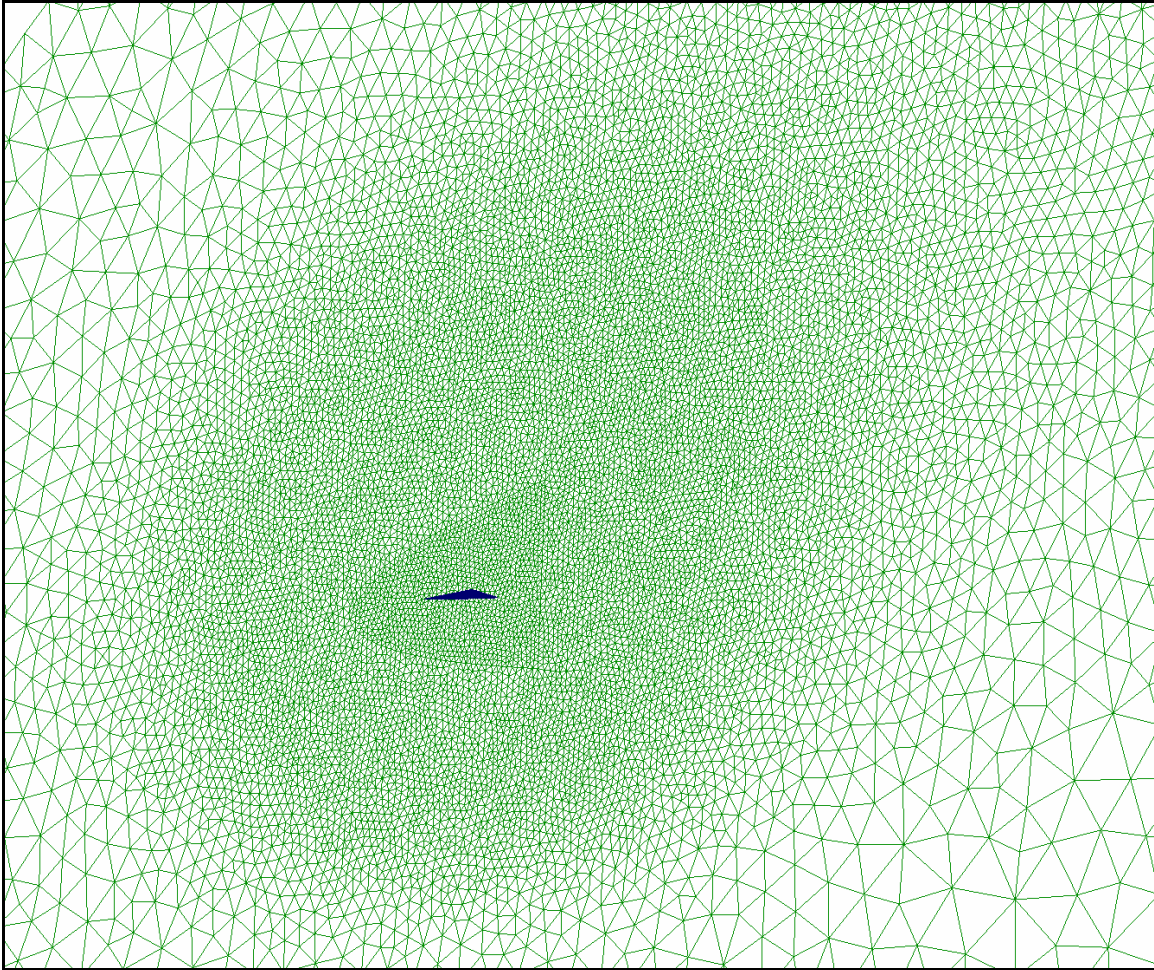


Figure 3.7 – Mesh Generation, Revision E: Closer View of Region around Wing

Since Revision E gave an unacceptable solution, Revision F extended the domain downstream to 250 chord lengths but reduced the number of tetrahedral cells to 448,000, with 88,000 nodes. This revision also eliminated possible inaccuracy from the flattened front side by making it parabolic to the spanwise extent, as seen in Figure 3.8. These changes had little effect on the solution, since the domain was already sufficiently large and because flow far outboard of the wing had no recirculation issues.

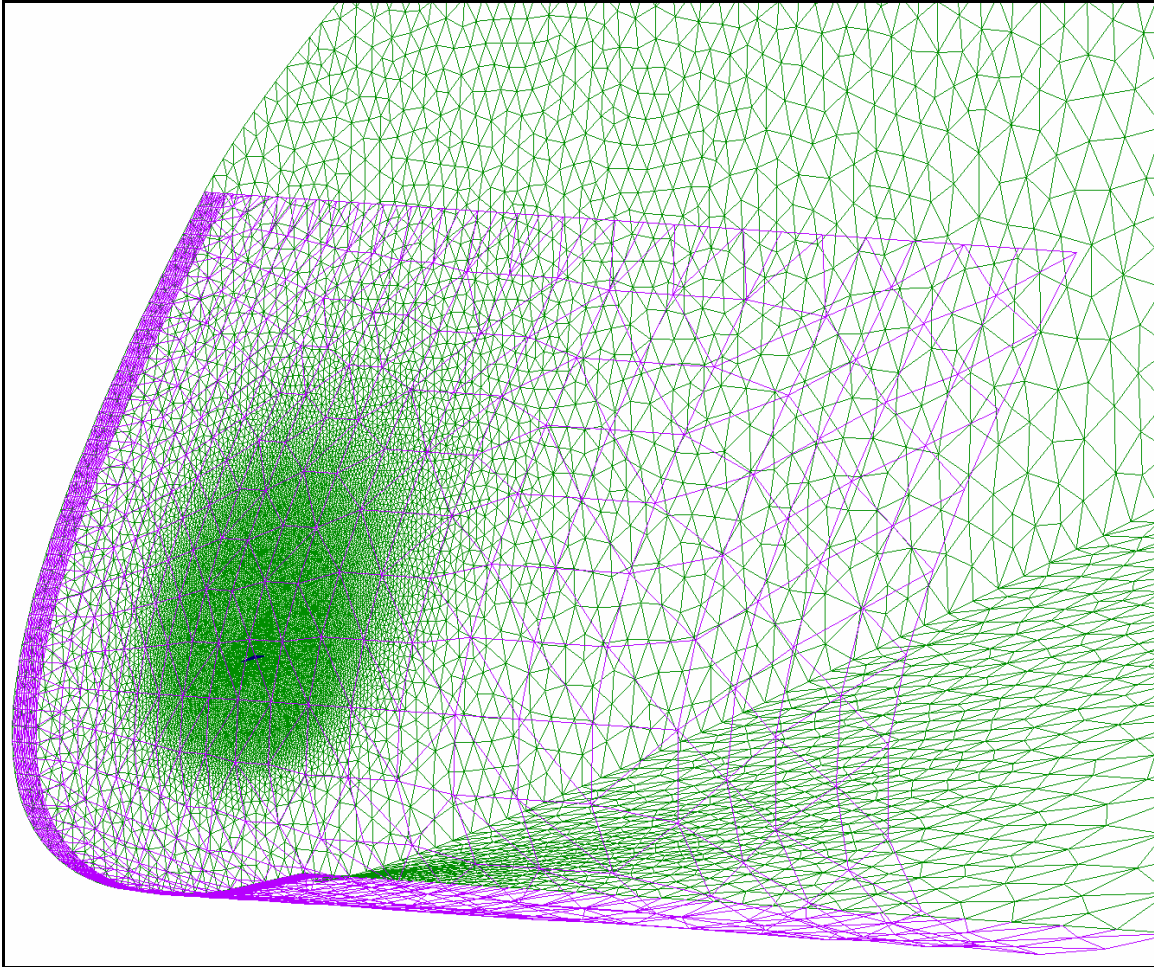


Figure 3.8 – Mesh Generation, Revision F: Parabolic Upstream Extent

At this point, it was determined the most prudent course of action would be to return to the drawing board and create the domain differently. That is, modeling the computational domain to be the same as the experiment's physical domain – a wind tunnel – was the basis for Revision G.

Revision G eliminated all existing boundaries around the wing and created a four-sided wind tunnel test section 60.96 cm in height, 60.96 cm in width, and which extended 20 chord lengths both upstream and downstream of the wing. Still offset 1.27 cm from the tunnel wall, the wing was rotated 15° about the y -axis to simulate angle of attack, since air would need to flow straight through the tunnel or perpendicular to the inlet and

outlet boundaries. A problem with rotating the wing to the proper angle of attack is that any modification of that angle requires a new grid to be generated, as opposed to simply altering a boundary condition in the flow solver. This setup called for a hybrid mesh, consisting of two structured blocks and one unstructured block. The unstructured block centered around the wing, extending two chord lengths upstream and downstream of the origin and filling that section of tunnel, as shown in Figure 3.9. Structured blocks extended outward from each end of the unstructured volume, and nodes were distributed more densely within a region 5 cm from each wall surface to better capture boundary layer effects. The new domain consisted of about 100,000 hexahedral cells (structured

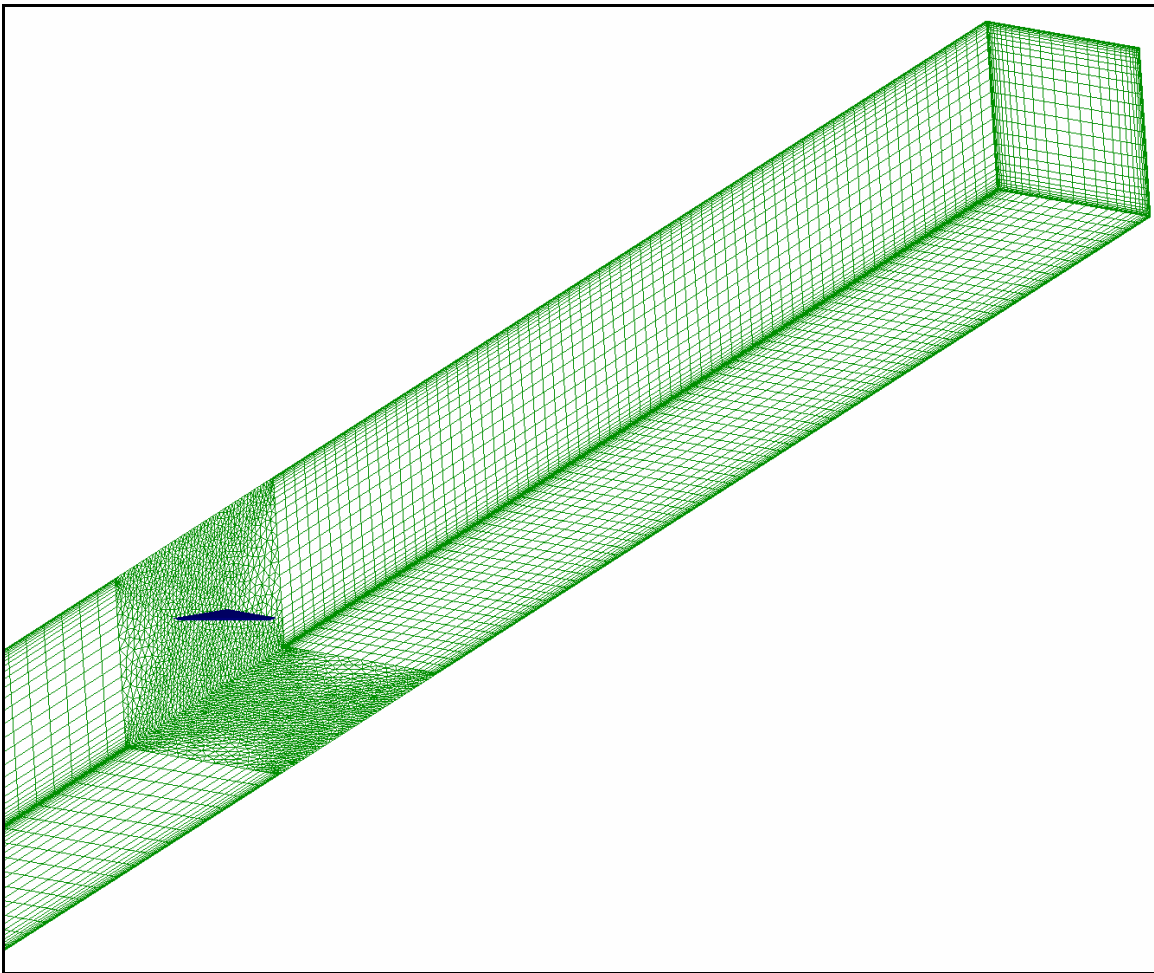


Figure 3.9 – Mesh Generation, Revision G: Hybrid Grid Including Wind Tunnel Model

volume) and 300,000 tetrahedral and pyramid cells within and along the borders of the unstructured volume.

Revision H enhanced wall boundary layer resolution within the unstructured block by isolating the unstructured from structured blocks via “transition” blocks and by creating an interior volume around the wing. Referring to Figure 3.10, note the structured walls have fewer nodes than were needed to adequately resolve boundary layer effects in the unstructured wing section of the tunnel. Therefore, a transition zone (about 5 cm long) was put in place, where the node count was, for example, 31 on one side and

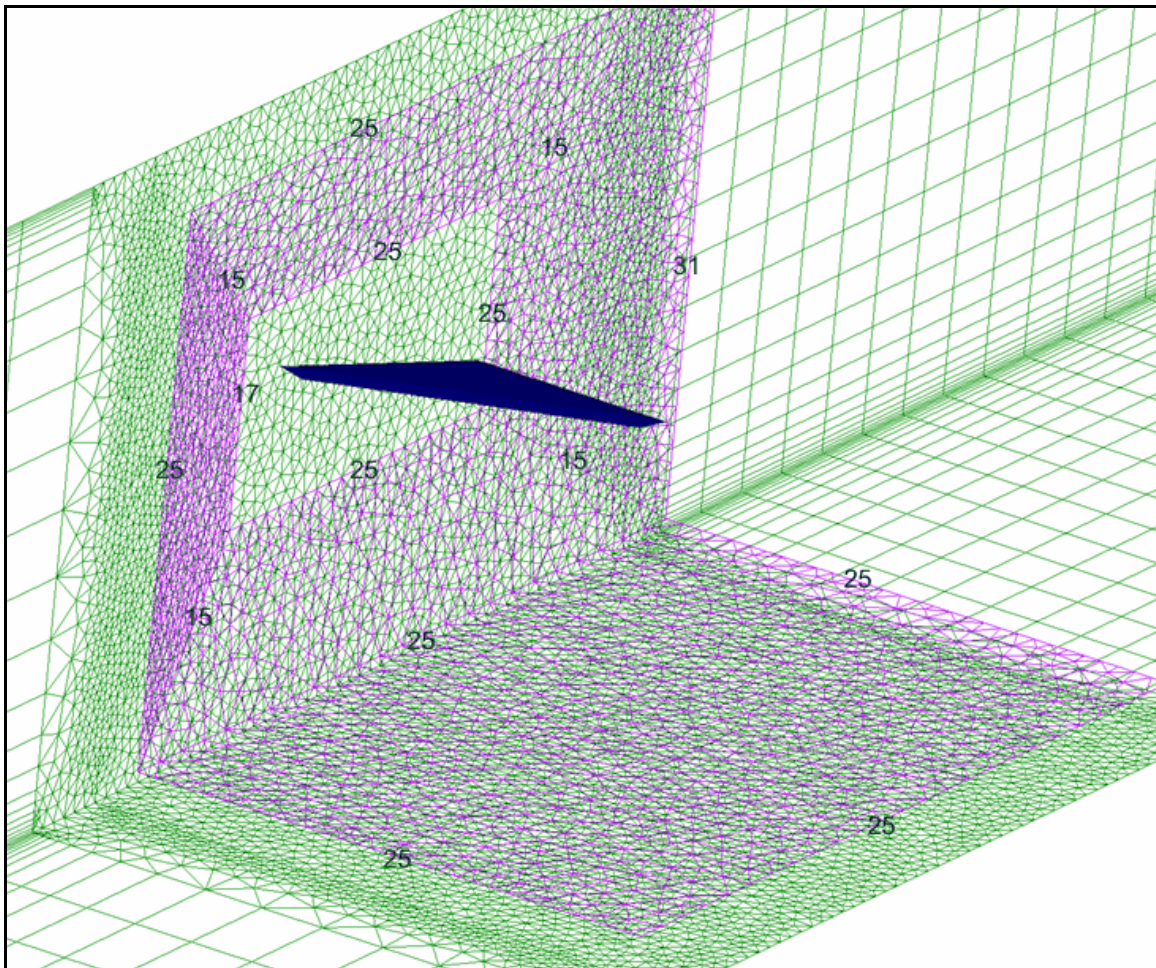


Figure 3.10 – Mesh Generation, Revision H: Enhanced Boundary Layer Resolution (Features Some Nodal Dimensions for Revision L)

71 on the other; the transition zone had adequate resolution but was short in length while the unstructured volume then had good resolution. Next, an interior volume was created 5 cm inside all unstructured tunnel walls, shown as purple mesh in Figure 3.10, except on the wing-mounted wall where resolution was already adequate. This resulted in a boundary layer 3-7 cells thick throughout the model's unstructured portion. Total cell count increased to 590,000.

In an effort to reduce boundary layer turbulence which engulfed the wing in Revision H, Revision I truncated the leading structured tunnel to one chord length, such that the pressure inlet was then about 60 cm from the wing apex, as seen in Figure 3.11.

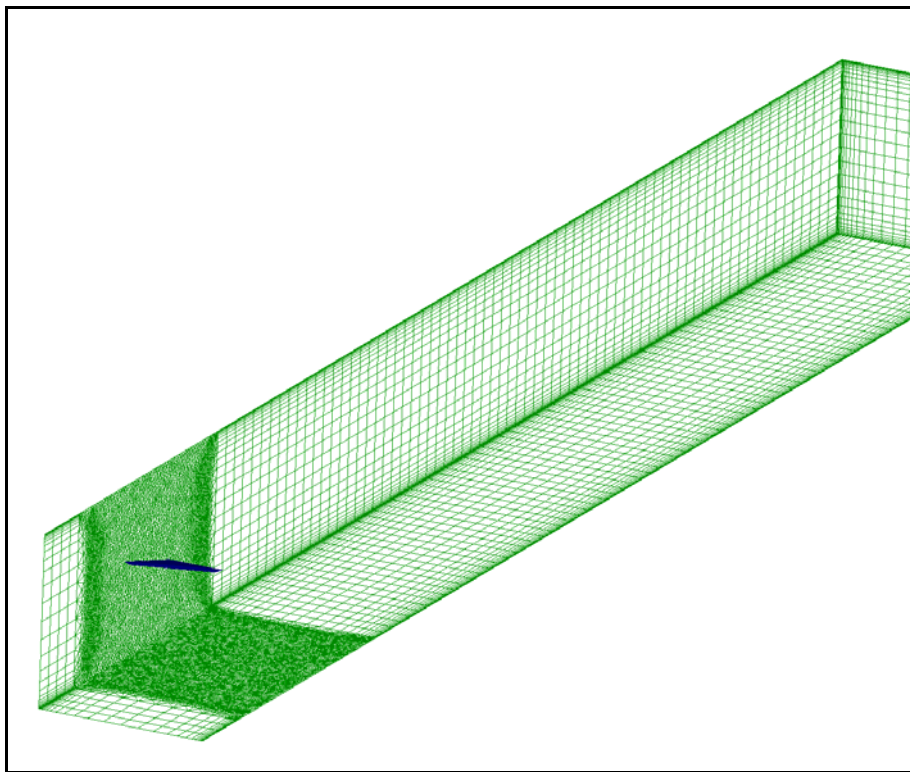


Figure 3.11 – Mesh Generation, Revision I: Truncated Distance to Inlet

At this point, discussion with the UC test engineer revealed the presence of a boundary layer refresher plate during wind tunnel testing (May, 2002.c), which generated

essentially laminar flow near the wing apex, as discussed in Chapter II. For Revision J the refresher plate's effect was approximated by truncating the domain to 7.6 cm upstream – later corrected by UC test engineer to be 5 cm (May, 2002.b) – of the wing apex and providing evenly distributed, non-turbulent flow at the inlet, as seen in Figure 3.12. This revision also added more nodes to the unstructured volume, bringing total number of cells to nearly 800,000. The wing was still offset from the wall, an error corrected in the next revision.

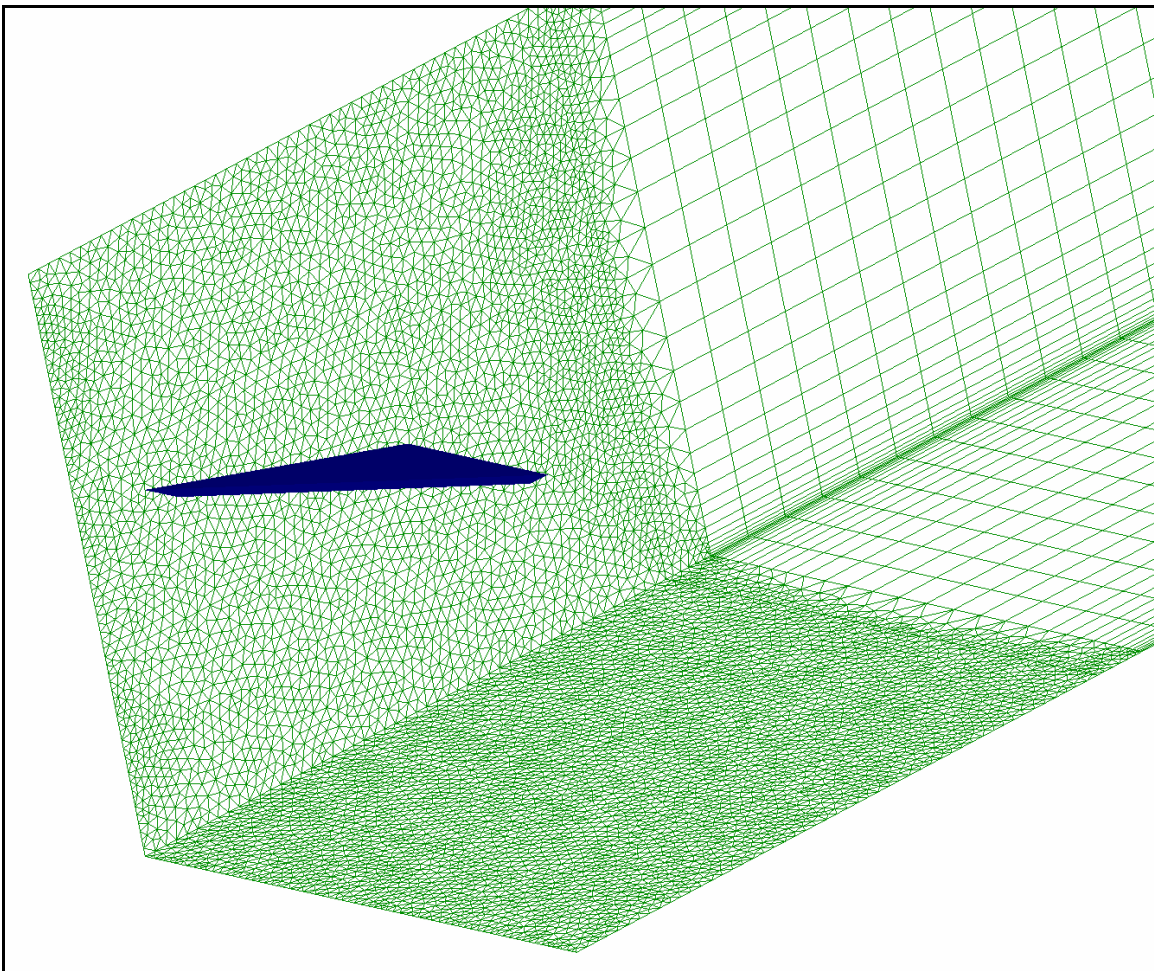


Figure 3.12 – Mesh Generation, Revision J: More Truncated Distance to Inlet

Revision K placed the wing flush against the tunnel wall/refresher plate, modified the inlet to be 5 cm upstream of the wing apex, and included several derivative meshes at

various angles of attack. Figure 3.13 shows this numerical mesh with wing at 15° angle of attack. With wing against wall, the number of domain cells reduced to 764,000.

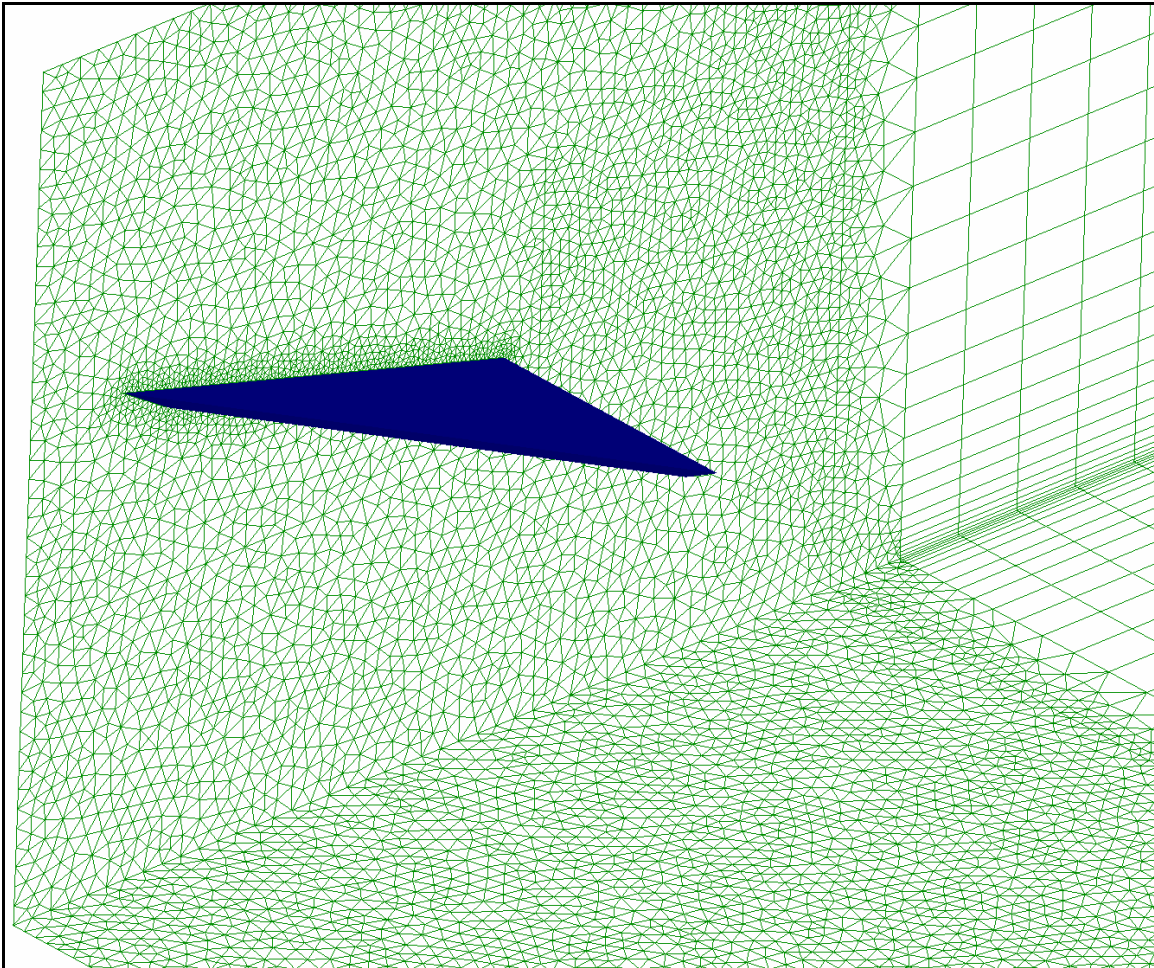


Figure 3.13 – Mesh Generation, Revision K: Wing Flush Against Wall

From Revision K findings, it was determined that the angle of attack should be 18° for best results; more detail is provided later in this chapter. Revision L incorporated this modified wing angle and increased fidelity of the boundary layer refresher plate approximation by including the plate's leading edge 45° bevel, coupled with the re-addition of structured upstream tunnel, as seen in Figure 3.14. About 4.3 cm upstream of the wing apex, the tunnel wall angles 45° inboard for 0.635 cm in the x -direction, then transitions for a centimeter or so into a structured mesh, which then continues to a

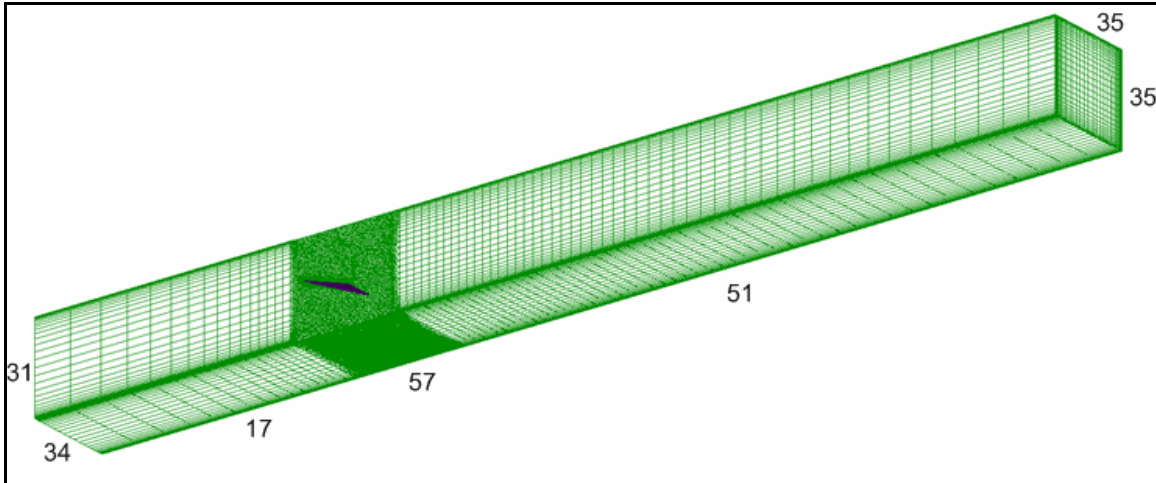


Figure 3.14 – Mesh Generation, Revision L: Tunnel with Nodal Dimensions

distance 200 cm upstream of the origin. The tunnel runs 500 cm downstream of the origin, which is 200 cm greater than the actual wind tunnel test section’s downstream segment, but this was done to allow greater extent for flow resolution and accuracy.

The numerical boundary layer refresher plate is an approximation for three reasons: first, this ramp extends to the tunnel ceiling and floor vice covering only half the vertical distance of the tunnel wall, as shown in Figure 2.5; second, this simulated plate is not offset by 1.27 cm from the tunnel wall; and third, the approximated plate runs the remaining downstream distance of the tunnel, instead of extending only 45.72 cm from the plate’s leading edge. The first and third approximations likely produce negligible differences in the solution, but approximating the plate as flush against the tunnel wall is not the same as the actual wind tunnel setup in the vicinity of the wing. Here a tradeoff was made for greater modeling simplicity, as the solver would possibly have needed to deal with additional flow physics between the refresher plate and tunnel wall and with more complicated downstream flow. Revision O removed the second and third approximations.

Figure 3.14 shows nodal dimensions for the tunnel walls and inlet and outlet faces, and Figure 3.15 shows them for the transition zone between structured and unstructured segments, for the unstructured volume walls and for the wing. To avoid a

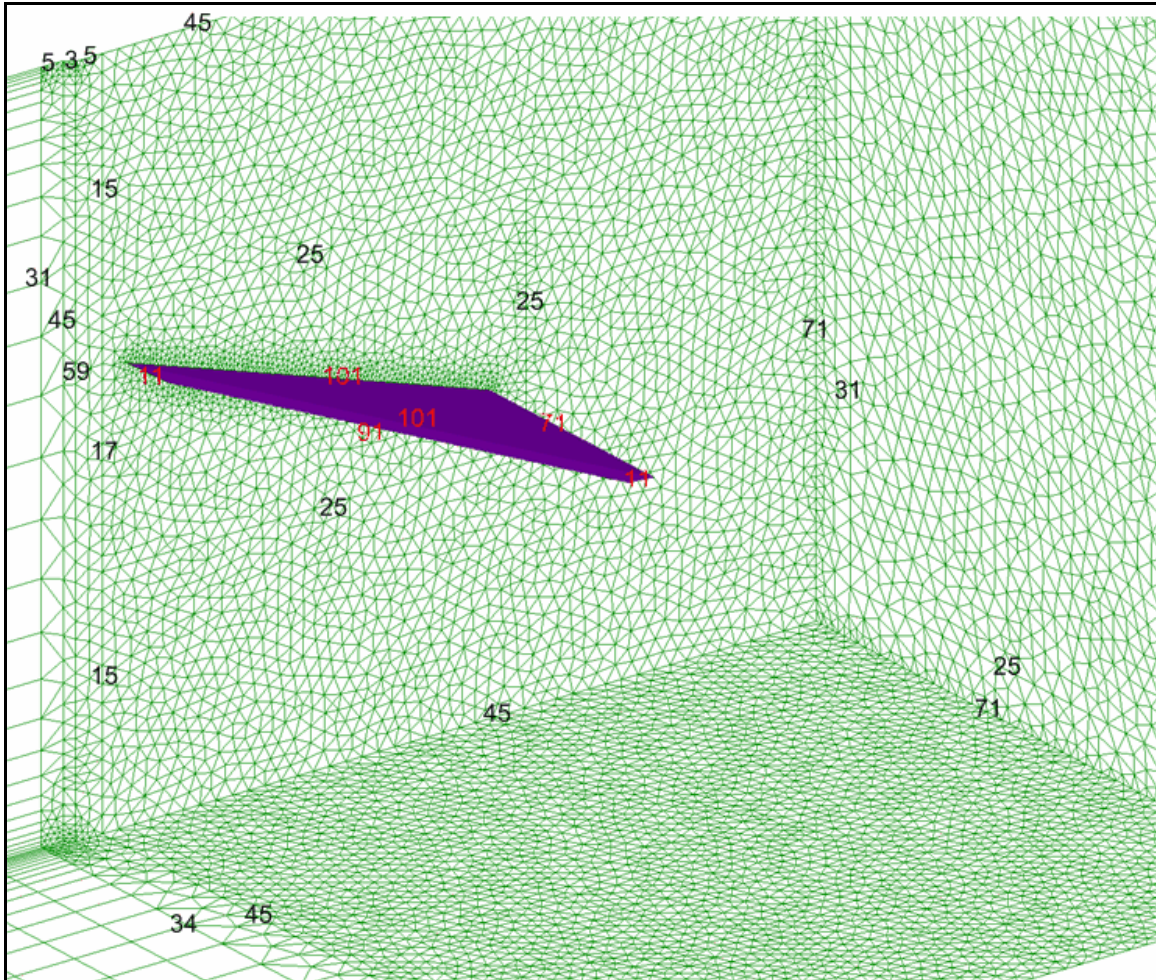


Figure 3.15 – Mesh Generation, Revision L: Nodal Dimensions for Tunnel Wing Section

superfluous figure, nodal dimensions for Revision L's interior volume surrounding the wing are shown in Figure 3.10, since this grid structure remained the same; faces not shown have essentially the same nodal dimensions as the bottom face. This interior volume allowed for a 5-cm wall boundary layer thickness (where cells were more concentrated) throughout the unstructured zone of the tunnel. Furthermore, in the

structured portions of the tunnel, the model provided a 5-cm zone along the tunnel walls for boundary layer resolution. Length of that zone was divided into 7 square cells, where the one closest to the wall measured 0.2 cm on each side, then they increased to 1.3 cm for the seventh cell.

Not including interior faces, the numerical model consists of 67,598 triangular (unstructured) and quadrilateral (structured) faces; this number does include faces of the interior volume from Figure 3.10. The wing claims 24.2% of that number of faces. There are a total of 585,297 cells and 176,626 nodes; the cells include 452,686 tetrahedrons (unstructured), 58,971 mixed pyramids, prisms and tetrahedrons (transition), and 73,640 hexahedrons (structured). Note that while the unstructured portion is 11.4% of the tunnel length, it accounts for 87.4% of the total cells.

Figure 3.16 shows a side view of the wing, detailing the cell face distribution where the wing interfaces with the tunnel wall. Figure 3.17 displays tightly packed cell faces on the upper wing surface; excluding the three blowing ports and the region immediately surrounding them, the sides of each triangular face measure about 3.4 mm.

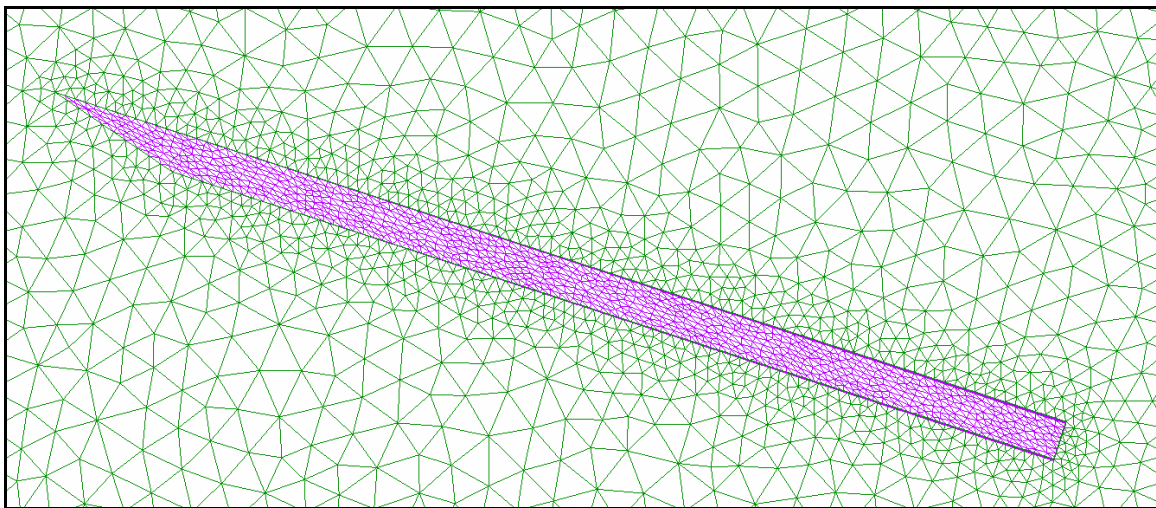


Figure 3.16 – Mesh Generation, Revision L: Profile View of Wing Mounted to Wall

Figure 3.18 is a close-up view of one of the blowing ports (enclosed by a blue circle) on the wing upper surface, where 104 triangular faces fit into the 0.49-mm² area.

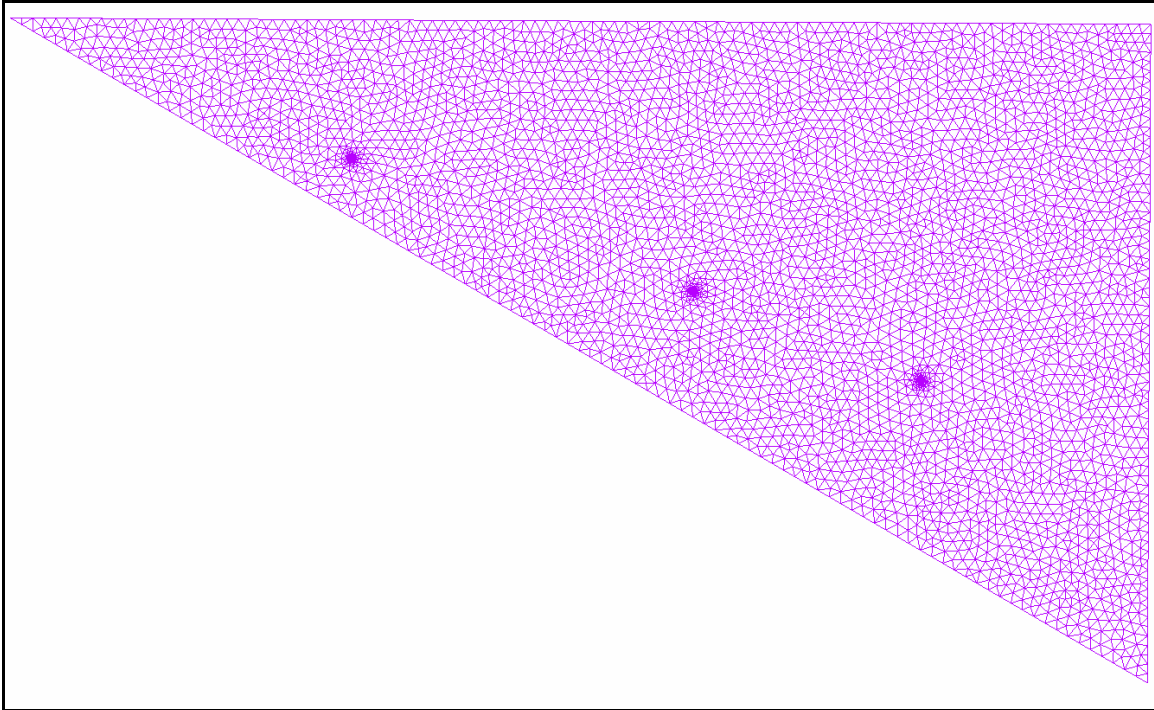


Figure 3.17 – Mesh Generation, Revision L: Upper Surface of Wing

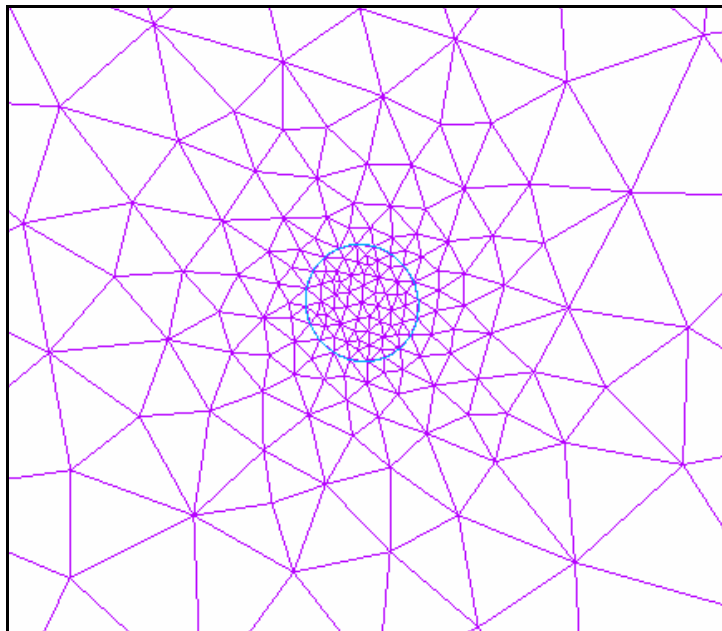


Figure 3.18 – Mesh Generation, Revision L: Close-Up View of Wing Blowing Port

Boundary layer resolution, in both structured and unstructured blocks of Revision L, proved adequate for some turbulence models but not all. Over the wing surface, Figure 3.19 shows that wall y^+ values ranged between 15 and 60, which is acceptable resolution for S-A, $k-\epsilon$, and RSM turbulence models, but it is inadequate for the LES model; cells around the blowing ports also have finer resolution as shown in the figure by

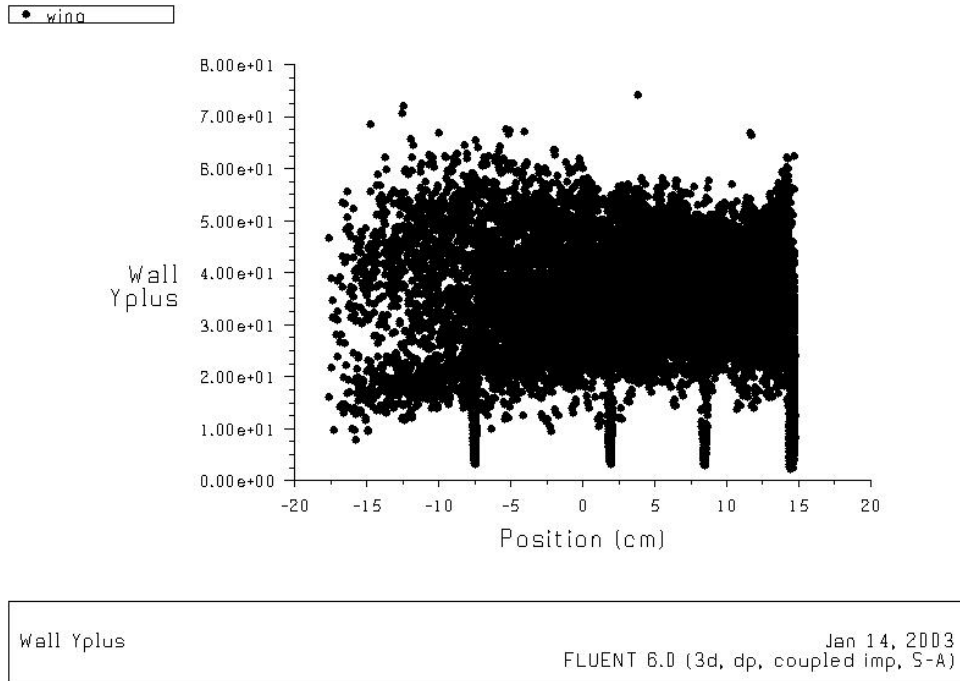


Figure 3.19 – Wall y^+ Values along Wing Surface in x -Direction, Revision L, Steady S-A points extending as low as $y^+ = 3$. Figure 3.20 shows wall y^+ values for the tunnel walls. Structured portions of the domain wall boundary layer have better cell resolution, where y^+ ranges between 10 and 40, and unstructured walls have poorer resolution, particularly in the transition zones between structured and unstructured regions where y^+ reaches as high as 220 but ranges mostly between 40 and 175. This indicates that the unstructured tunnel wall resolution is acceptable though not optimal; finer resolution would require a tradeoff for increased computing time and/or resources. Tunnel wall resolution was generally not refined in this study because emphasis was placed on solution prediction in

regions of vortex generation and breakdown, which are away from the tunnel walls; however Revision O includes some boundary layer refinement along walls and wing.

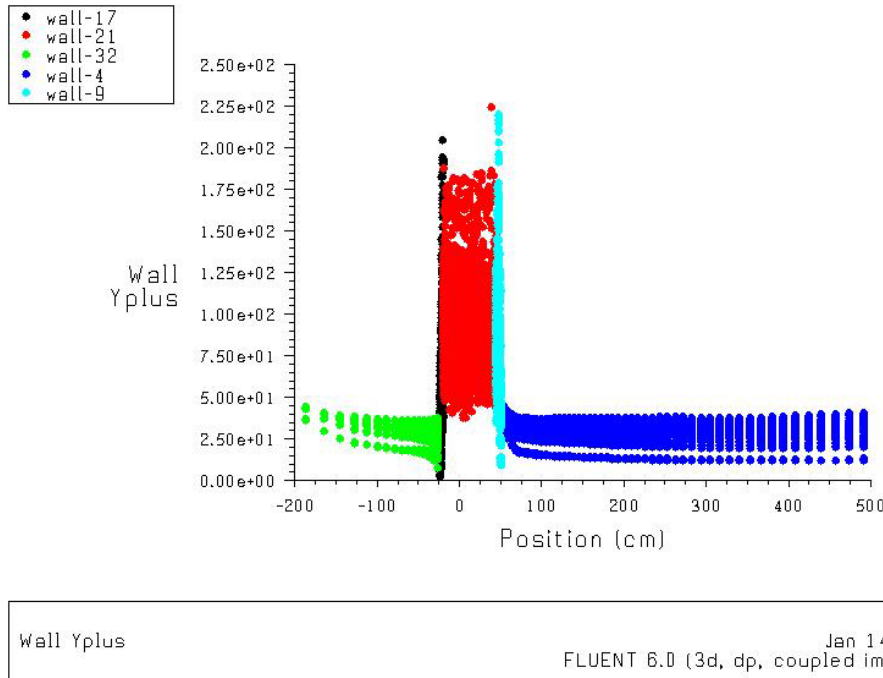


Figure 3.20 – Wall y^+ Values along Tunnel Walls in x -Direction, Revision L, Steady S-A

As for additional mesh revisions, Revision M is specific to the blowing cases (Chapter IV) and Revision N will be addressed in the mesh adaptation section later in this chapter. Revision O addressed the boundary layer refresher plate approximations discussed above. Shown in Figure 3.21, this mesh revision altered Revision L by creating the 1.27-cm gap between refresher plate and tunnel wall and did not include the mounting bracket, seen in Figure 2.3; the plate extends to the top and bottom tunnel walls and extends downstream 45.72 cm from its leading edge, as in the experimental setup. The wing remained at $\alpha = 18^\circ$, but nodes were added to its upper surface which resulted in an additional 3,306 faces and 58,730 tetrahedral cells. Nodes were also added to the upstream structured block to refine the cell transition to the unstructured volume of the

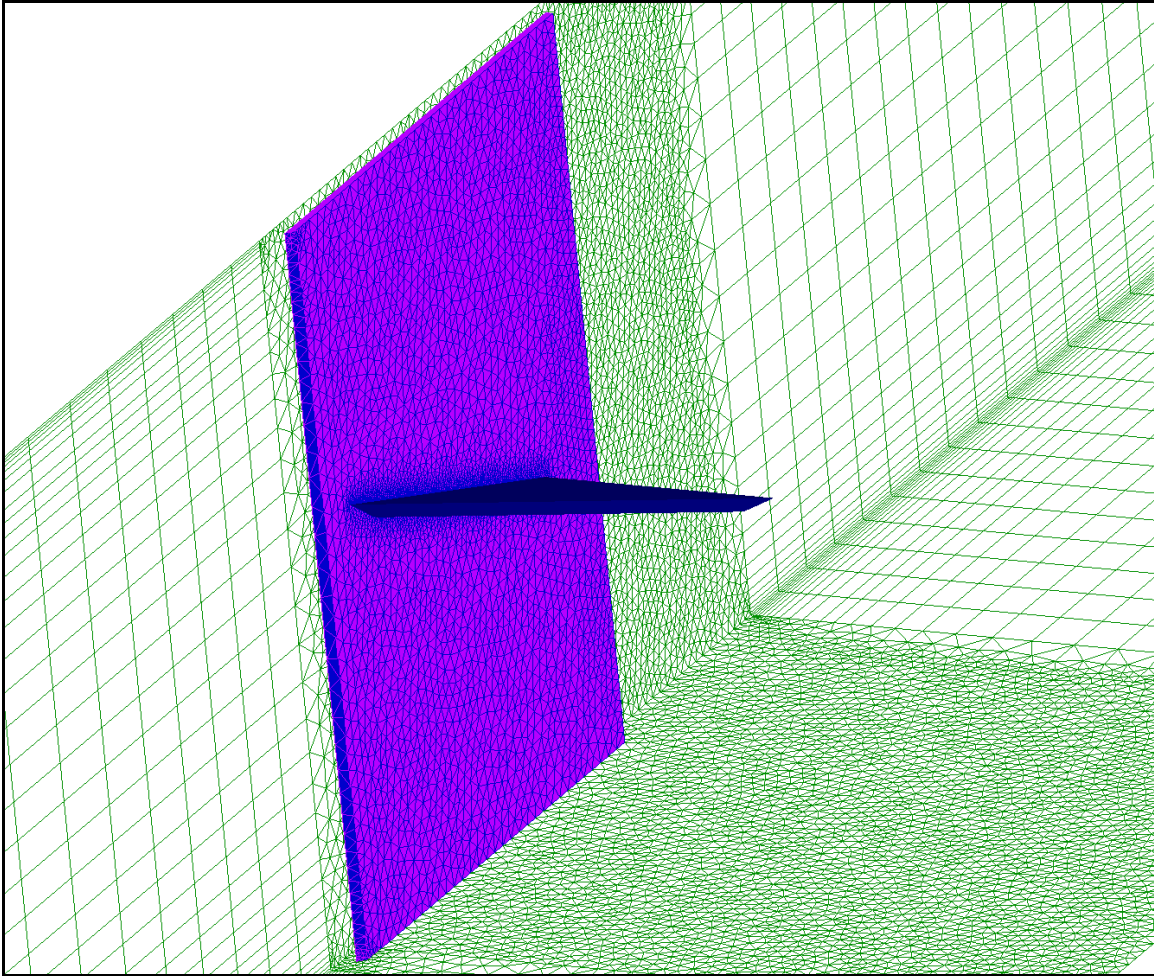


Figure 3.21 – Mesh Generation, Revision O: Boundary Layer Plate Separated from Tunnel Wall, Plus Wing and Transition Refinements

tunnel's wing region and to improve y^+ values in that transition zone; this resulted in an additional 14,188 hexahedral and 14,731 mixed cells. Mesh Revision O had a total of 207,784 nodes and 672,946 volumetric cells.

These modifications did improve wall y^+ values in several areas within the numerical domain. Lower bounds were not enhanced, but y^+ upper bounds reduced on the wing from Revision L's 60 down to 45; along the tunnel walls, y^+ reduced its majority upper bound (below which are most of the data) from 175 down to 100 and maximum upper value from 220 down to 130. While these were marked improvements

in cell resolution along the walls, the numerical mesh still would not be fine enough for the LES turbulence model. Further results from this grid revision are included later in this chapter, but it did not prove superior to mesh Revision L because approximating the plate as flush against the tunnel wall was a good assumption.

Solver Parameters and Turbulence Models

This section discusses the procedure used in FLUENT to initialize the various flow cases, including selection of and justification for solver parameters, flow and turbulence models, discretization schemes, and so forth.

Import Numerical Mesh

After opening FLUENT in three-dimensional, double-precision mode, the user imports or reads a case file, which in this instance was created with and exported by Gridgen (using *Export Analysis Data* command). A Gridgen case file contains information about the mesh and boundary conditions, which may be compatible with FLUENT. The grid was then checked for negative volumes, face handedness (where left-handedness on a face indicates negative volume), and properly matched numbers of nodes to cells (FLUENT, 2001: 5.5.1). Next the domain was reordered and cell faces were smoothed and swapped. Reordering the domain – nodes, faces and cells – places neighboring cells nearer each other in memory “to reduce the cost of memory access” (FLUENT, 2001: 5.7.10), and smoothing/swapping, which applies only for unstructured portions of a grid, repositions nodes and combines faces where possible to reduce total cell count and generally improve mesh quality (FLUENT, 2001: 23.11-23.11.2). These actions do not affect the model geometry proper. Lastly, the case file in FLUENT was

scaled from its default meter setting to the centimeter scale used in generating the grid. All other units remained in default SI units.

Solver Initialization

Following are the options selected in FLUENT to generate an initial solution. In the *define*→*models* menu, *solver* selections included coupled solver, implicit formulation, three-dimensional space, and steady time. The coupled, implicit formulation was chosen for computational efficiency, quicker convergence and because sufficient computing resources were available. Even though the vortex breakdown problem is inherently unsteady, a steady solver was chosen initially, hoping that it would lead to a good starting place (mesh geometry determination and turbulence model selection) before running unsteady cases. For later cases with unsteady time, the second-order implicit formulation was selected; second-order refers to the temporal order of accuracy, and implicit refers to time-stepping where the solution iterates to convergence at each time step. The user may opt to declare a maximum number of iterations per time step vice letting it run to meet a set of convergence criteria; for unsteady cases in this effort, that number was set at 20, and the initial time step was set at 0.0001 sec. This time step was set to not exclude effects of the vortex inner core's observed frequency of 1,000 Hz immediately prior to breakdown (Novak, Sarpkaya, 1999: 825); it was later discovered that this time step could be increased to 0.0004 sec without adverse effects on the solution. This step size, $\Delta t = 0.0004$ sec, allowed essentially for 2.5 computations per revolution of the vortex core upstream of breakdown. The solution then proceeded through an undetermined number of time steps, but at least a few flow cycles, until the solution either converged or reached a relatively steady time-periodic cycle. One flow cycle is defined as the time

required for an average particle trace to flow the distance of the domain, or domain length divided by freestream velocity; for $V_\infty = 16.05$ m/s, one flow cycle is 0.436 sec.

In the *define*→*models* menu, *energy equation* was enabled and *viscous* options include inviscid, laminar, Spalart-Allmaras (S-A), k- ϵ , k- ω (not investigated in this study – refer to Chapter I), Reynolds Stress (RSM), and Large-Eddy Simulation (LES). Figure 3.22 shows the FLUENT *define*→*models*→*viscous* drop-down menu. Initially, the S-A viscous model was chosen because it is the simplest of the turbulence models available in FLUENT and because previous studies have shown that turbulence modeling gives more accuracy in prediction of vortex strength, bursting location and extent of breakdown

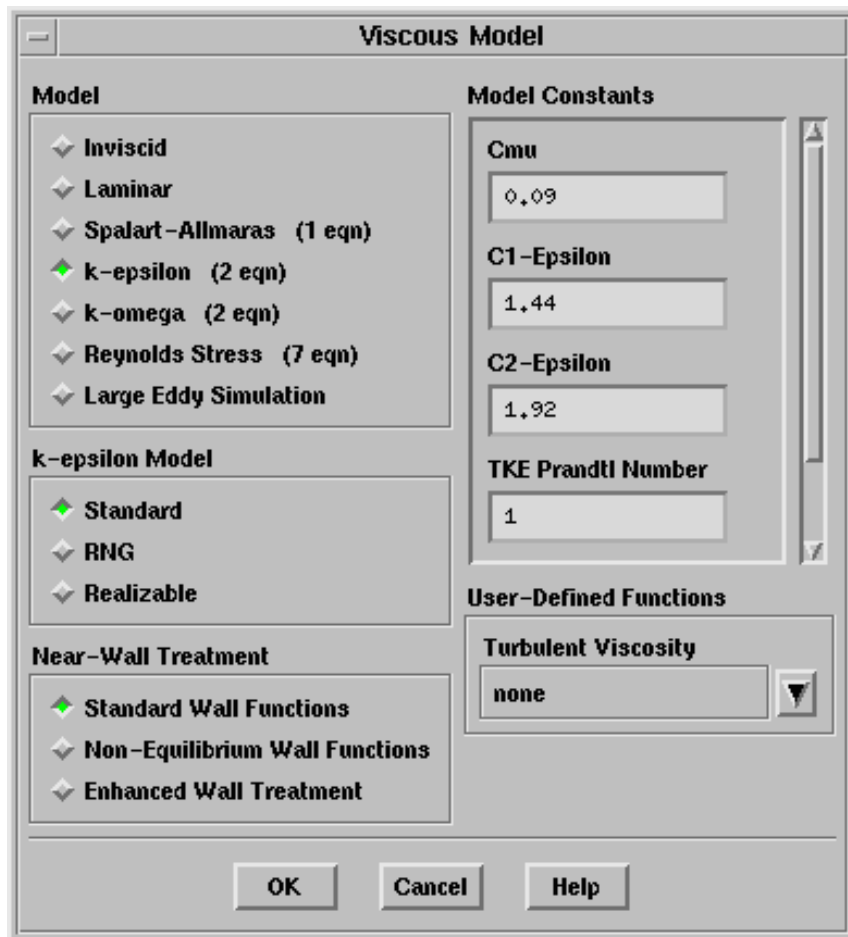


Figure 3.22 – FLUENT *Define*→*Models*→*Viscous* Menu (FLUENT, 2001: Tutorial 9.3)

region, and it is the only way to model swirling flow with anisotropic turbulence (Ekaterinaris, Schiff, 1990: 61; Novak, Sarpkaya, 1999: 833). FLUENT default values were used for S-A model coefficients, and no attempts were made to alter them. Inviscid, laminar, RNG k- ϵ and RSM models, with FLUENT default settings, were all compared in steady state with the S-A model. The following models were run in unsteady time: LES, with Smagorinsky-Lilly subgrid scale model, RNG k- ϵ , RSM, and S-A (FLUENT, 2001: 10.4.2, 10.7.2). With exceptions noted above, these models all used FLUENT default settings for coefficients and wall treatment.

In the *define*→*materials* menu, the only operating fluid, air, was defined with ideal-gas density, to allow for compressibility effects, and with the Sutherland Law viscosity using Three-Coefficient Method, which is recommended for cases with compressible flow; otherwise, FLUENT default values were used for air properties. Although it is accurate, Sutherland viscosity was likely overkill, since it is a function of the ratio of total and static temperature, which in this case is near unity (FLUENT, 2001: 7.3.2). Arguably the baseline model might do better with incompressible air, but the flow control cases inject air at or near sonic velocity, so the more robust model accounts for compressibility effects. Under *define*→*operating conditions*, the operating pressure was set to zero and referenced at the origin, allowing for absolute pressure computations.

Regarding *define*→*boundary conditions*, the wing, unused blowing ports on the upper wing surface, boundary layer refresher plate, and all tunnel walls were defined as no-slip, aluminum, impermeable, insulated wall boundaries (i.e., no heat or mass flux). In the farfield mesh models, through Revision G, remaining domain boundaries were set as farfield pressure, where gauge pressure was 99.56 kPa (atmospheric pressure measured

in the lab during wind tunnel testing), M_∞ was 0.0437 (based on the original claim that $V_\infty = 15$ m/s), temperature was 298 K (ambient temperature measured during tunnel testing), turbulent viscosity ratio (TVR) was 10 – FLUENT’s recommendation for external compressible flow (Tutorial 3), and components of the flow direction were $x = 0.965926$ or $\cos 15^\circ$, $y = 0$, and $z = -0.258819$ or $-\sin 15^\circ$, simulating the wing’s angle of incidence. TVR is the ratio of turbulent to laminar viscosity, where a value of unity corresponds to laminar flow. In later revision cases, it was discovered that varying TVR between 5 and 10 had no significant effect on the solution and that $\text{TVR} = 1$ (in farfield) didn’t allow for sufficient vortex strength (FLUENT, 2001: 27.4). For wind tunnel cases, entry to the tunnel was defined as a pressure inlet, where initial gauge pressure was 99.56 kPa, total temperature was approximated at 298 K, TVR was unity to give laminar flow at the inlet, flow direction was normal to the boundary, and gauge total pressure was set to a value that would create the appropriate freestream velocity; values used are shown as P_{TOT} in Table 3.1. Tunnel exit was defined as a pressure outlet, where outlet gauge pressure was 99.56 kPa, TVR was 10 for fully turbulent flow, and backflow total temperature was 298 K.

Table 3.1 – Pressure Inlet and Reference Values for Various Freestream Velocities

V_∞ (m/s)	P_{TOT} (Pa)	P_{INIT} (Pa)	ρ_∞ (kg/m ³)	P_{DYN} (Pa)
15.05	99,692	99,560	1.164377	131.867
15.4*	99,698	99,560*	1.20767*	143.206*
16.05	99,710	99,560	1.164437	149.981
17.03	99,729	99,560	1.164500	168.865
19.99	99,793	99,560	1.164713	232.710
24.98	99,924	99,560	1.165149	363.527

* Conditions reported during UC wind tunnel testing

The above boundary conditions remained the same whenever possible for k- ϵ , RSM and LES turbulence models; for inviscid and laminar cases, there was no TVR and Sutherland viscosity was not used as a property of air. For k- ϵ , RSM and LES models, turbulence intensity (ratio of root-mean-square turbulent fluctuations magnitude to freestream velocity) was used either instead of or in addition to TVR, where intensity was 0.05% at the pressure inlet and 10% at the pressure outlet – FLUENT’s recommendations for a laminar inlet and fully turbulent outlet (27.4; 6.2.2).

In the *solve*→*controls* menu, solution parameters were set for discretization type, Courant or CFL number, and under-relaxation factors. Discretization was either first- or second-order upwind for spatial order of accuracy and for time accurate cases was always second-order implicit for temporal order of accuracy. CFL numbers ranged from 5 to 10, based on whether the solution was stably converging, where a lower CFL number gives a more stable but slower converging solution and a higher CFL number gives quicker convergence but may not be numerically stable. Under-relaxation factors remained at the FLUENT default settings with one exception, since convergence and stability problems were typically corrected by adjusting spatial order of accuracy and/or CFL number; an exception was with the RSM, where under-relaxation factor for Reynolds stresses was changed from 0.5 to 0.8 because the Reynolds Stress equation variables were observed to converge quickly and stably.

Once models, schemes, discretization methods, boundary conditions and so forth were judiciously selected, reference values were established (in *report* menu) based on pressure farfield or inlet conditions. FLUENT-computed reference (or freestream) values included density, enthalpy, pressure, temperature, velocity, viscosity, and ratio of specific

heats; pressure (P_{INT} or P_{∞}), velocity and density values that were used are indicated in Table 3.1. A reference value which required user specification was area; for this case, that area was one-half the planform area, 0.033957 m^2 or 339.57 cm^2 . These reference dimensions and values were then used with pressure values on the wing surface to determine the integrated quantities, coefficients of lift and drag. Next the domain was partitioned along principal axes for parallel processing on between 6 and 20 processors; cases with larger memory and computing requirements, typically those with unsteady computations, more transport equations and/or finer mesh resolution, were assigned the greater number of processors. At this point, the domain was initialized from the farfield or tunnel inlet and computational iteration commenced.

Regarding determination of how many partitions to create within the model for parallel processing, in many cases a tradeoff was made between reducing computing time and having enough processors available to allow several different cases to run in concert with each other. Another consideration was whether the case would run on the Aspen cluster or the Hydra cluster, described in Chapter II; since the Aspen's processors were slower but more were available, its cases were run on a greater number of processors to give roughly equivalent computing time per iteration. In general, steady cases ran on 6, 8 or 10 processors and were partitioned accordingly, though steady cases with mesh adaptation, and hence more computational cells, ran on 10 or 20 processors – 10 processors when other cases needed to run and 20 when resources were more available. Steady cases converged on average after computing for 8 to 12 wall-clock hours; mesh-adapted steady cases required between 15 and 38 hours to converge, depending on the number of processors and number of cells in the domain. Unsteady cases ran on 10

processors when other cases were running but were later expanded to 16 or 18 to accelerate arrival at convergence. Unsteady cases achieved fully developed flow after 10-20 days of wall-clock time. As for a limitation on number of partitions in the domain, no specific study was performed.

Computational Plan of Attack

In general, a solution with second-order spatial and temporal accuracy is desired, and this was attained in all cases. In later cases the solver was initialized at second-order, with CFL = 10 for steady cases and 5 for unsteady cases, and successfully generated a second-order solution. Earlier farfield cases required running the first-order solution to convergence then changing the solver to second-order and running that solution to convergence, with CFL = 10 throughout. Exceptions included the k- ϵ and RSM steady cases which required CFL = 5 for stability. These CFL values were obtained through trial and error but were based initially on FLUENT recommendations (FLUENT, 2001: Tutorials 3 and 4).

Has it Converged Yet?

Convergence is attained when the solution no longer changes with more iterations or has reached a fully developed flow for an unsteady case. An indicator for steady-state convergence is the error residual, where error residuals for FLUENT's coupled solver are defined as the square root of the averaged time rate of change for each flow variable within the domain – basically the difference in each variable from one iteration to the next. Residuals may be monitored either automatically by FLUENT or manually by the user to determine when to stop iterating the solution. A general guideline for steady convergence is when the residuals have decreased by three orders of magnitude;

however, this does not necessarily hold true for turbulent unsteady cases, where it was observed that some residuals reduced by as many as seven orders of magnitude while others reduced only by three (FLUENT, 2001: 22.16.1, 22.19.1).

Occurrence of non-converging residuals necessitates other criteria for convergence, including monitoring for steady C_L , C_D and outlet mass flow rate (or percent change in mass flow rate). Once C_L and C_D have little or no change from one iteration (steady) or time step (unsteady) to the next, the solution has converged. Also mass flow rate may be monitored at the outlet surface or mass flux reports may be computed to determine whether mass flow is conserved, where acceptable mass flow imbalance should be no more than 0.5% through the domain (FLUENT, 2001: 22.16.3-4, Tutorial 4). See Figure 3.23 for an example of convergence shown by steady C_L and C_D .

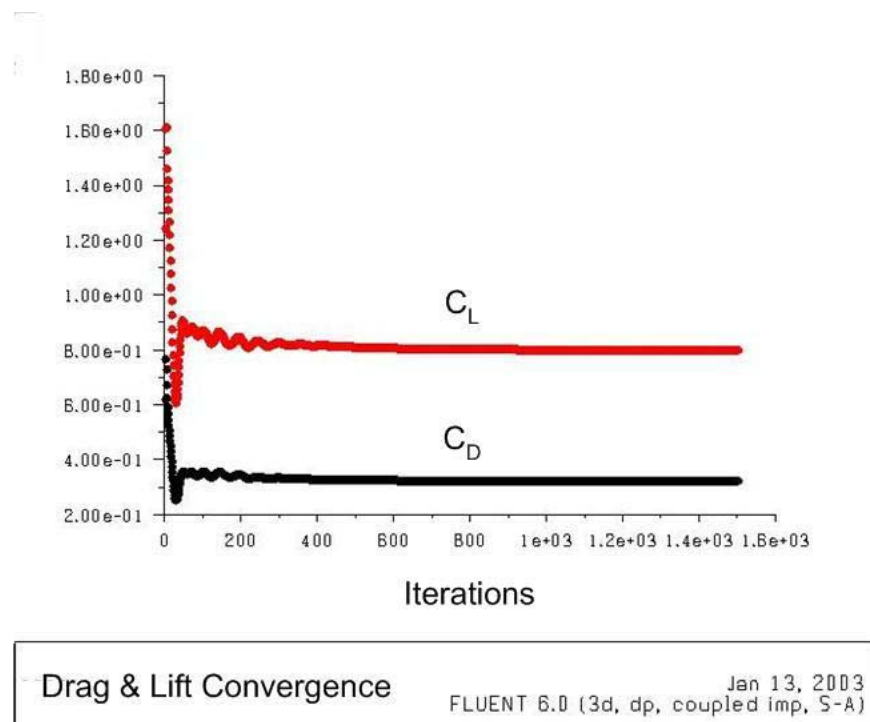


Figure 3.23 – Drag and Lift Convergence for Revision L, $\alpha = 18^\circ$, $V_\infty = 16$ m/s, Spalart-Allmaras Steady Case

Another possible value to monitor for convergence, though at one specific point, is the pressure coefficient, C_P . It is calculated as

$$C_P = \frac{p - P_{INIT}}{P_{DYN}} \quad (3.2)$$

where p is *local static pressure*, P_{INIT} is *reference or ambient pressure*, and P_{DYN} is *reference dynamic pressure*,

$$P_{DYN} = 0.5 \cdot \rho_\infty \cdot V_\infty^2 \quad (3.3)$$

with tabulated values for the various freestream velocities in Table 3.1 (FLUENT, 2001: 27.4). In this study C_P was not monitored for solution convergence, but its distributions were used to compare solutions from different meshes and turbulence models with wind tunnel test data.

For all steady cases, second-order solution convergence was achieved with between 1,100 and 2,100 iterations. For unsteady cases, second-order solution convergence was less obvious. In these cases, the error residuals reduced overall by between three and seven orders of magnitude – typically one to two orders within each implicit time step, mass flow rate was conserved to within a few thousandths of a percent, but while C_L and C_D values developed a stationary, periodic cycle in time, they did not reach “steady” values. After two seconds in dimensional time, or about 4.5 flow cycles, the flow was declared fully developed since average C_L and C_D values were then degrading/decreasing by only 0.4% per flow cycle. This compared to acceptable variation computed in a similar study, where C_L varied by 1.6% within a flow cycle (Ekaterinaris, Schiff, 1990: 61, 65). At a step size of 0.0004 sec, this fully developed and mass-conserved flow required 5,000 time steps at the FLUENT-recommended 20

iterations per step (FLUENT, 2001: 22.15.1), for a total of 100,000 iterations. Within each time step, the 20 iterations generally resulted in one to three orders of magnitude reduction in error residuals for the flow, continuity, energy and transport variables. Depending on the number of processors used in parallel, fully developed unsteady solutions required between 278 (11.6 days) and 472 (19.7 days) wall-clock hours.

Determination of “Correct” Initial Conditions

Studies were performed to determine initial conditions which would give an acceptable solution prediction. Impetus for these sub-studies arose from uncertainty in the experimental setup and resulting data, where no tolerance was initially given for the freestream velocity measurement, $V_\infty = 15$ m/s, where the wing’s angle of attack was not precisely measured, and where consideration must be given for scraped and gouged wing surfaces and a leading edge subjected to light grinding, which diminished its sharpness and gave it a slight curvature not modeled. As mentioned in Chapter I, V_∞ was determined to be 15.4 m/s, based on atmospheric data, but without benefit of a tolerance or error bar. These factors led to the decision to adjust the wing’s angle of attack and the freestream velocity, based on engineering judgment, to compensate for testing uncertainty and to give a closer correlation between numerical prediction and experimental data.

For these evaluations primary consideration was given to how closely C_p data compared with the experiment and how closely C_L compared with Polhamus’ theoretical value, since lift had not been experimentally determined for this setup. Using Equations

1.1, 1.3 and 1.4, and determining K_P and K_V coefficients from Polhamus' plots, for $\alpha = 15^\circ$, $C_L \approx 0.7866$ (Polhamus, 1971; Polhamus, 1966).

Selection of Freestream Velocity

Results from earlier cases, using mesh Revisions H and K, showed that varying freestream velocity (increasing it from 15 m/s to 17 or 25 m/s) did not affect C_P predictions because it increased magnitude of dynamic and local pressures in proportion to each other; increased velocity also did not significantly change C_L , where the increase to 25 m/s resulted in a 1.7% increase in lift coefficient. Thus $V_\infty = 16$ m/s was chosen because it increased local static pressures closer to the experimentally determined values without significantly increasing the reference dynamic pressure (150 Pa) above the average measured value (143 Pa) and because it was within a reasonable tolerance of the estimated 15.4 m/s wind tunnel condition.

Selection of Wing Angle of Attack

Using mesh Revision L, cases were run for angles of attack, $\alpha = 15, 16, 18, 19, 20$ and 21° , using the Spalart-Allmaras (S-A) turbulence model in steady state and $V_\infty = 16.0467$ m/s. C_L values from several experiments, from this study, and from Polhamus are listed in Table 3.2. The "Experiment" C_L value came from testing performed at Louisiana State University several years ago, where the same wing was attached to a half-fuselage. Those results showed that such a configuration creates an effective increased angle of attack so C_L for the wing without fuselage would be somewhat less, likely less than the theoretical value (Guillot, 1999: 33). In Chapter I and as shown by empirical data from Wentz, Kohlman, Seginer and Salomon in Table 3.2, it was

established that Polhamus' estimation tended to be high, so cases were eliminated with C_L greater than about 0.79, leaving as options cases for $\alpha = 15, 16$ and 18° . Note also that numerically estimated C_L values correspond closely with experimental data in the table; this validates the steady, S-A numerical model's ability to accurately predict C_L .

Table 3.2 – Comparison of Lift Coefficient Resulting from Various Angles of Attack

Case	α (deg)	V_∞ (m/s)	C_L
Experiment ^a	~15	~15.4	0.81
Theory (Polhamus)	15	~0	0.7866
	18	~0	0.9614
Wentz, Kohlman ^b	15	18	0.72
	18	18	0.80
Seginer, Salomon ^c	15	30	0.70
	18	30	0.84
Revision L (S-A)	15	16.0467	0.6851
	16	“	0.7240
	18	“	0.7974
	19	“	0.8268
	20	“	0.8587
	21	“	0.8812

^a Results with fuselage attached to wing (Guillot, 1999: 32)

^b Delta wing with $\Lambda=60^\circ$, sharp leading edge but only 20% of wing thickness in current study (Wentz, Kohlman, 1971: 157-158)

^c Delta wing with $\Lambda=60^\circ$ and relatively sharp leading edge (Seginer, Salomon, 1986: 803-804)

Other factors affecting lift coefficient include whether the wing was mounted flush against the tunnel wall, whether inlet flow was laminar or turbulent, and whether boundary layer refreshing was done. The difference between mesh Revisions J and K, for same angle of attack, was that the wing was flush against the wall in Revision K; this increased C_L by 5.0%. With Revision K, two cases were run with TVR set at 1 and 10, all other conditions being the same; the case with TVR = 10, or turbulent inlet flow, increased C_L by 0.6%. Mesh Revision J differed from Revision H in that it simulated boundary layer refreshing by removing nearly 2 m of tunnel wall upstream of the wing;

this change resulted in increasing C_L by 10.1%. Neglecting the insignificant difference created by varying inlet turbulence, Revision L incorporated both mounting wing flush with the wall and introducing a boundary layer refresher plate.

The observations above did not conclusively indicate which angle of attack should be used in the numerical model, since C_L data were not available from testing in this configuration. Therefore, the following detailed comparisons of C_P data, Figures 3.24-27, were used instead, which indicated that the best option for angle of attack was $\alpha = 18^\circ$.

Figure 3.24 contains data along the chordwise location, $x/c = 0.35$, from the experiment conducted at University of Cincinnati, seen as a blue line with a square marker for each pressure sensor location in the spanwise direction. Each experimental data point was calculated using Equation 3.2, where p was *pressure measured at that specified location*, P_{INIT} was *ambient pressure in the lab*, and P_{DYN} was *dynamic freestream pressure measured in the wind tunnel*. This resulted in negative pressure coefficients, but they were plotted on a positive scale for easier viewing, as is common practice. Numerical solutions, at the various angles of attack, are shown as lines with no markers except for the $\alpha = 18^\circ$ case, which is indicated as a black line with markers. Numerical data points corresponding to predicted static pressure values were extracted from the solution along the spanwise line at chordwise location, $x/c = 0.35$, and were plugged into Equation 3.2 to yield the according C_P . This procedure was performed instead of using the FLUENT-computed C_P values to allow greater semblance to the procedure for calculating experimental C_P . Figures 3.25-27 provide data for $x/c = 0.55$, 0.75 and 0.95, respectively.

In the following observations, numerical cases with $\alpha = 15$ and 16° are referred to as “lower-alpha cases,” and $\alpha = 19, 20$ and 21° are “higher-alpha cases.” In Figure 3.24, $\alpha = 18^\circ$ is the best case because its slope is better than those of the higher-alpha cases and its magnitude is greater than the lower-alpha cases. While its magnitude is lower than the higher-alpha cases, it maintains better C_L correlation. The same arguments hold for the remaining figures, and note in Figures 3.26 and 3.27 that the $\alpha = 18^\circ$ case has the greatest peak value and has a slope which closely matches that of the experimental data. Of prime importance is the model’s ability to closely approximate the solution in the region inside and following vortex breakdown at or near $x/c = 0.4$, and the $\alpha = 18^\circ$ case indeed appears to do this. Furthermore, this case clearly predicts pressure values with greater accuracy than the $\alpha = 15^\circ$ case.

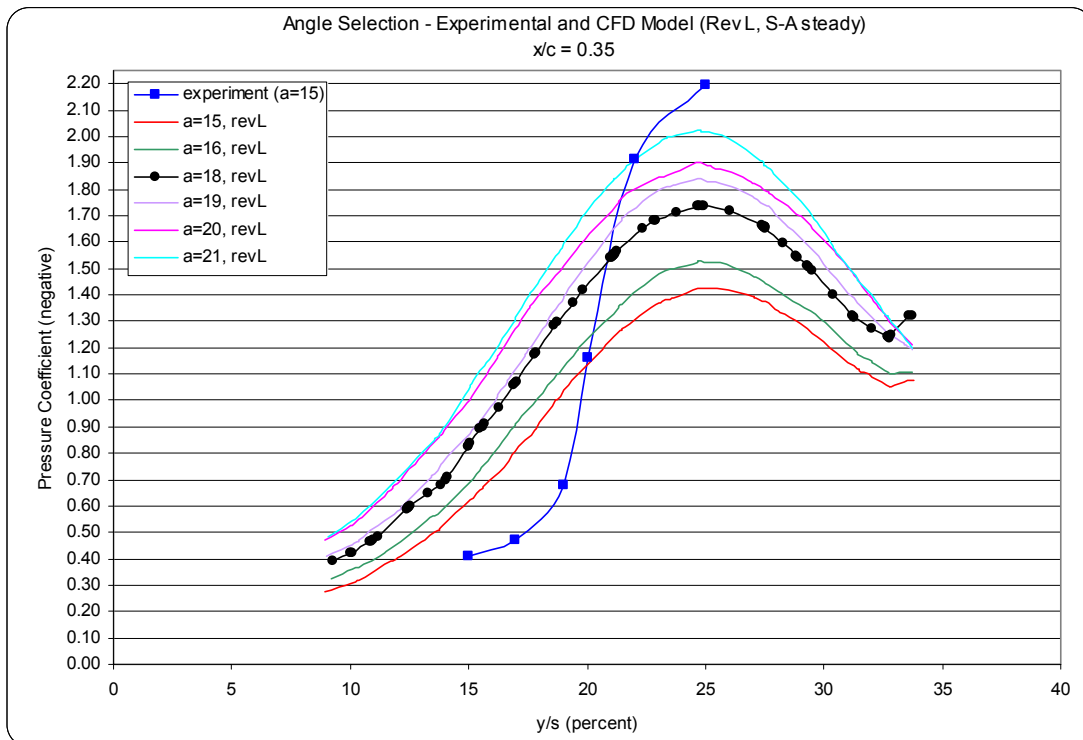


Figure 3.24 – Angle Selection Data at $x/c = 0.35$ (Mesh Revision L, Steady S-A)

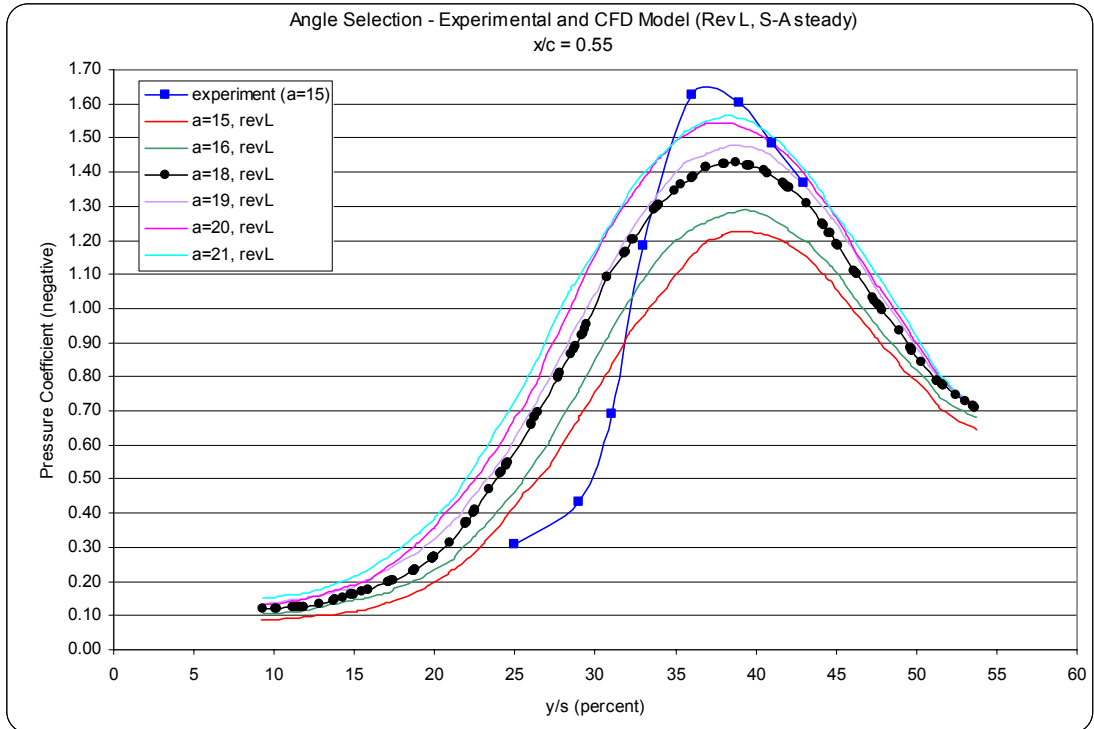


Figure 3.25 – Angle Selection Data at $x/c = 0.55$ (Mesh Revision L, Steady S-A)

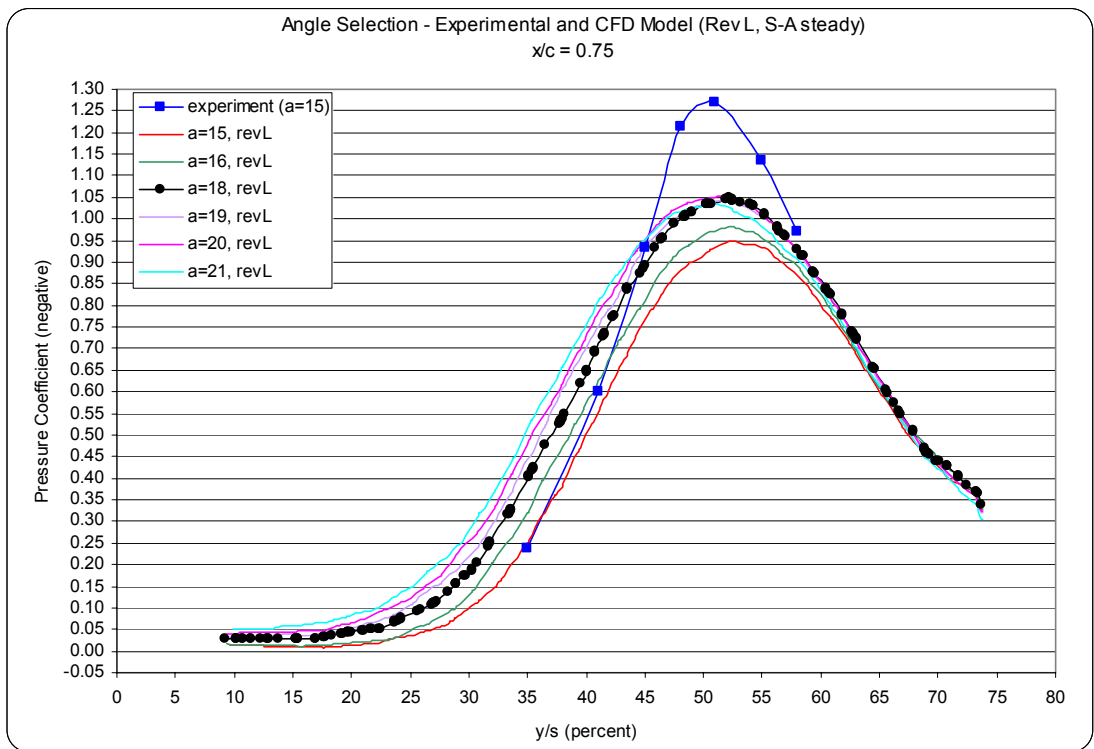


Figure 3.26 – Angle Selection Data at $x/c = 0.75$ (Mesh Revision L, Steady S-A)

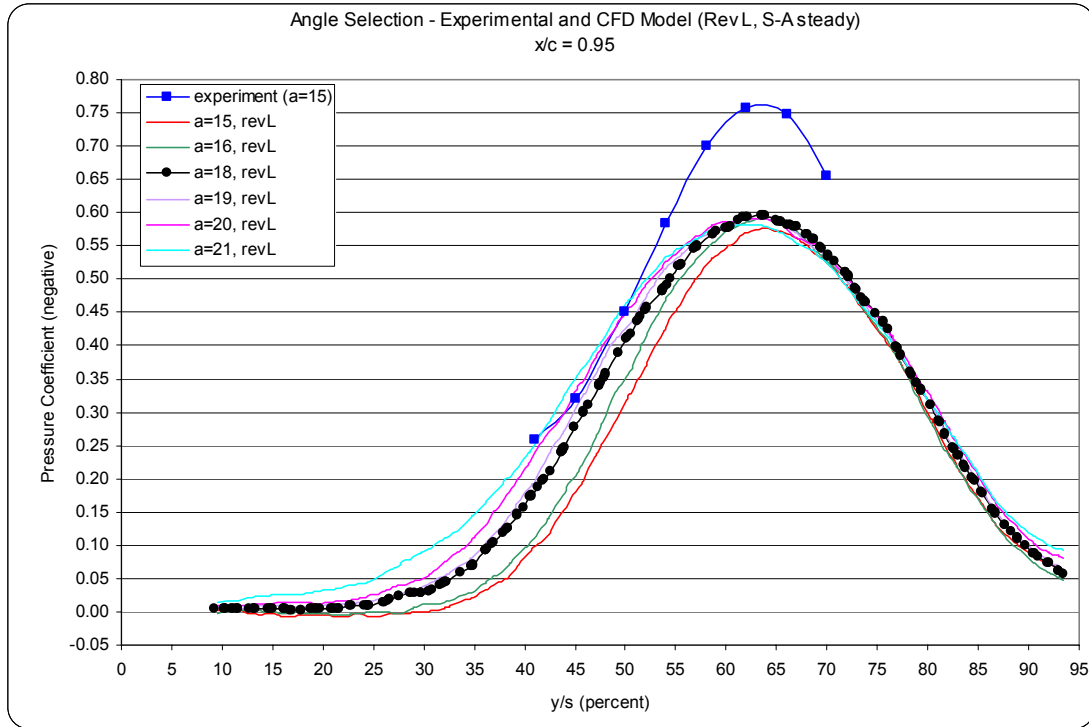


Figure 3.27 – Angle Selection Data at $x/c = 0.95$ (Mesh Revision L, Steady S-A)

Therefore, to compensate for uncertainties in experimental measurement and procedure, this study’s final or best numerical mesh and flow model set the wing at 18° angle of attack and freestream velocity at 16 m/s. It must be pointed out that these sub-studies were performed using the steady solver with S-A turbulence model; the section on time accurate solutions later in this chapter shows, however, that more accurate solutions (i.e., those which more precisely model the highly unsteady nature of the flow) used an unsteady formulation. However, since the steady S-A results did show good correlation with experimental findings, the initial conditions above were deemed acceptable.

Results

Effect of Model Geometry

The initial numerical mesh through Mesh Revision F included the wing, offset from a no-slip wall boundary, and a pressure farfield which extended to various dimensions from the wing. It was likely a flawed approach to include a constraining wall in this manner, particularly since that wall eventually exceeded the dimensions of the equivalent adjacent wall in the wind tunnel experiment. Better options could include modeling the experimental setup, as was done in ensuing mesh revisions, or to establish a symmetry plane instead of a wall in the farfield cases, where a symmetry plane would ensure no wall boundary layer influence on the wing. However, a case with symmetry plane would resemble even less the actual experimental setup, thus that option was not exercised. The following C_P plots, compared with experimental data, Figures 3.28-31, show that none of the farfield models adequately predicted the experimental results.

For each solution, the steady case used the S-A turbulence model, $\alpha = 15^\circ$ and $V_\infty = 15$ m/s, largely for the sake of consistent evaluation; while none of these solutions could be precise with a steady solver (refer to discussion in Chapter I), relative comparison was sufficient for establishing the most suitable model with which further investigation could proceed. As an additional note on using a steady solver to ascertain the best configuration to run the unsteady cases: steady solutions predicted C_P values closer to experimental values than did any unsteady solution, because steady or time averaged solutions more precisely represent the experimental data, which were also time averaged; however, to reiterate, steady solvers cannot accurately predict all the flow physics involved with vortex generation and particularly vortex breakdown. Thus the

preferred model should be able to adequately predict C_P data *and* physics of flow, specifically vortex strength (velocity and pressure) and location of vortex breakdown.

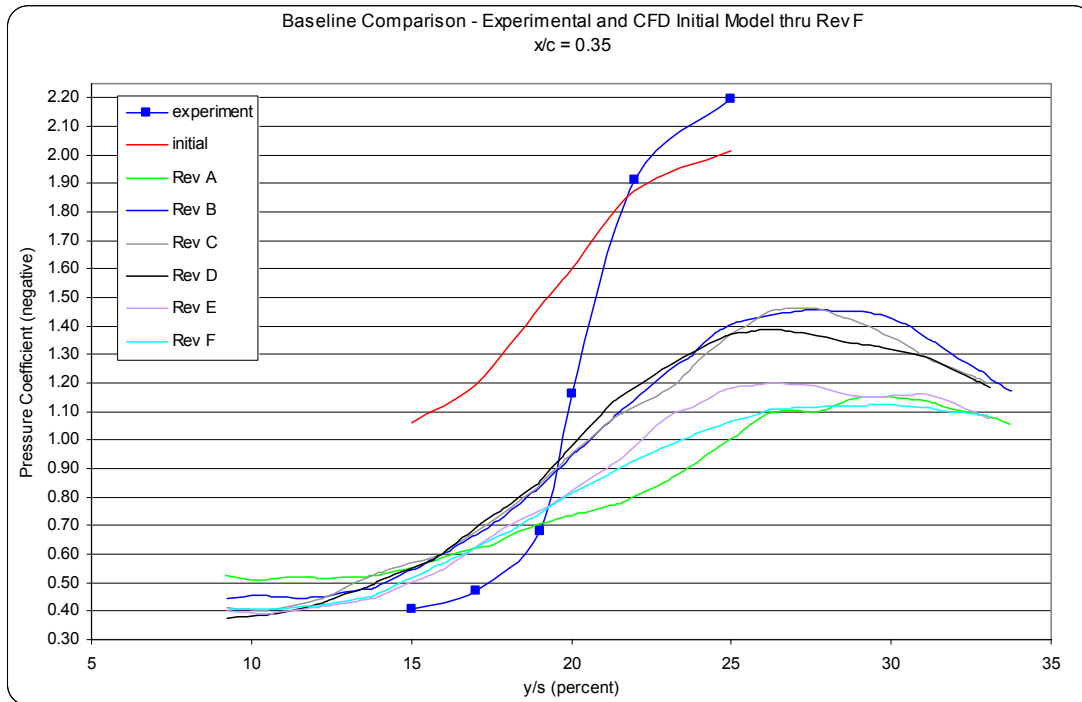


Figure 3.28 – C_P Comparison of Initial through Mesh Revision F at $x/c = 0.35$ (Steady S-A, $\alpha = 15^\circ$, $V_\infty = 15$ m/s)

In Figures 3.28-31, C_P predictions generated by the solution from the initial numerical mesh are indicated by a red line, experimental data are indicated by a blue line with square markers, and predictions from mesh Revisions A-F are indicated by green, blue (no markers), gray, black, purple and light blue, respectively. In each of the plots, the peak values (actually a minimum negative value) indicate the experimentally determined or numerically predicted center location of the vortex core, since a large negative coefficient represents a static pressure lower than ambient conditions, which corresponds also to an area of higher velocity. The initial mesh tended to result in overestimated C_P predictions but was reasonably close in prediction of vortex peak location, because the initial numerical model gave no offset between wing and wall.

Revisions A-F predicted vortex peak locations which strayed from the experimentally determined location by 3-6%. This likely corresponds to the numerical wing being offset from the wall by 1.27 cm, which is 6.1% of the half span, representing an effectual decrease in angle of attack or an increase in sweep angle. In Figure 3.28, the early Revisions – B, C and D – provided the greatest relative improvement by enlarging the numerical domain downstream and spanwise, while Revisions E and F resulted in worse predictions because their upstream expansions resulted in greater boundary layer generation along the wall, thus negating the experiment’s boundary layer refreshing. Note similar trends in Figures 3.29-31. At $x/c = 0.35$, Revisions A-F predicted peak values with an error between 34 and 49% of the experimentally determined peak, which is of course unacceptable. These Revisions’ errors were about 10-33% at $x/c = 0.55$, 2-23% at $x/c = 0.75$, and 1-21% at $x/c = 0.95$. These results would be marginally acceptable if C_P magnitude were the only criterion, but that was not the case.

All of the numerical meshes result in better pressure prediction in these plots as the flow advances downstream over the wing surface; this is likely because vortex energy increases with increasing turbulence, and as a result pressure decreases and gives a larger negative pressure coefficient. It may also be a function of numerical grid resolution, where finer resolution may be required near the apex to resolve the smaller vortex diameter and higher rotational velocity. While it appears that Revision B gave the closest estimations, its domain did not contain the flow solution; also while Revisions D, E and F did contain the solution (extent of vortex) within the computational domain, they either failed to provide domain extents acceptable for low subsonic flow (as with Revision D,

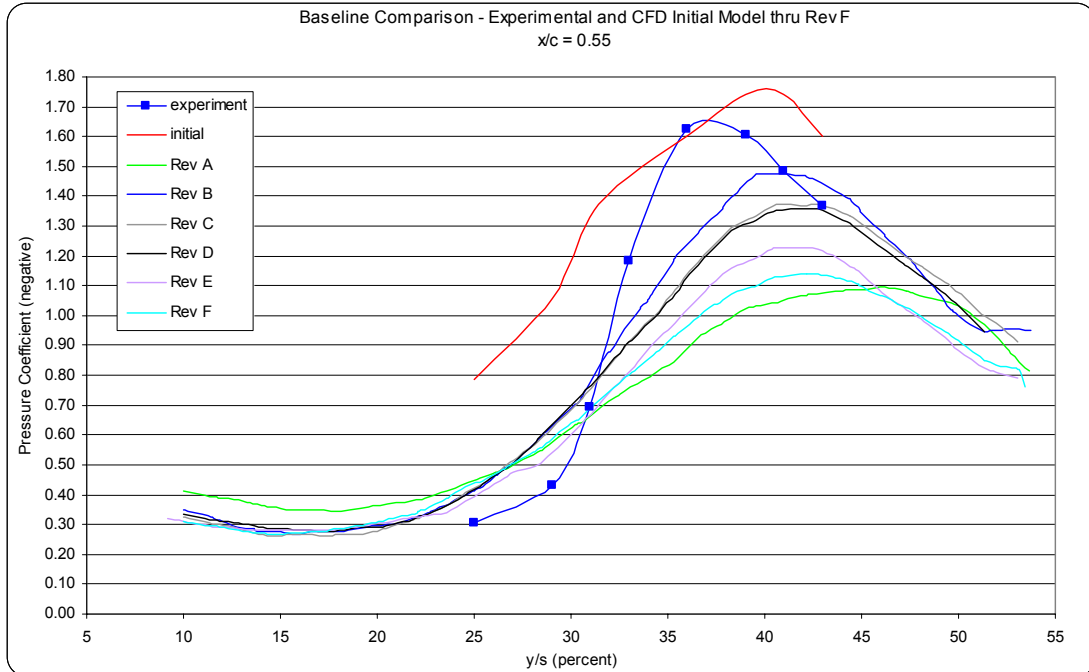


Figure 3.29 – C_P Comparison of Initial through Mesh Revision F at $x/c = 0.55$
 (Steady S-A, $\alpha = 15^\circ$, $V_\infty = 15$ m/s)

which needed more upstream extent) or failed to provide results within an acceptable margin of the experimental data. Again, none of Revisions Initial through F adequately predicted vortex location or C_P values at $x/c = 0.35$. Farther downstream on the wing surface, these models predicted closer C_P magnitudes because flow became more turbulent in this region, but they still failed to predict the correct vortex location. This lack of improvement in predictions led to creation of numerical meshes which included the wind tunnel (Revisions G-J) and boundary refresher plate (Revisions K-O).

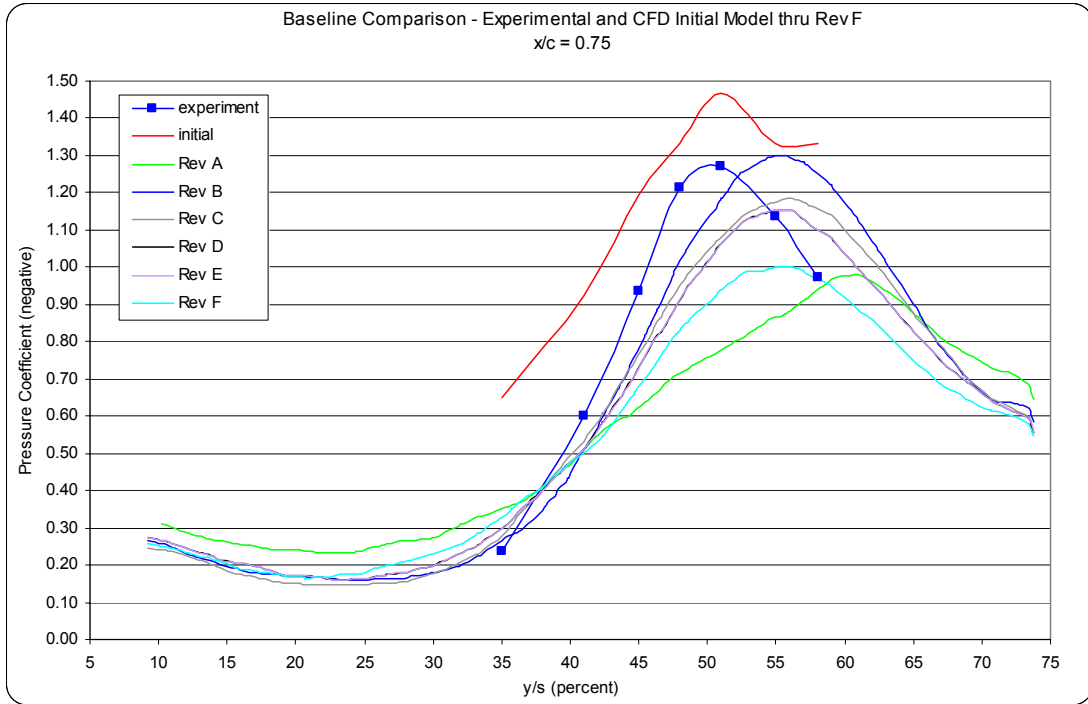


Figure 3.30 – C_P Comparison of Initial through Mesh Revision F at $x/c = 0.75$
 (Steady S-A, $\alpha = 15^\circ$, $V_\infty = 15$ m/s)

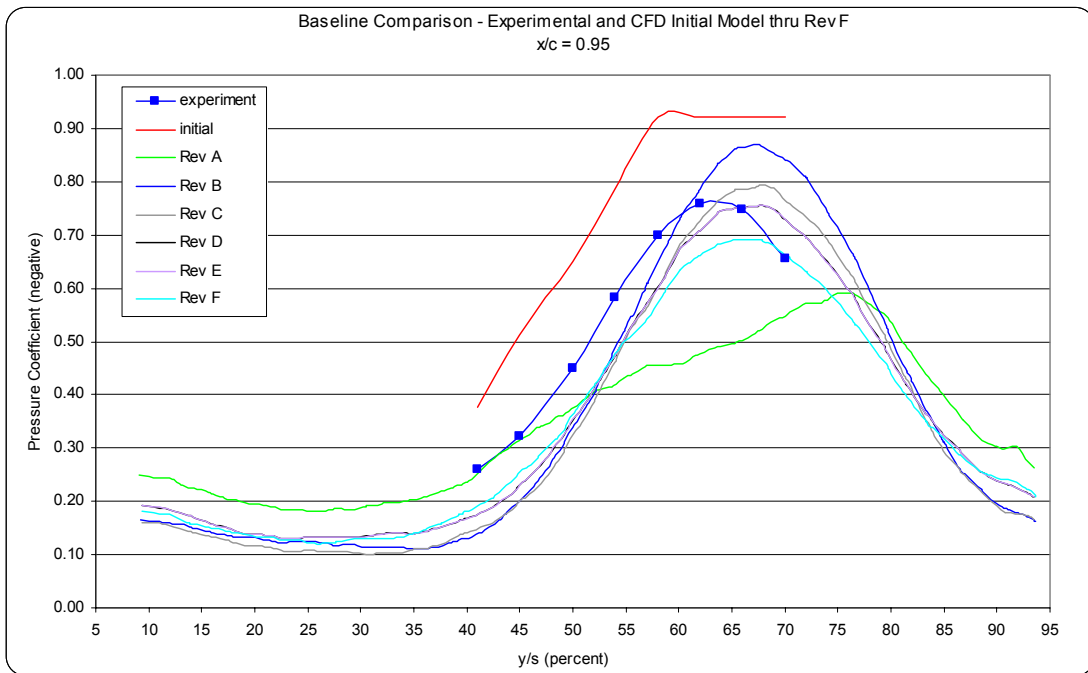


Figure 3.31 – C_P Comparison of Initial through Mesh Revision F at $x/c = 0.95$
 (Steady S-A, $\alpha = 15^\circ$, $V_\infty = 15$ m/s)

To review the changes implemented in the next mesh revisions: Revision G modeled the wind tunnel with wing offset from the wall and with tunnel inlet 2 m upstream of the wing (results were not obtained for Revision G, since it was revised before a converged solution was obtained); Revision H improved resolution in the boundary layer region and maintained the wing's offset from the wall and the tunnel inlet location; Revision I maintained the wing offset but truncated the tunnel inlet location to about two chords upstream of the wing apex to assess the impact of boundary layer flow over the wing; Revision J still maintained the wing offset from the tunnel wall and reduced the inlet distance to several centimeters upstream of the wing apex, the first intentional attempt to simulate boundary layer refreshing; Revision K placed the wing flush against the tunnel wall and corrected the distance (shorter) between wing apex and leading edge of refresher plate; Revision L included the refresher plate's 45° ramp or bevel and replaced the tunnel inlet to 2 m upstream of the wing apex; and Revision O modeled the wing flush against the refresher plate, which plate was then offset from the tunnel wall, and tunnel inlet at 2 m from the wing. Revision O came as an afterthought to validate or refute the assumption of placing the refresher plate flush against the tunnel wall, and its evaluation showed the assumption for Revision L was good and allowed for a simpler numerical geometry.

All of the above meshes modeled 5 m of tunnel downstream of the wing, and in the following comparisons used the steady solver, S-A model, $\alpha = 15^\circ$ and $V_\infty = 15$ m/s, except Revision L used $V_\infty = 16$ m/s. (As noted earlier in this chapter, the slightly higher freestream velocity showed no effect on C_p values.) Also the comparison between Mesh

Revisions L and O used $\alpha = 18^\circ$, $V_\infty = 16$ m/s, and the steady RSM turbulence model, since the S-A model introduced instability in the solver for Revision O.

In Figures 3.32-35, data at the four chordwise locations ($x/c = 0.35, 0.55, 0.75$ and 0.95) are shown by a blue line with square markers for the experiment and by lines with no markers of colors, green, blue, gray, black and red for predictions from Mesh Revisions H-L, respectively.

In these plots, Revisions K and L give the closest prediction of peak C_p location, which corresponds to vortex core centerline, because they both model the wing as flush against the wall; Revisions H-J incorrectly model the wing as offset from the wall. Revision L predicts closer than does Revision K to the experimentally determined centerline at all chordwise locations except $x/c = 0.35$, where they predict the same location. This is because Revision L resembles more closely the actual experimental setup, which includes boundary layer buildup from the 2 m of tunnel wall upstream of the wing.

While some discussion of C_p magnitude follows, primary consideration must be given to the model which most closely predicts vortex core location because development of this model is intended ultimately to be part of a control system which needs to direct blowing momentum into the vortex core. To do this, the vortex core location must be accurately predicted. Since these data are all time averaged, including the experiment, except for the row of sensors upstream of vortex breakdown (at $x/c = 0.35$) none of them shows a true location of the vortex core, since it meanders back and forth in time in a spanwise direction once vortex bursting has occurred (see Chapter I for more information and references); this phenomenon is shown in later unsteady cases. Nonetheless, steady

modeling provided relatively accurate predictions from the varied numerical meshes and thus serves to identify the best numerical mesh.

In these comparisons, little consideration is extended to actual predicted C_p magnitudes because they were subsequently altered to more closely match experimental data by adjusting wing angle of attack; hence relative comparisons are made to determine the best computational grid. Revision H clearly predicted the least accurate solution at all locations. Also at each location, Revisions I and J which progressively truncated the distance between wing apex and tunnel inlet, showed marked improvement over Revision H results. This indicated the clear need for boundary layer refreshing in the numerical model. Revision K's results showed the combined effect of moving the wing to be flush with the wall and again reducing distance to the tunnel inlet. Thus at each chordwise position, the C_p peak moved closer to that of the experimental data, and C_p magnitudes increased at $x/c = 0.35$ and 0.55 . For $x/c = 0.75$ and 0.95 , Revision K's predicted C_p magnitudes increased over those of Revision J, as shown moving a spanwise outward direction in Figures 3.34 and 3.35, but then it predicts lower peak values around the vortex core. This indicates the advantage of a fresher boundary layer was then overridden by boundary layer or other viscous effects from having the wing flush against the tunnel wall and from interaction with flow over the other tunnel walls. This also showed that wall or boundary layer effects from the tunnel have a diminishing influence on prediction of vortex strength in the region aft of vortex breakdown. Revision K, however, was superior to Revision J because it better predicted vortex centerline location. Revision L's introduction of the boundary layer plate and extended upstream tunnel, as opposed to approximating by a closer tunnel inlet, resulted in decreased vortex strength

but more accurate vortex core position. Clearly, structure of flow approaching the wing is one of the more significant factors affecting solution accuracy. Therefore, Mesh Revision L was selected for further investigations because it most closely predicted vortex centerline position and it most closely modeled the experimental setup.

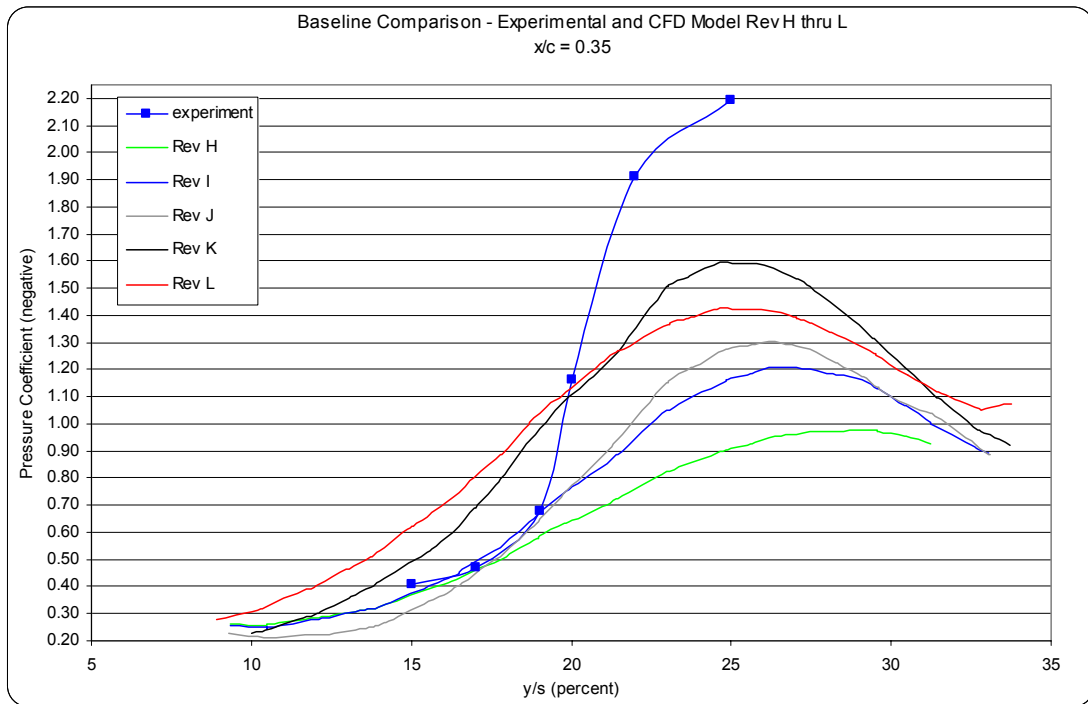


Figure 3.32 – C_p Comparison of Mesh Revision H through L at $x/c = 0.35$ (Steady S-A, $\alpha = 15^\circ$, $V_\infty = 15$ m/s (except for RevL, $V_\infty = 16$ m/s))

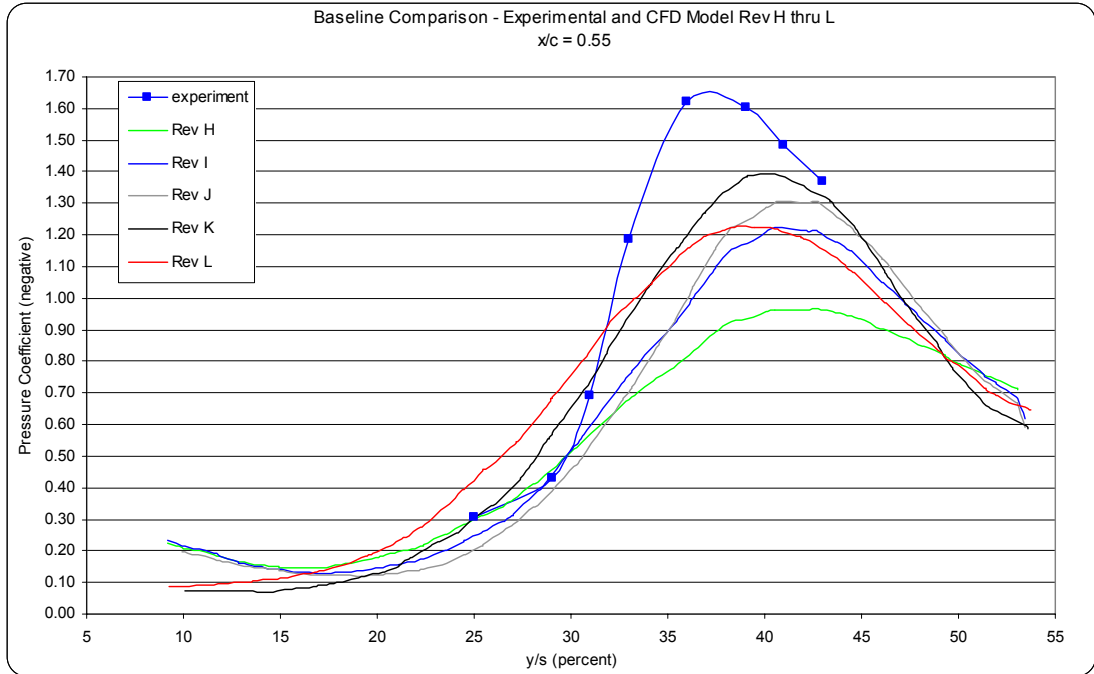


Figure 3.33 – C_p Comparison of Mesh Revision H through L at $x/c = 0.55$ (Steady S-A, $\alpha = 15^\circ$, $V_\infty = 15$ m/s (except for RevL, $V_\infty = 16$ m/s))

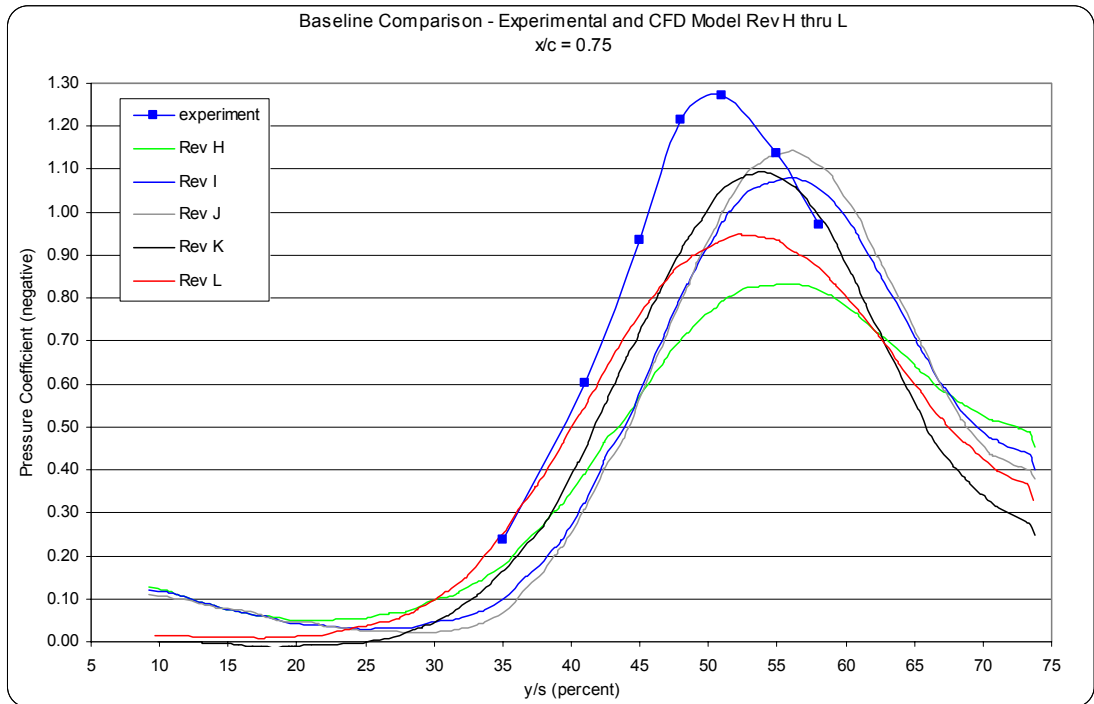


Figure 3.34 – C_p Comparison of Mesh Revision H through L at $x/c = 0.75$ (Steady S-A, $\alpha = 15^\circ$, $V_\infty = 15$ m/s (except for RevL, $V_\infty = 16$ m/s))

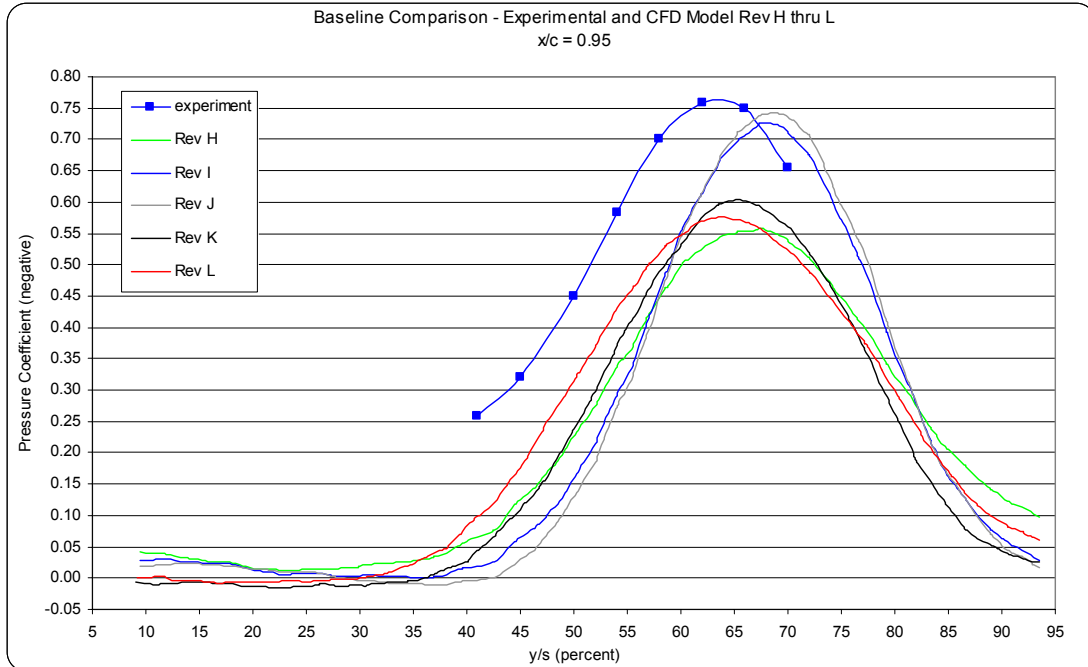


Figure 3.35 – C_p Comparison of Mesh Revision H through L at $x/c = 0.95$
 (Steady S-A, $\alpha = 15^\circ$, $V_\infty = 15$ m/s (except for RevL, $V_\infty = 16$ m/s))

To lend further validity to the assertion that Mesh Revision L was superior to Revision K, Figure 3.36 compares experimental and predicted C_p values, where all four chordwise data sets are captured in one plot and where solutions from Revisions K and L were computed with $\alpha = 18^\circ$ and $V_\infty = 16$ m/s. These data show that while Revision K does better at $x/c = 0.35$, Revision L predicts a solution comparable or better at the other chordwise locations.

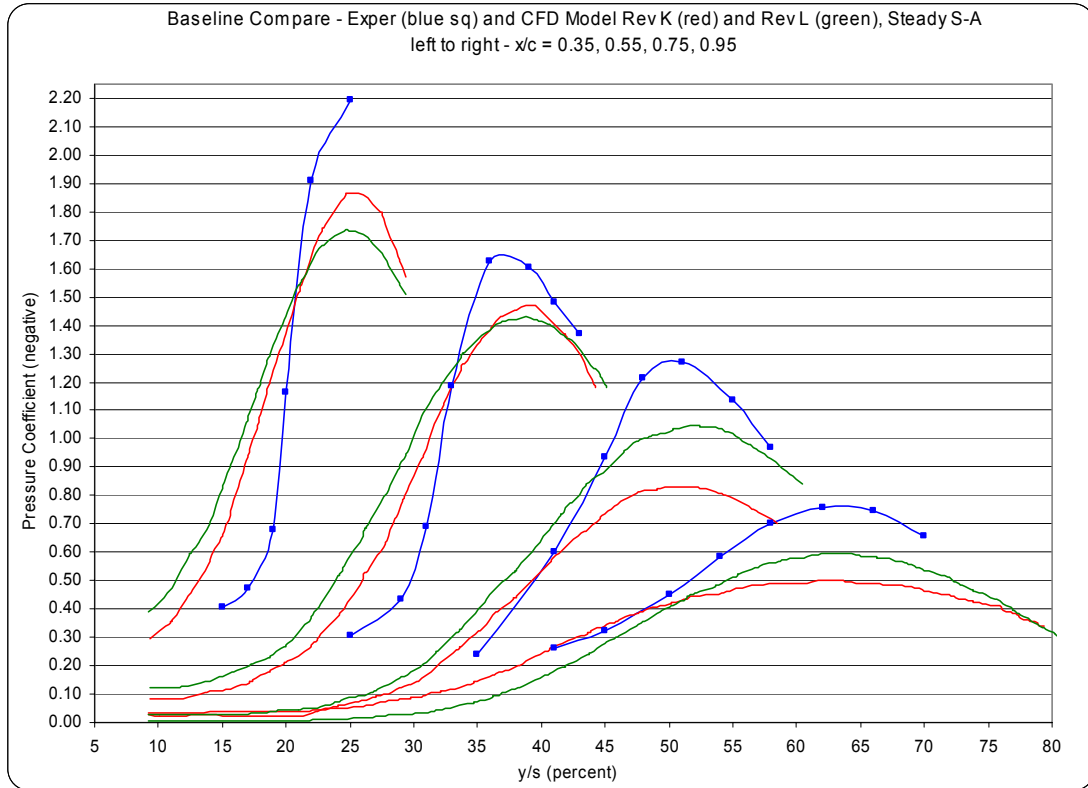


Figure 3.36 – C_P Comparison of Revisions K and L (Steady S-A, $\alpha = 18^\circ$, $V_\infty = 16$ m/s)

A final consideration in determining correct numerical model geometry for the flow model was to evaluate the effect of the boundary layer refreshing plate's placement – flush with or offset from the tunnel wall. Using the steady RSM turbulence model, Revision L's solution computed $C_L = 0.740$ and Revision O gave $C_L = 0.768$, thus Revision O resulted in a C_L prediction closer to theoretical and experimental values, shown earlier in Table 3.2. Data in Figure 3.37 show that Mesh Revision O's (green line) geometry gives slight improvement in C_P magnitude and slope over that of Revision L; however, using the steady RSM solver, neither computational mesh resulted in close comparison with experimental results. In addition to comparing C_P and C_L values, a qualitative comparison between boundary layers follows in Figures 3.38 and 3.39.

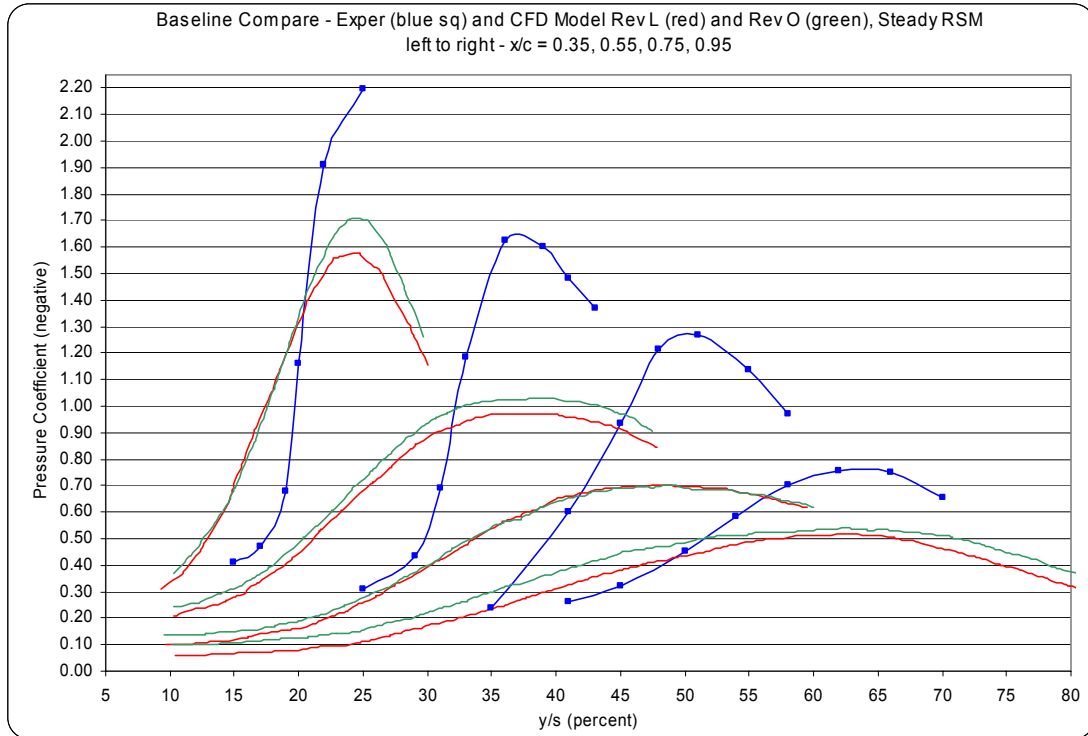


Figure 3.37 – C_p Comparison of Revisions L and O (Steady RSM, $\alpha = 18^\circ$, $V_\infty = 16$ m/s)

In Figures 3.38 and 3.39, velocity predictions were nondimensionalized with the freestream velocity then truncated at $V/V_\infty = 0.50$, where V is *velocity magnitude*, for cleaner viewing of the layer. The only noteworthy difference between these two figures is that Figure 3.39 shows formation of a thicker boundary immediately upstream of the refresher plate leading edge, which thickness then disappears into the gap; otherwise, the boundary layer flow approaching the wing in each case is nearly identical with or without an offset between the refresher plate and tunnel wall.

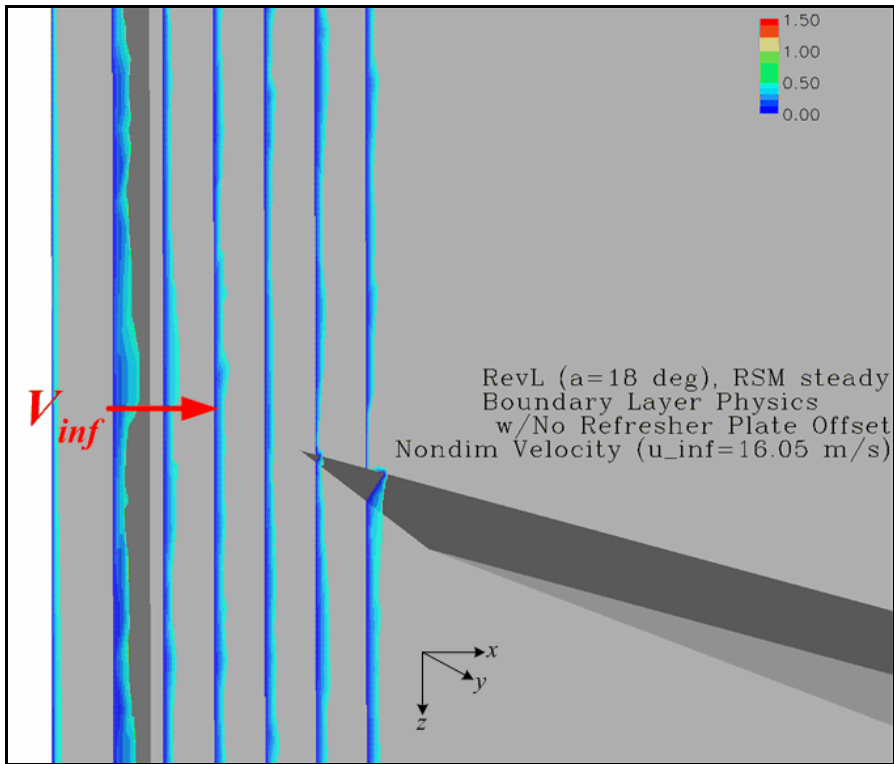


Figure 3.38 – Boundary Layer Effects with Refresher Plate Flush with Tunnel Wall

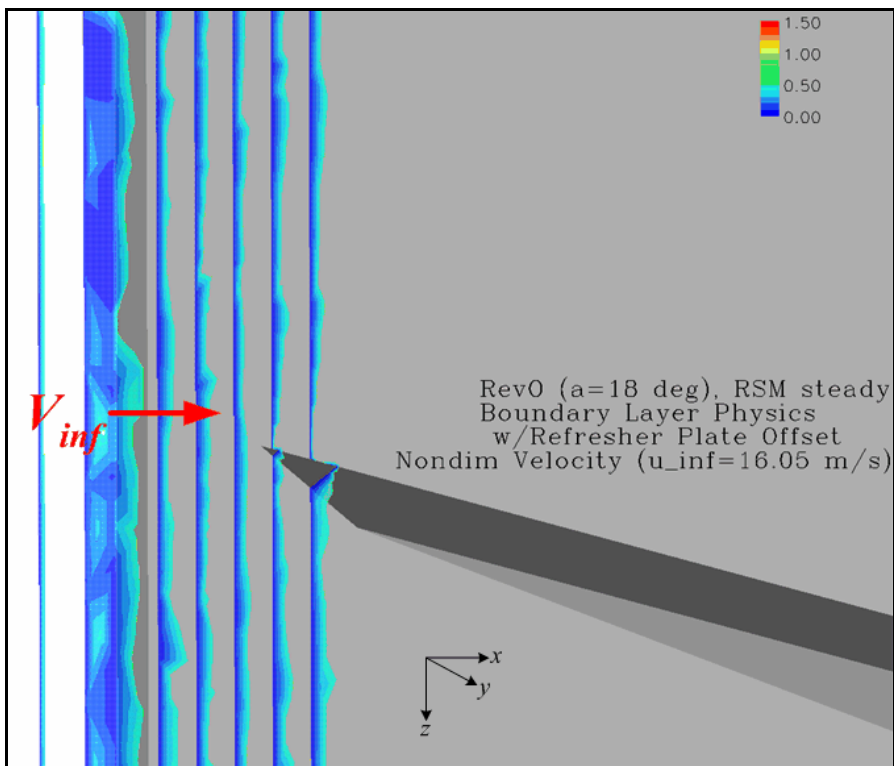


Figure 3.39 – Boundary Layer Effects with Refresher Plate Offset from Tunnel Wall

Figure 3.40 shows via streamlines that flow around the boundary layer refresher plate is laminar and steady, unless or until the flow rolls into vortex effects, as observed with the purple streamlines. The black streamlines indicate that flow over the refreshing plate upper surface is undisturbed until it mixes with the downstream turbulence from the vortex and its breakdown, shown with blue streamlines. While Mesh Revision O, compared with Revision L, apparently gives slightly more accurate C_P and C_L predictions and does not overly complicate the flow field, its computation required 15.4% more time per iteration and 20% more memory. Therefore, results using the modeled approximations of Mesh Revision L were deemed acceptable, and the assumption of placing the refresher plate flush against the tunnel wall was appropriate.

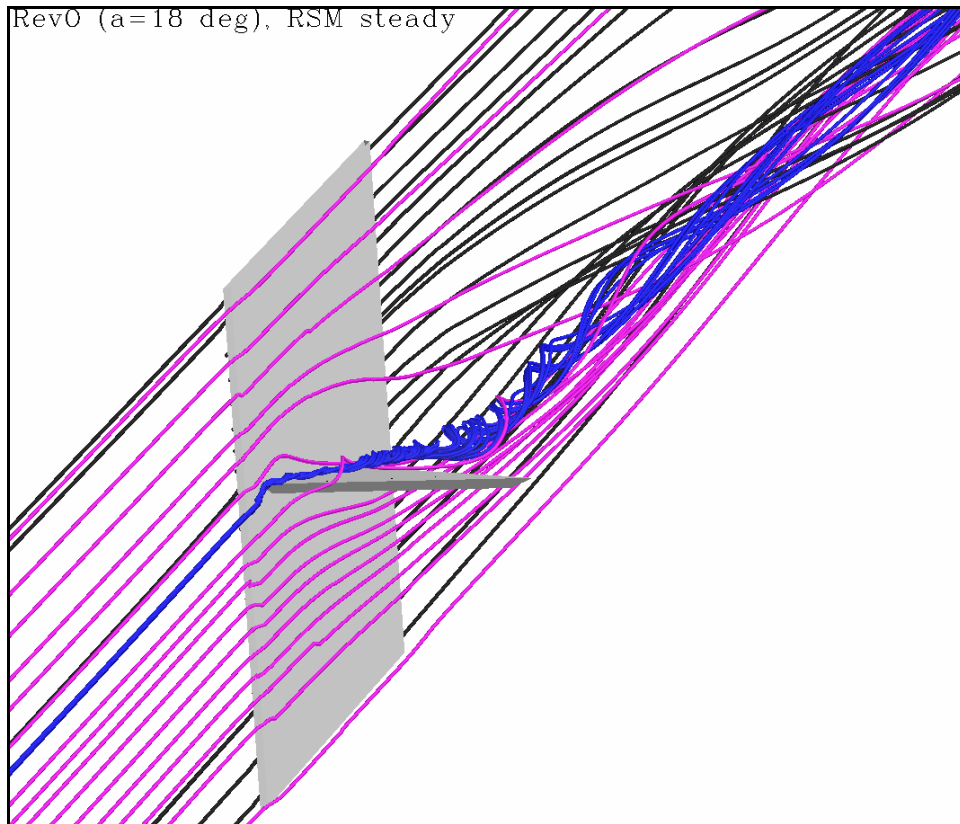


Figure 3.40 – Streamlines Showing Benign Effect of Refresher Plate Offset from Wall

In summary, Mesh Revision L was selected as an acceptable numerical mesh because it modeled correct tunnel geometry, it made a suitable approximation by placing the refresher plate flush against the tunnel wall, it resulted in accurate prediction of vortex core position, and its predicted C_P and C_L values (with modified wing angle of attack) were within a reasonable range of experimentally determined values.

Effect of Turbulence Model with Time Averaged Flow

While time averaged or steady flow solutions may not accurately predict all the physics of this highly unsteady flow, they do provide cursory correlation with the experimental data, where each C_P point on the plots below represents the average of 500 collected data points at each respective pressure sensor. Thus time averaged, numerically predicted C_P data allow for the most correct correlation between results, whereas time accurate solutions show snapshots in time and not an averaged value.

Figures 3.41-44 show experimental C_P data compared with predicted values using inviscid and laminar (non-turbulence) models, and S-A, RNG k- ϵ , and RSM turbulence models. None of the numerical models showed good agreement with the experiment, but the steady S-A model came closest to predicting a correct solution, with respect to C_P correlation. It accurately predicted the vortex core centerline location at all chordwise positions, and it came closest to slope and peak magnitude at $x/c = 0.55$ and 0.75 , which are both aft of the vortex bursting location – a region where accurate prediction is crucial. At $x/c = 0.95$, the S-A model best predicted the slope or region of vortex activity, and the magnitude was closer than the other turbulence models.

With some modification to help it predict the physics of vortex bursting, S-A may prove to be the best of these turbulence models. One modification (termed S-A Rotation

Correction) allows “production of turbulent viscosity to be reduced in regions of high vorticity,” and another (termed Detached Eddy Simulation) combines the computational advantages of the Reynolds-Averaged Navier-Stokes method with the accuracy of LES in computing highly separated flow fields (Morton, Forsythe, Mitchell, Hajek, 2002: 3, 5). But for this study, the S-A model proper remains inadequate since it failed to correctly predict occurrence of vortex breakdown.

At $x/c = 0.35$, all of the numerical models predicted nearly the same solution, though the laminar case best estimated C_p slope and magnitude, likely because this location most closely corresponds to laminar flow – prior to vortex breakdown. At this location, no model accurately predicted vortex strength or size, which may have been due to coarse grid resolution, shown in greater detail in the next section. The laminar model’s predicted C_p curves lost smoothness after vortex breakdown occurred, seen in Figures 3.42-44, indicating that a laminar model unsurprisingly has difficulty predicting properties of highly turbulent flow. The inviscid solution coincided relatively closely with laminar predictions, but since the flow field was highly dependent upon freestream conditions over the wing and since those conditions included no boundary layer flow, the inviscid prediction is not a valid option for further investigation. It was included merely for pedagogical rigor.

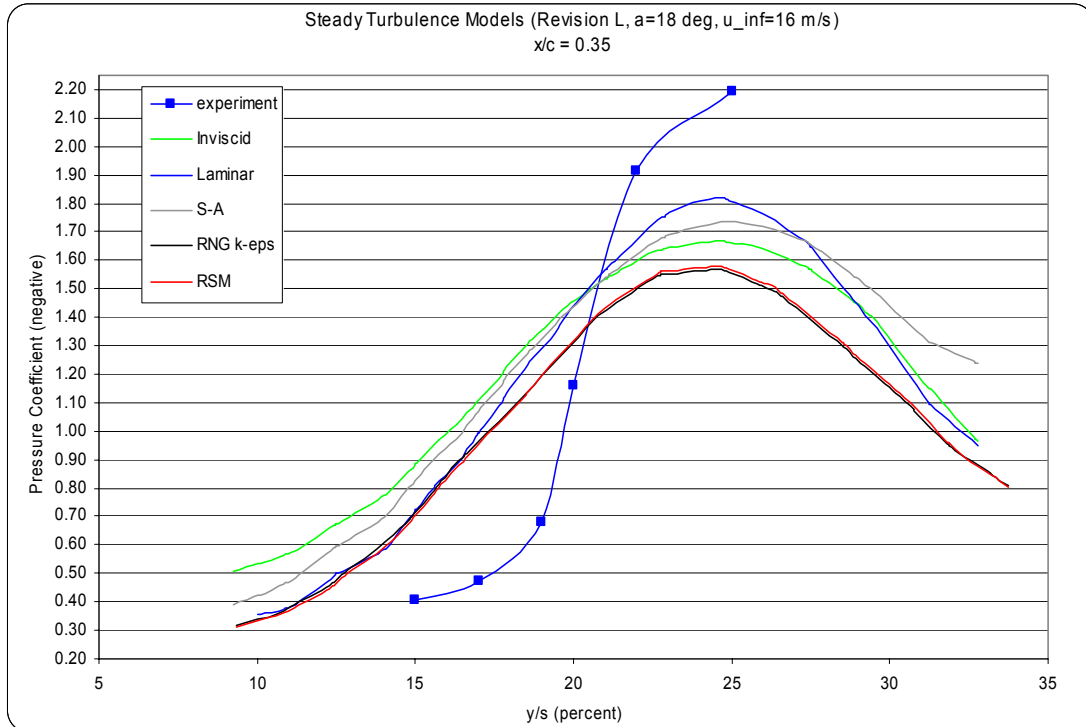


Figure 3.41 – C_p Comparison of Steady Turbulence Models at $x/c = 0.35$
(Mesh Revision L, $\alpha = 18^\circ$, $V_\infty = 16$ m/s)

There was no significant variation between k- ϵ and RSM model solutions, except in prediction of vortex center location at $x/c = 0.75$ and 0.95 . The k- ϵ model better predicted that location for $x/c = 0.75$, and RSM model better predicted it for $x/c = 0.95$. This was likely a result of applying averaging and steady modeling to an inherently unsteady flow, and there is no reason to believe that even the experimental data show a “true” vortex core position since breakdown has been observed to shift its location (Morton, Forsythe, Mitchell, Hajek, 2002; Novak, Sarpkaya, 1999; Leibovich, 1978; Faler, Leibovich, 1977).

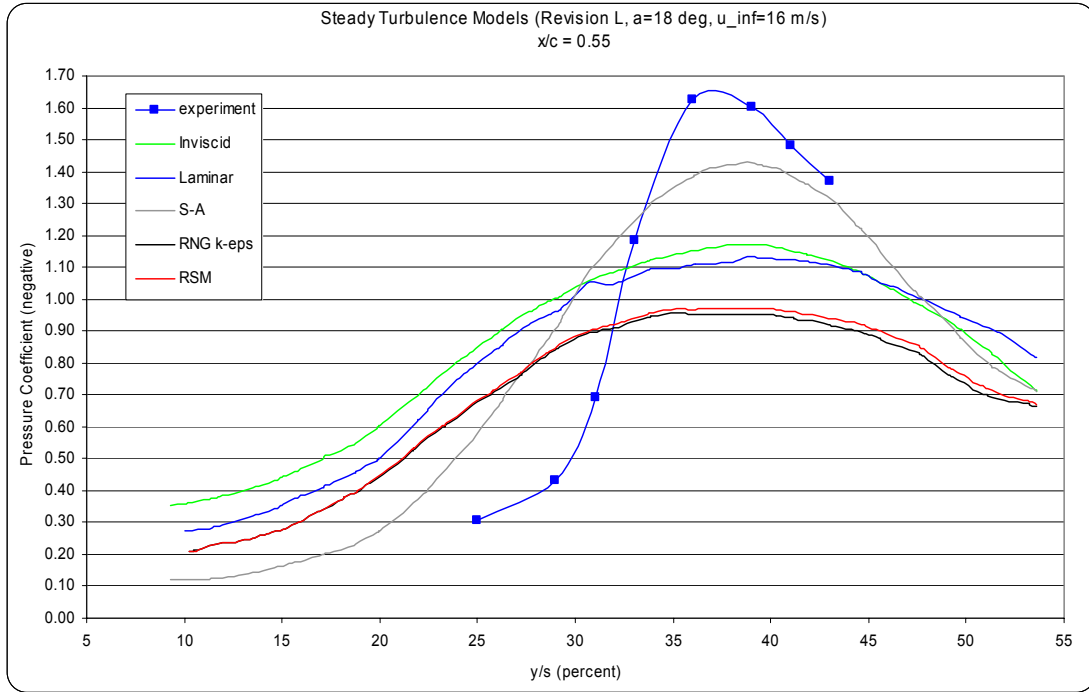


Figure 3.42 – C_p Comparison of Steady Turbulence Models at $x/c = 0.55$
(Mesh Revision L, $\alpha = 18^\circ$, $V_\infty = 16$ m/s)

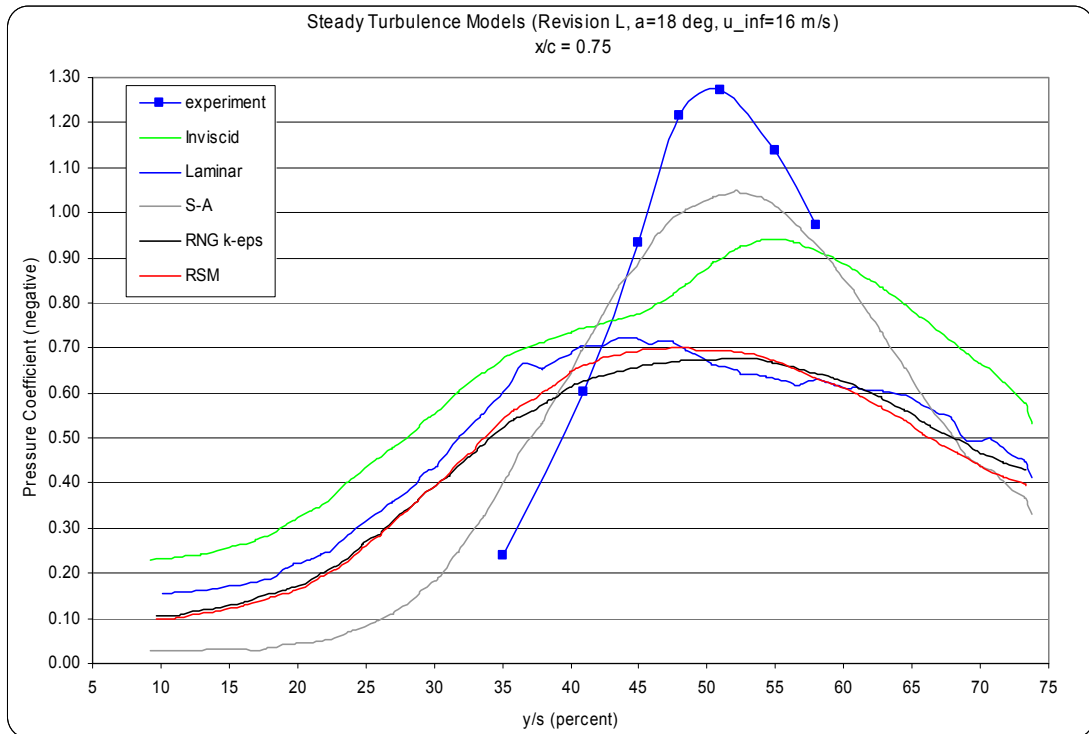


Figure 3.43 – C_p Comparison of Steady Turbulence Models at $x/c = 0.75$
(Mesh Revision L, $\alpha = 18^\circ$, $V_\infty = 16$ m/s)

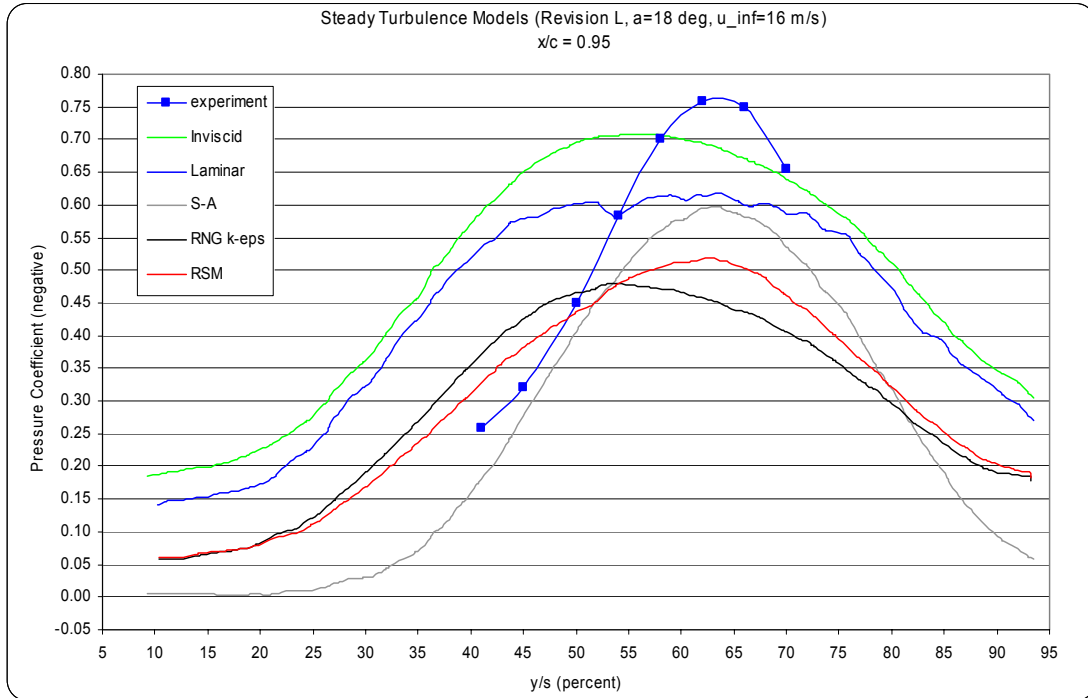


Figure 3.44 – C_p Comparison of Steady Turbulence Models at $x/c = 0.95$
(Mesh Revision L, $\alpha = 18^\circ$, $V_\infty = 16$ m/s)

Figure 3.45 shows nondimensional velocity contours, defined as V/V_∞ , contained in the plane perpendicular to the wing surface and which runs through the center of the delta wing's vortex. Its images include the predicted solution from the steady laminar, S-A, RNG k- ϵ , and RSM flow models. In the figure, predicted vortex breakdown is indicated where the vortex diameter expands and where flow may reverse and stagnate, shown by regions of dark blue, where flow is at or near zero. All but the S-A model predicted stagnated flow. However, experimentalists have observed in cases where $Re > 3 \times 10^5$ (which applies to this case where $Re = 3.4 \times 10^5$) that in the region of vortex breakdown and immediately following, the flow does not necessarily reverse, stagnate or bridge between laminar and turbulent states (Novak, Sarpkaya, 1999: 825, 833). Thus the S-A model may arguably have predicted vortex breakdown but not as pronounced as by the other models. Additionally, since reversed flow results in bubble type breakdown,

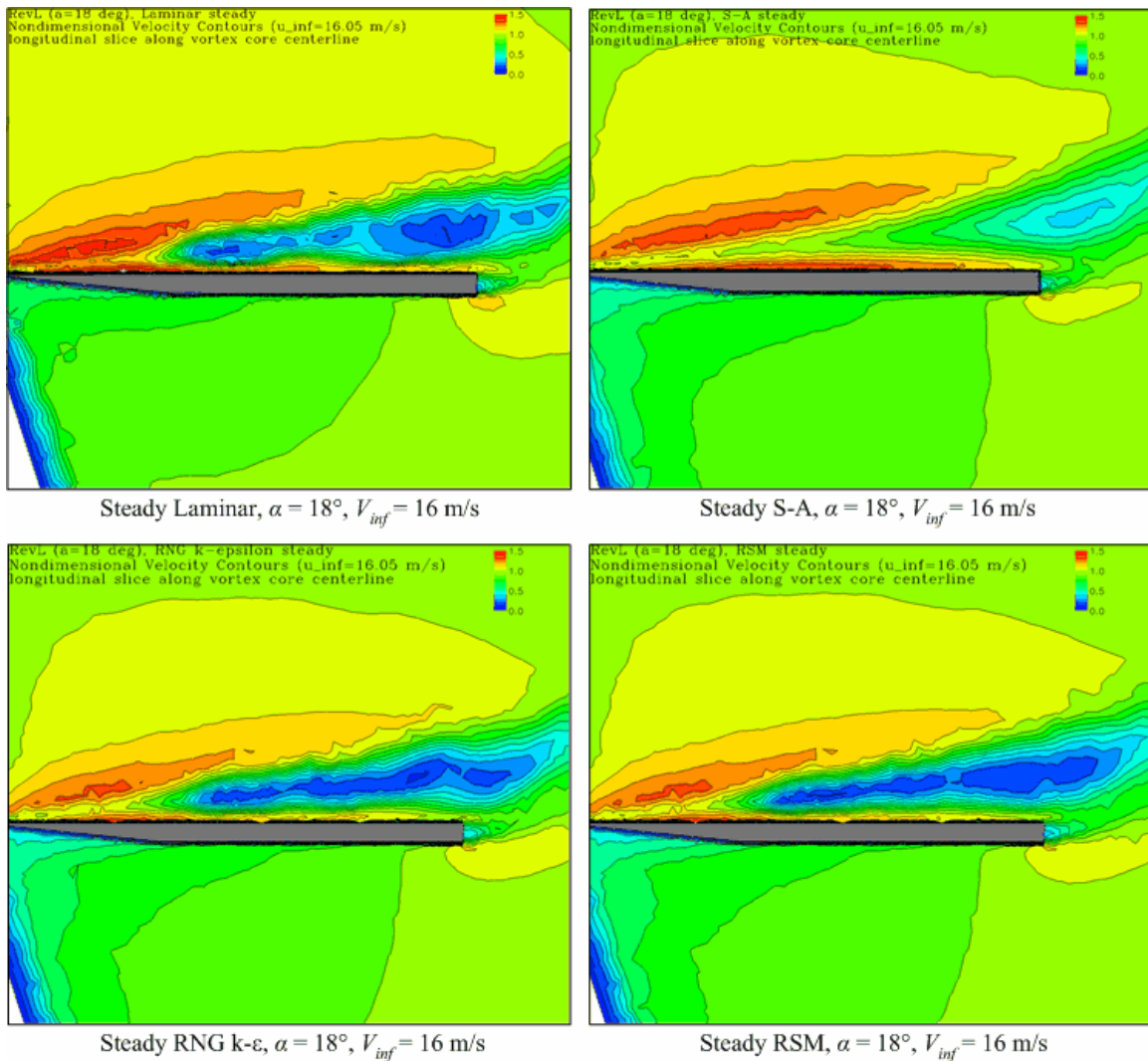


Figure 3.45 – Nondimensional Velocity Contours through Vortex Center, Predicted by Steady Turbulence Models (Mesh Revision L, $\alpha = 18^\circ$, $V_\infty = 16$ m/s)

shown in Figures 1.3a and 1.4, the vortex core diameter naturally becomes large – as predicted by the laminar, k- ϵ and RSM models, and as indicated in Figures 3.41-45 where these models predicted a larger region of vortex bursting and turbulence. But since experimental findings indicate that flow at this Reynolds number typically results in spiral type breakdown with smaller vortex diameter, the S-A turbulence model most accurately predicted a solution which correlates with experimental numerical data and with experimental observation of the flow physics, at least with respect to vortex size

after bursting. This conclusion must include the caveat that the steady S-A model's predicted solution was only marginally acceptable, since C_P magnitudes were low by as much as 21% from the experimental value and since predicted vortex diameter at $x/c = 0.35$ and 0.55 was larger than indicated experimentally – shown by lesser C_P curve slope in Figures 3.41 and 3.42. Furthermore, the LSU study, which used the same wing but attached a fuselage, showed distinct and relatively large regions of stagnated flow as the vortex approached the wing's trailing edge (Guillot, 1999: 41). To summarize, the S-A model may become the most accurate turbulence model after appropriate numerical code modifications are incorporated to help it better predict the physics of vortex breakdown (Morton, Forsythe, Mitchell, Hajek, 2002).

Another observation from the S-A model's predicted solution in Figure 3.45 is that the vortex rotational speed prior to breakdown was approximately 2,200 rad/sec or 350 Hz, based on radial velocity and distance from vortex center. This result is less than it should be because the radial distance was over-predicted and is considerably less than an experimental observation of 1,000 Hz for a similar configuration and of 860 Hz for the LSU study (estimated graphically, not measured specifically) and serves as further evidence that the numerical model is not entirely accurate (Novak, Sarpkaya, 1999: 825; Guillot, 1999: 41).

Figure 3.46 shows blue particle streamlines through the vortex and bursting region and a red vortex core centerline for the same turbulence models shown in Figure 3.45. The vortex core centerline was created using FIELDVIEW's Vorticity Alignment method, and vortex breakdown follows shortly after the first large break in that line (Intelligent Light, 2001: 137). The streamlines indicate roughly where vortex breakdown

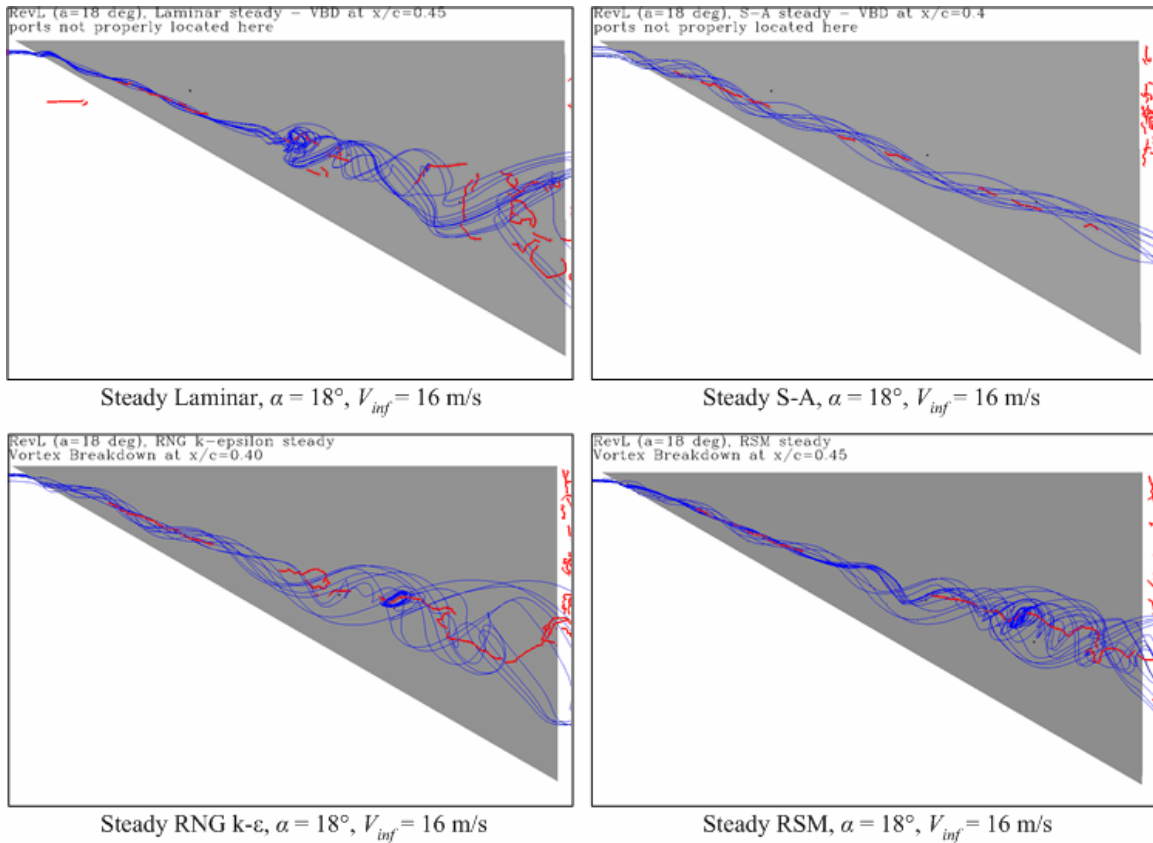


Figure 3.46 – Blue Streamlines through Vortex and Red Vortex Core, Predicted by Steady Turbulence Models (Mesh Revision L, $\alpha = 18^\circ$, $V_\infty = 16$ m/s)

occurs, shown by radial expansion, and they show reversed flow in the laminar, k- ϵ and RSM cases. In the S-A case, top right in Figure 3.46, vortex bursting is indicated by the first large break in the vortex core centerline; the streamlines relax in frequency rather than expand significantly in core diameter. It is debatable whether the S-A model even predicted vortex breakdown.

From Figures 3.45 and 3.46, the approximate location may be identified where vortex breakdown occurs. It is seen in Figure 3.45 where there begins to be velocity gradients inside the vortex core and in Figure 3.46 where streamlines show relaxed rotational frequency or vortex diameter expansion and where a large break occurs in the vortex core centerline prediction. With each turbulence model, the solution appears to

predict a vortex breakdown location between $x/c = 0.35$ and 0.45 . A more precise location would be arguable, since it is a subjective determination.

These results agree relatively closely with three experimental studies. Two of those studies used a delta wing with the same aspect ratio and sweep angle, a slightly greater thickness, and $Re = 1.0 \times 10^5$, and those studies for $\alpha = 18^\circ$ each determined vortex breakdown occurred between $x/c = 0.42$ and 0.45 (Johari, Olinger, Fitzpatrick, 1995: 806; O'Neil et al, 1989). The third study (LSU) used the same half delta wing as this study but with fuselage attached; in that configuration with $\alpha = 15^\circ$, one may argue the equivalent angle of attack was about 18° , since there is close C_L agreement seen in Table 3.2 (using results from the steady S-A model at $\alpha = 18^\circ$). The LSU study determined that vortex breakdown occurred between $x/c = 0.3$ and 0.4 (Guillot, 1999: 38). Traub's method predicts vortex breakdown occurs at $x/c = 0.23$ for $\alpha = 18^\circ$ and at $x/c = 0.43$ for $\alpha = 15^\circ$, based on empirical data for delta wings with larger sweep angles than that used in this study (1996; see Appendix B for calculations). An earlier study showed breakdown at about $x/c = 0.6$ for $\alpha = 18^\circ$, but that experiment used a delta wing with a thickness of 0.25 cm (about 20% the thickness used in this study), sharper leading edge bevel and a rough upper wing surface (Wentz, Kohlman, 1971).

Figure 3.47 shows contour slices of total pressure over the wing surface from the steady laminar model's predicted solution. The slices are perpendicular to the upper wing surface, spaced from $x/c = 0.05$ to 1.05 by increments $0.10c$. In this figure, vortex breakdown occurred where the inner core pressure contours first expand, which was possibly as soon as between $x/c = 0.25$ and 0.35 but more likely between $x/c = 0.35$ and 0.45 . This is a visually qualitative assessment but has potential to feed into a quantitative

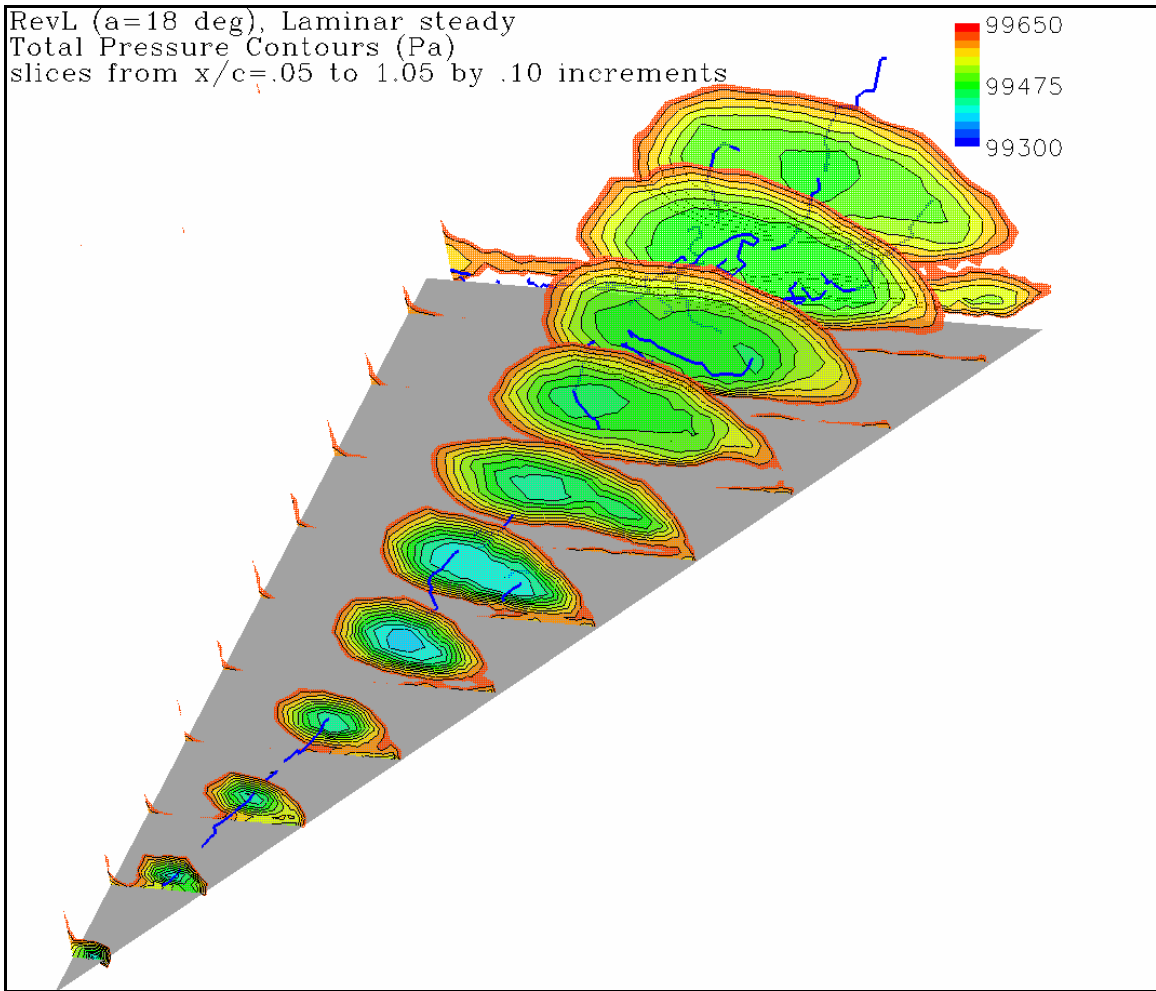


Figure 3.47 – Contours of Total Pressure over Wing Surface for Steady, Laminar Model (Mesh Revision L, $\alpha = 18^\circ$, $V_\infty = 16$ m/s)

feedback control system, should the system need to identify where vortex breakdown occurs. This steady laminar model resulted in over-prediction of vortex extent but it adequately demonstrates the physics of vortex bursting.

Figure 3.48 shows contour slices of velocity magnitude nondimensionalized by the freestream velocity over the wing surface from the steady, S-A turbulence model's predicted solution at the same locations described for Figure 3.47. Contours were limited between $V/V_\infty = 1.0$ and 1.6 for easier visibility of multiple slices, and a dark blue line indicates the vortex core centerline by vorticity alignment. This contour plot was

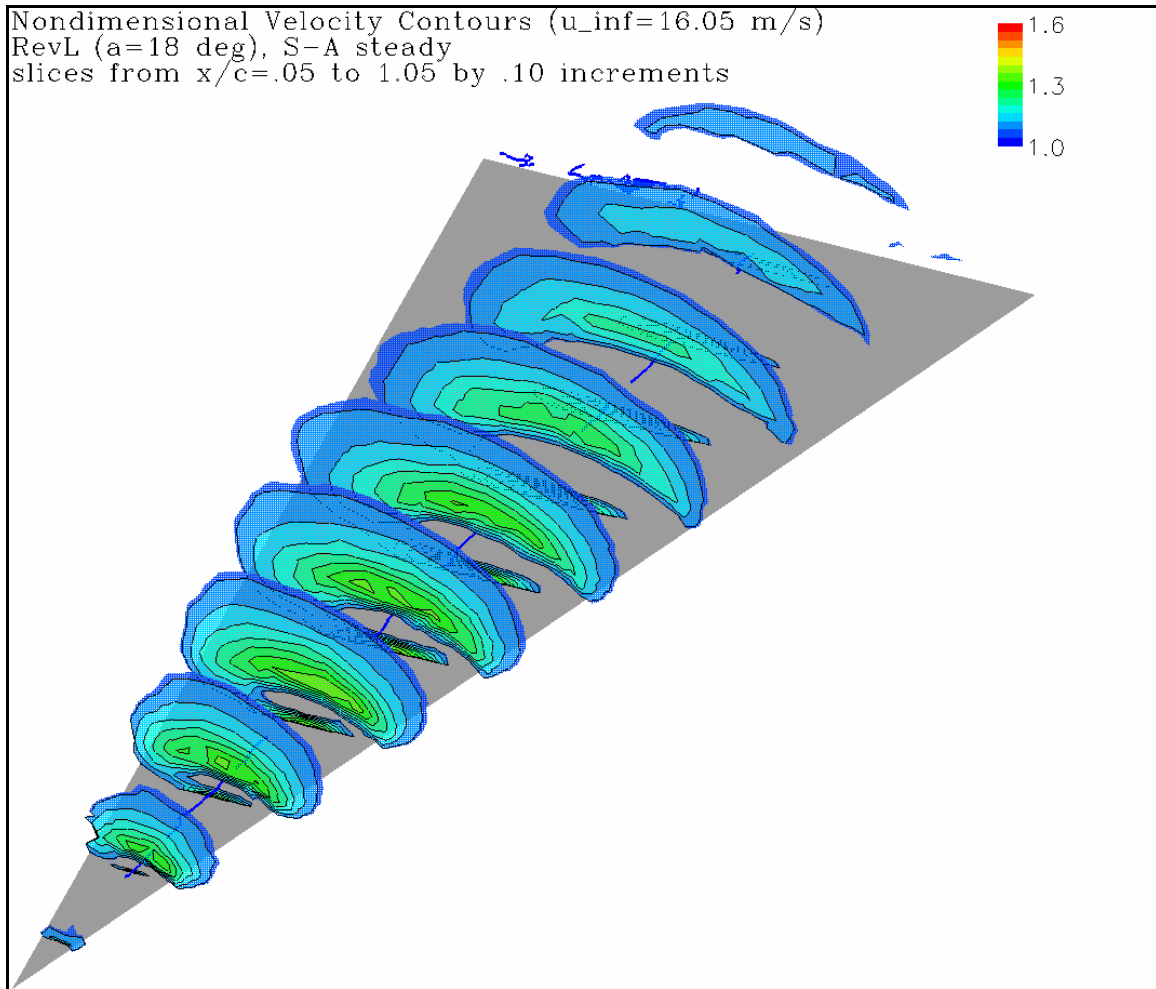


Figure 3.48 – Contours of Nondimensional Velocity over Wing Surface for Steady, S-A Turbulence Model (Mesh Revision L, $\alpha = 18^\circ$, $V_\infty = 16$ m/s)

included for comparison with equivalent plots of data generated in the LSU experiments, and these contours compare reasonably well with those experimental results. Forms are basically the same but the numerically predicted magnitudes are lower by roughly 10% in the areas of maximum velocity. Interestingly the LSU data indicated no regions of stagnated axial flow until $x/c = 0.75$ (Guillot, 1999: 41). This indicates that the steady S-A model is perhaps the least inaccurate of the turbulence models evaluated in this study, since the other models (laminar, k- ϵ and RSM) predicted stagnation as early as $x/c =$

0.50; however, the S-A model is far from accurate, since it did not predict any stagnation whatever and since it questionably even predicted vortex breakdown.

As one additional argument against the steady S-A model's ability to correctly predict vortex breakdown, Figure 3.49 compares iso-surface helicity contours for the steady S-A and laminar models. Helicity is the dot product of vorticity, which is a measure of rotational fluid flow, and the velocity vector (FLUENT, 2001: 27.4). This figure shows that the laminar model predicts breakdown of this relatively uniform rotational flow much sooner chordwise than it does with the S-A model. Interestingly, neither model predicted breakdown of the secondary vortex along the leading edge, which is contrary to experimental findings that the secondary vortex's breakdown preceded that of the primary vortex (Cummings, Morton, Siegel, 2003).

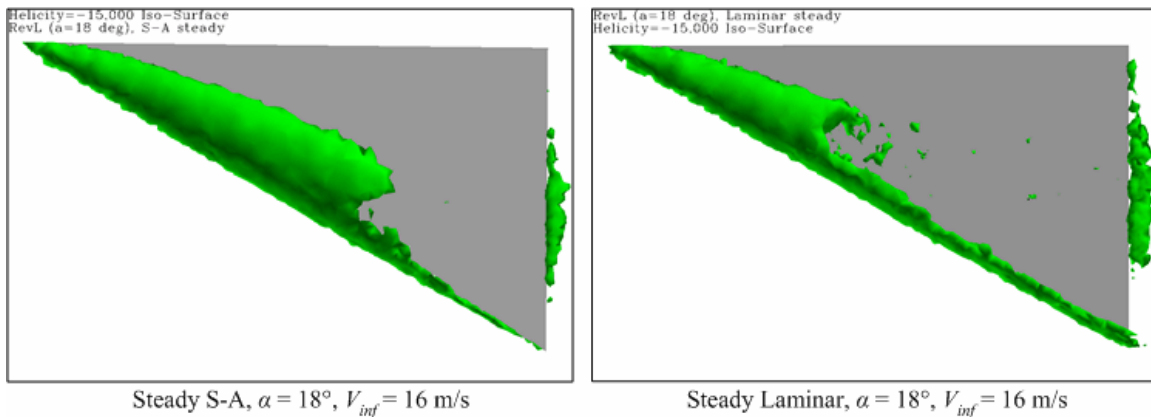


Figure 3.49 – Iso-Surface Helicity Contours for Steady S-A and Laminar Models
(Mesh Revision L, $\alpha = 18^\circ$, $V_\infty = 16$ m/s)

To summarize the steady solutions from the various non-turbulence and turbulence models, the inviscid, laminar, RNG k- ϵ , and RSM models over-predicted the expanse of vortex breakdown and its ensuing turbulence and under-predicted vortex strength, indicated by lower velocity and higher static pressure around the primary vortex. The steady S-A turbulence model also under-predicted vortex strength, though

generally not as poorly as the other models; except at $x/c = 0.35$ (which may be a grid resolution issue), it predicted satisfactorily the region and extents of vortex breakdown and its turbulent wake. Thus none of the steady turbulence models predicted a completely satisfactory solution.

Since “the effect of grid density or flow solver may have a higher-order effect on the solution than the turbulence model itself” (Kral, 1998: 485), a study of grid resolution follows.

Mesh Adaptation

As part of a mesh independence study and in hopes of improving the numerically predicted solutions, Mesh Revision L was adapted in two ways using the *Mesh Adaptation* features in FLUENT, and it was modified also in Gridgen to form Revision N. The first adaptation was motivated from a numerical study analyzing delta wing vortex generation with an unstructured grid, which concluded that topological features may be effectively used for mesh refinement to obtain better vortex resolution and stated that “grid resolution around the vortex core is very important for the accurate prediction of the vortex breakdown” (Murayama, Nakahashi, Sawada, 2001: 1305, 1311). Also, it is necessary to use “sufficient grid resolution in regions of high flow gradients [such as around and within the vortex core] to obtain accurate numerical solutions” (Ekaterinaris, Schiff, 1990: 60). In accordance with these recommendations, a FLUENT *Iso-Value Adaption* was performed on the steady S-A solution from Mesh Revision L with $\alpha = 18^\circ$ and $V_\infty = 16$ m/s. This adaptation was focused on iso-metric contours of turbulent viscosity, since these contours captured the turbulent field within the vortex core; all cells with turbulent viscosity values between 0.0019 and 0.0020 m^2/s were then refined.

FLUENT refines three-dimensional cells by dividing each respective face into four equal triangles or squares then propagating it volumetrically (FLUENT, 2001: 23.2.2). The result of this refinement is shown in Figure 3.50, where the image on top shows a vertical

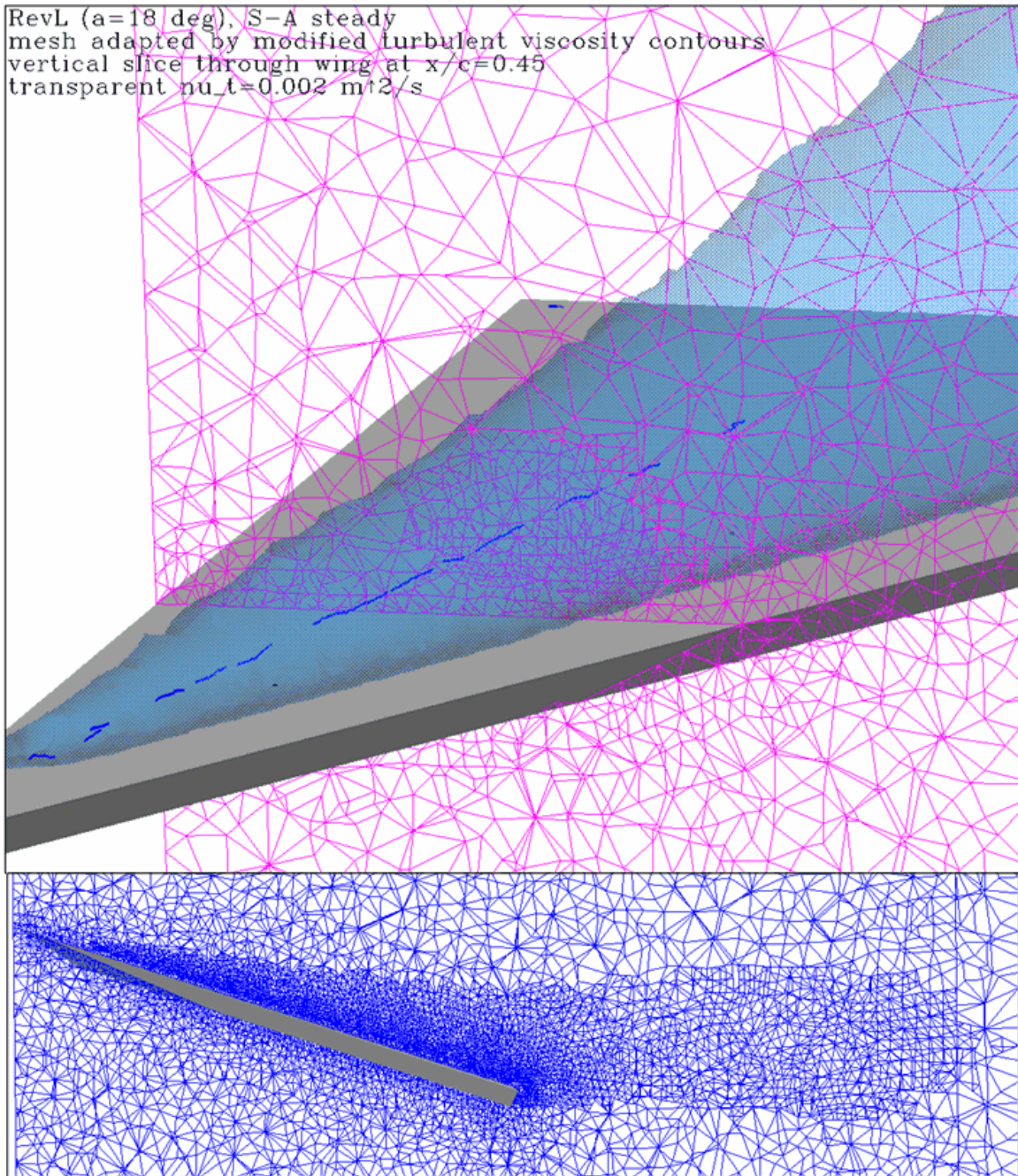


Figure 3.50 – Mesh Adaptation within Vortex Core
(Revision L, Steady S-A, $\alpha = 18^\circ$, $V_\infty = 16$ m/s)

slice through the turbulent viscosity three-dimensional field and the image on the bottom shows the extent of the adaptation via a slice through the vortex core. This adaptation created an additional 327,000 tetrahedral cells for a 56% increase in total number of volumetric cells.

Another adaptation, independent of the adaptation described above, was performed to better show generation of the secondary vortex along the wing's leading edge and incidentally improved portions of the solution prediction. This adaptation used FLUENT's *Region Adaption* menu option and created a cylindrical region for refinement. The cylinder's centerline was located parallel to, 1 cm above and 1 cm inboard of the wing leading edge; cylinder radius was 2.5 cm. This allowed for refined cells along both lower and upper surfaces of the wing around the leading edge. This improved resolution in the region of the secondary vortex but also in the region where the primary vortex is initialized (or where the shear layers separate), resulting in a generally improved predicted solution. This refinement is shown in Figure 3.51 as a tight clustering of cells on the wing surface (bottom image) and in a vertical slice around the wing (top image). An additional 295,000 tetrahedral cells resulted from this adaptation.

Mesh Revision N was created in an effort to refine the number of cells around the entire wing upper surface but not to the degree generated by FLUENT. A three-dimensional permeable enclosure was created with roughly a 2.5-cm gap between it and the wing, excluding the wing's bottom surface; it resembles a box for a slice of pie or pizza, as shown in the top image in Figure 3.52. The bottom image shows the cell face resolution and nodal dimensions on the upper wing surface, which dimensions are double those of Revision L's upper wing surface. These changes resulted in an additional

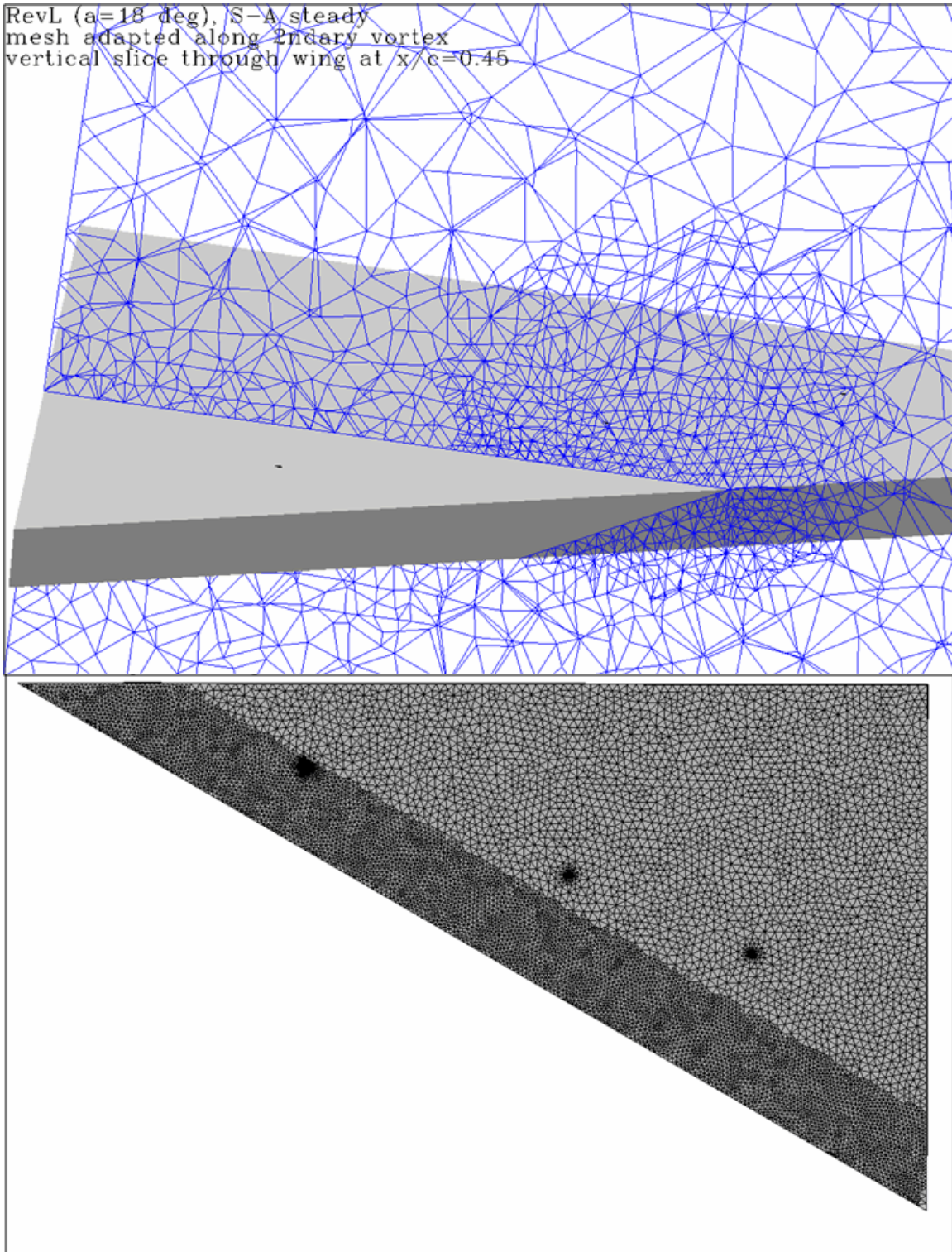
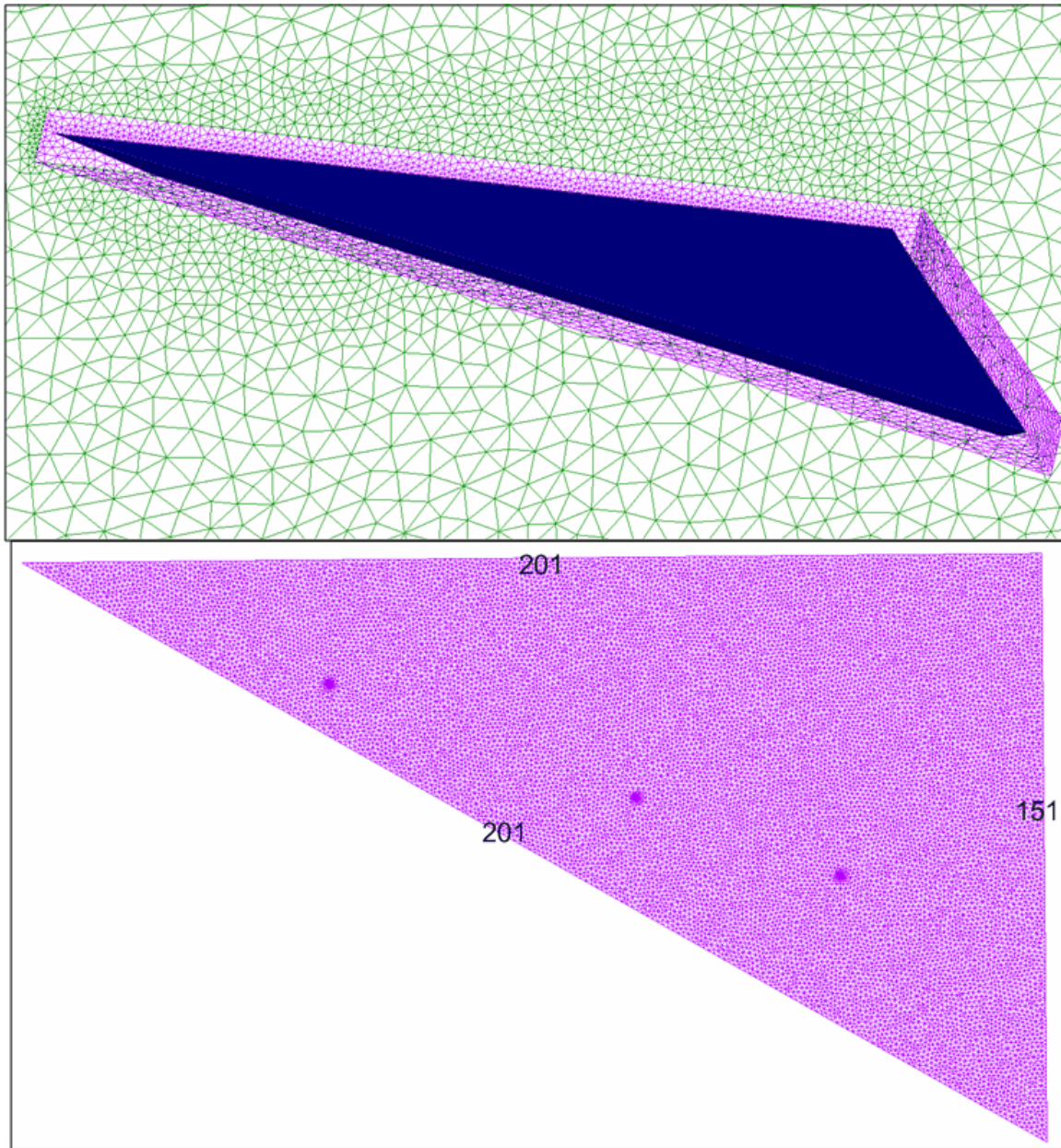


Figure 3.51 – Mesh Adaptation along Leading Edge
(Revision L, Steady S-A, $\alpha = 18^\circ$, $V_\infty = 16$ m/s)



Adapted over Upper Surface, Mesh Revision N

Adapted over Upper Surface, Mesh Revision N

Figure 3.52 – Mesh Adaptation: Revision N (Steady S-A, $\alpha = 18^\circ$, $V_\infty = 16$ m/s)

215,000 tetrahedral cells and gave results comparable to those from the leading-edge adaptation but at less computational cost. All of the adaptations lowered y^+ values along the wing surface but still not sufficiently to meet the resolution requirement for the LES model.

Each adaptation was used to generate a numerical solution using S-A turbulence model and steady solver with $\alpha = 18^\circ$ and $V_\infty = 16$ m/s. Table 3.3 summarizes computed lift coefficients, and additional comparisons follow. Solutions from the adapted meshes resulted in no more than 0.6% variation from the non-adapted baseline's C_L , thus showing that the initial numerical mesh allowed for adequate prediction of this integrated quantity.

Table 3.3 – Comparison of C_L Resulting from Various Mesh Adaptations and Using Steady S-A Model with $\alpha = 18^\circ$ and $V_\infty = 16$ m/s

Case	C_L
Rev L, No Adaptation	0.7974
Rev L, Turbulent Viscosity Adaptation	0.8022
Rev L, Leading Edge Region Adaptation	0.7978
Rev N, Pie Slice Box Adaptation	0.7959

The right-side image in Figure 3.53 shows noticeable improvement in contour smoothness for the model with refined mesh within the vortex core. Smoother contours for this adapted mesh are also visible in the top right image in Figure 3.55. In addition to finer resolution, this mesh adaptation resulted in improved C_p slopes and magnitudes in

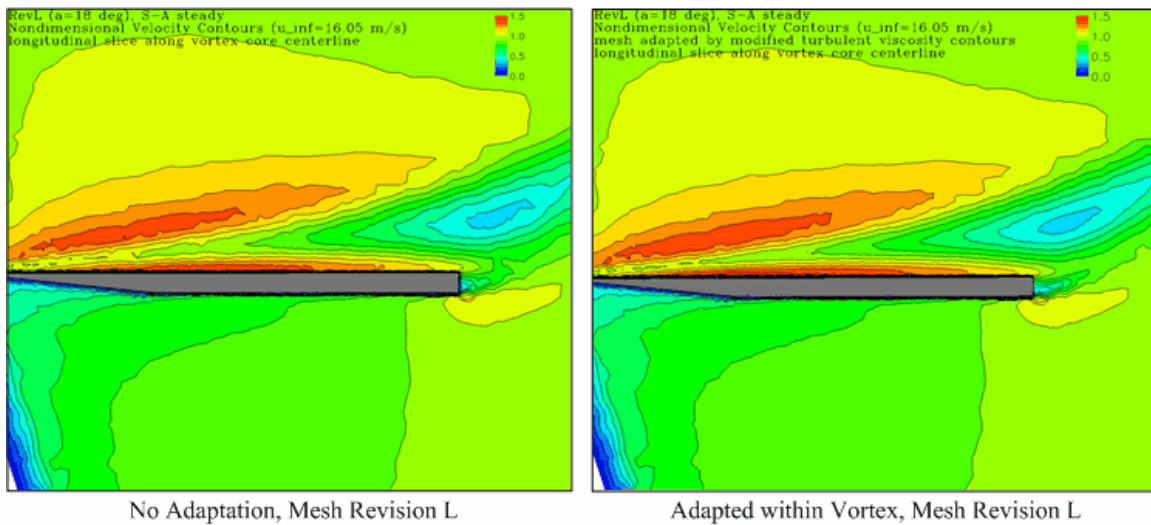


Figure 3.53 – Nondimensional Velocity within Vortex Core for Revision L and Adaptation by Turbulent Viscosity Iso-Contours (Steady S-A, $\alpha = 18^\circ$, $V_\infty = 16$ m/s)

Figures 3.56-59; its prediction (blue line with no markers) exceed the non-adapted solution (green line) by 4-6%. However, these improvements were small and were not deemed worthwhile for the tradeoff in computational speed.

Figure 3.54 compares plots of no-slip surface-restricted flow (sometimes termed oil surface flow) predicted by the steady S-A models with mesh adaptation along the leading edge (top right), over the upper wing surface (bottom), and with the non-adapted mesh (top left). In addition to providing greater resolution of the surface flow lines, both adapted mesh solutions better indicate presence of a secondary vortex, along the leading edge. Surface-restricted flow plots showed little variation among solutions from different

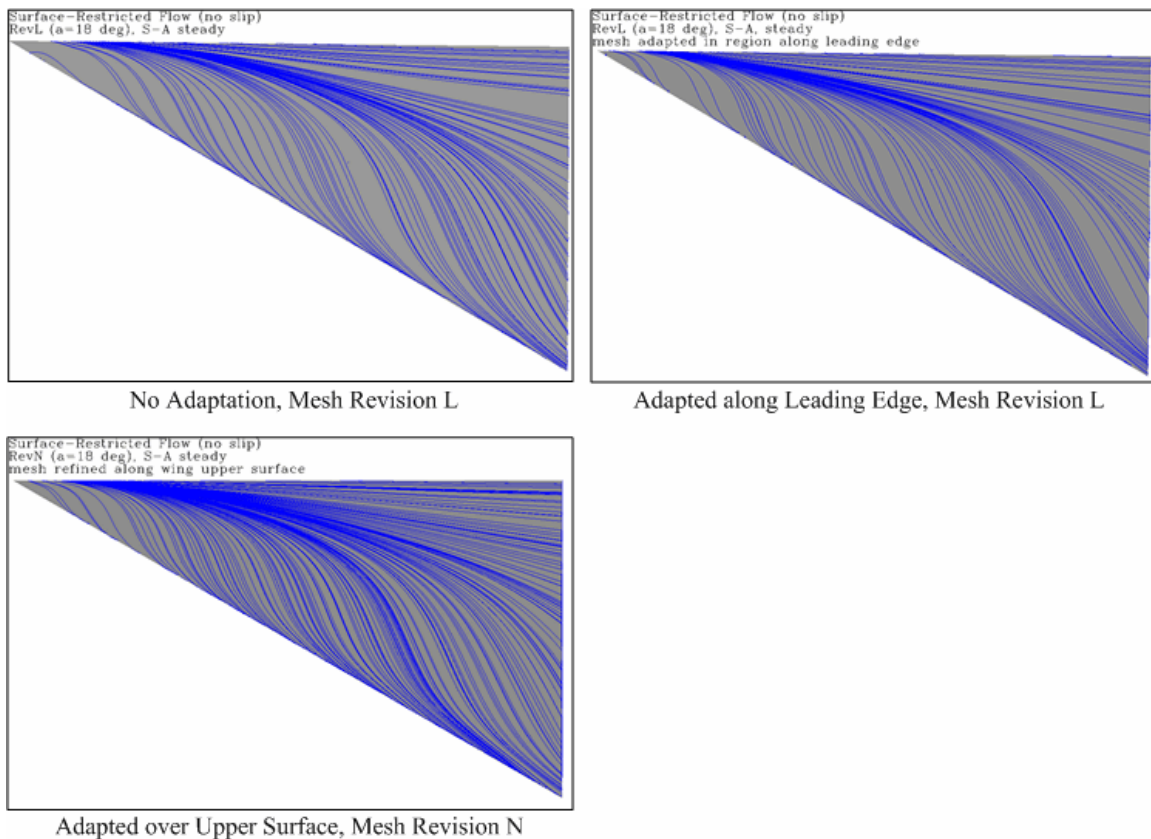


Figure 3.54 – Wing Surface-Restricted Flow for Mesh Revision L, Adaptation along Leading Edge, and Revision N (Steady S-A, $\alpha = 18^\circ$, $V_\infty = 16$ m/s)

turbulence models, as well as between steady and unsteady solutions; thus no additional oil flow plots are included in this document.

Improved secondary vortex resolution becomes more apparent after observing total pressure contours in Figure 3.55. In that figure's images from the adapted mesh solutions (bottom left and right), for adaptation along the leading edge and over the upper surface, the secondary vortex along the leading edge has greater strength and is better distinguished from the primary vortex. It appears further that the leading edge mesh

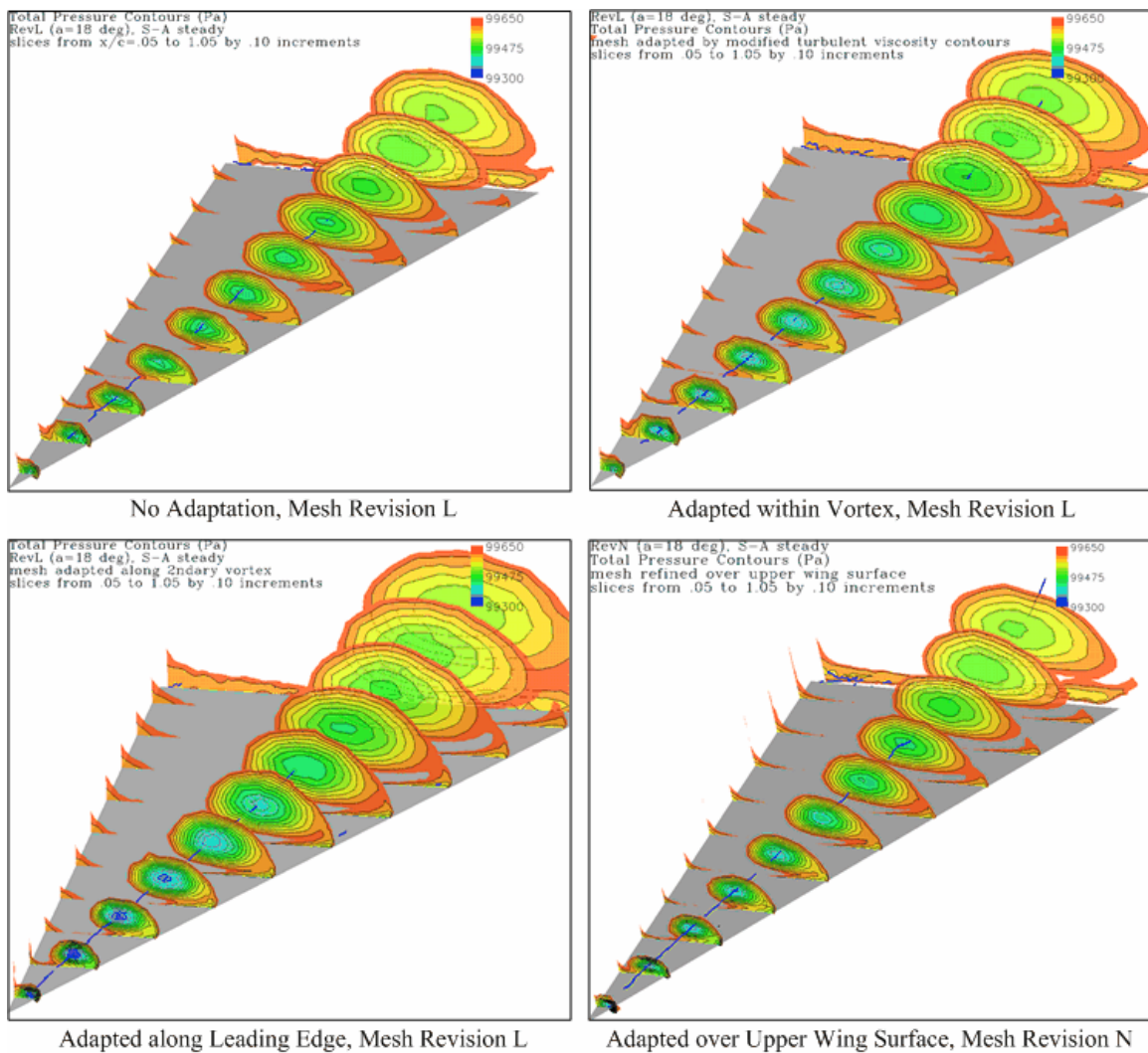


Figure 3.55 – Contours of Total Pressure over Wing Surface for Mesh Revision L, Adaptations, and Revision N (Steady S-A, $\alpha = 18^\circ$, $V_\infty = 16$ m/s)

refinement gave better resolution than did Mesh Revision N, indicated also in Figure 3.56, where a small secondary C_P peak is evident around $y/s = 0.34$; but again it is an issue of computational load, where Revision N iterated and converged more quickly.

Apparently, mesh adaptation using turbulent viscosity contours failed to refine the vortex core in its entirety, as the other adaptations appear to have better refined the vortex core centerline, indicated by a thick blue line in each image in Figure 3.55. Nonetheless, each adapted case resulted in improved centerline resolution, which may assist in identification of vortex breakdown location.

Figure 3.56 shows quite clearly that mesh adaptation improved the solution at and likely around $x/c = 0.35$; this shows also that the solution from Revision L was not mesh independent at that location. Comparing against the non-adapted results, the numerical model with leading edge adaptation improved the peak C_P magnitude by 13%, and the two other adapted meshes each resulted in 5.7% magnitude increase. They also slightly improved the C_P curves' slopes or vortex extents. However, Figures 3.57-59 indicate that Revision L's solution was independent of mesh at most other locations over the wing surface. Therefore, since the regions corresponding to $x/c > 0.35$ have greater significance for vortex breakdown control issues, the non-adapted Mesh Revision L was considered sufficient for further evaluation. As an aside, the model used for follow-on investigations would do well to include improved grid resolution in the region corresponding to the forward half of the wing.

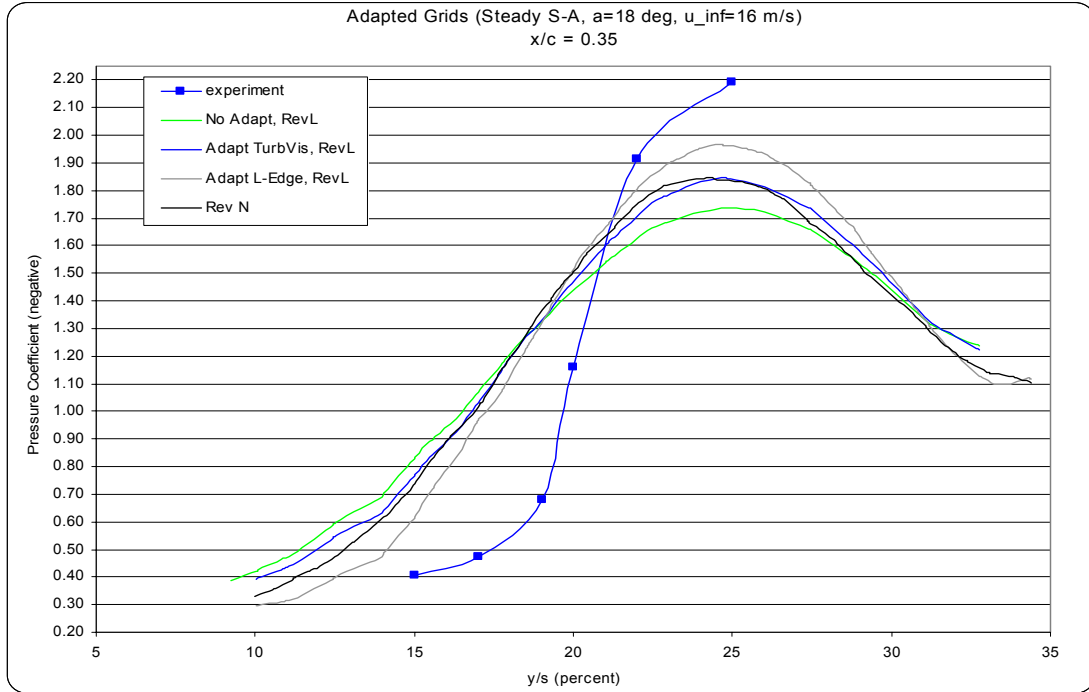


Figure 3.56 – C_p Comparison of Mesh Revision N and Adaptations of Mesh Revision L at $x/c = 0.35$ (Steady S-A, $\alpha = 18^\circ$, $V_\infty = 16$ m/s)

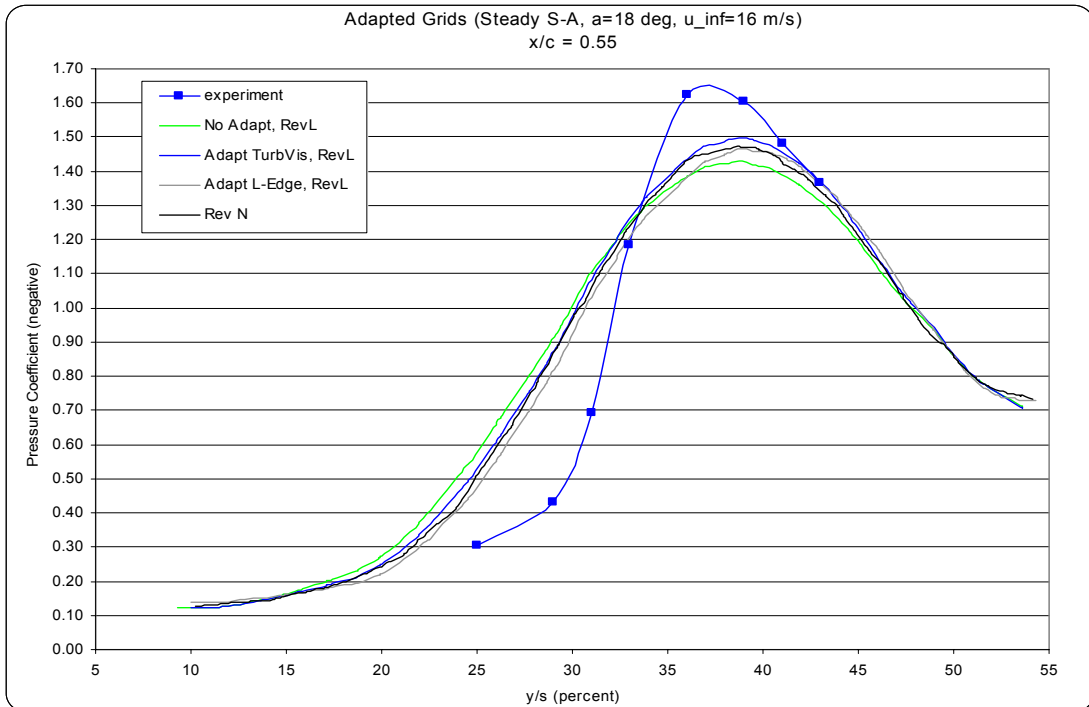


Figure 3.57 – C_p Comparison of Mesh Revision N and Adaptations of Mesh Revision L at $x/c = 0.55$ (Steady S-A, $\alpha = 18^\circ$, $V_\infty = 16$ m/s)

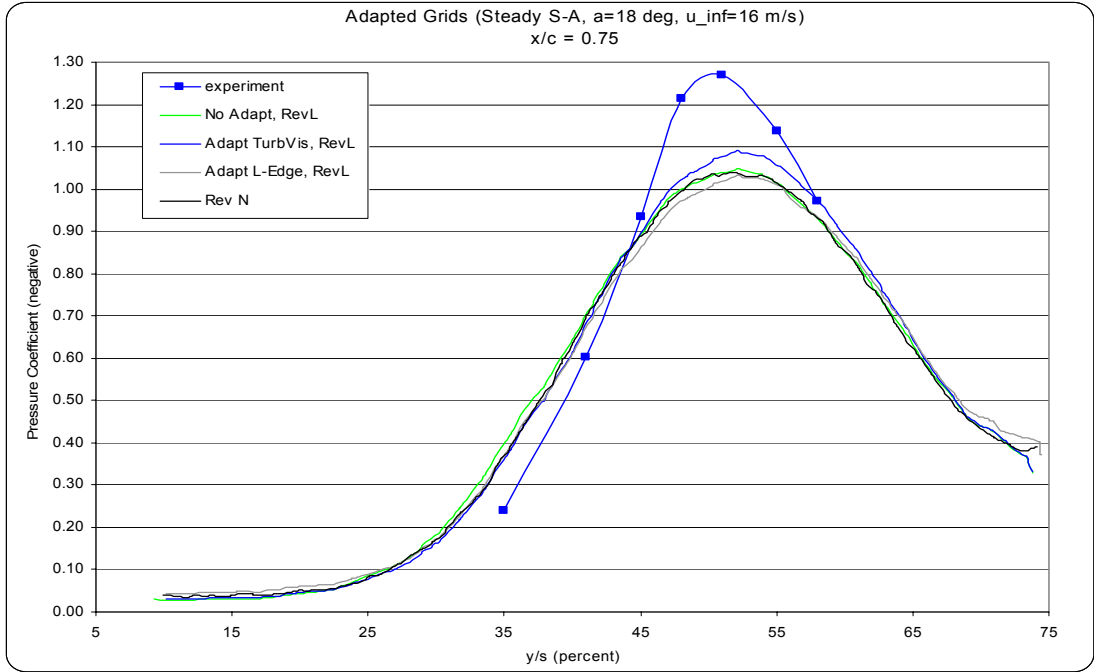


Figure 3.58 – C_p Comparison of Mesh Revision N and Adaptations of Mesh Revision L at $x/c = 0.75$ (Steady S-A, $\alpha = 18^\circ$, $V_\infty = 16$ m/s)

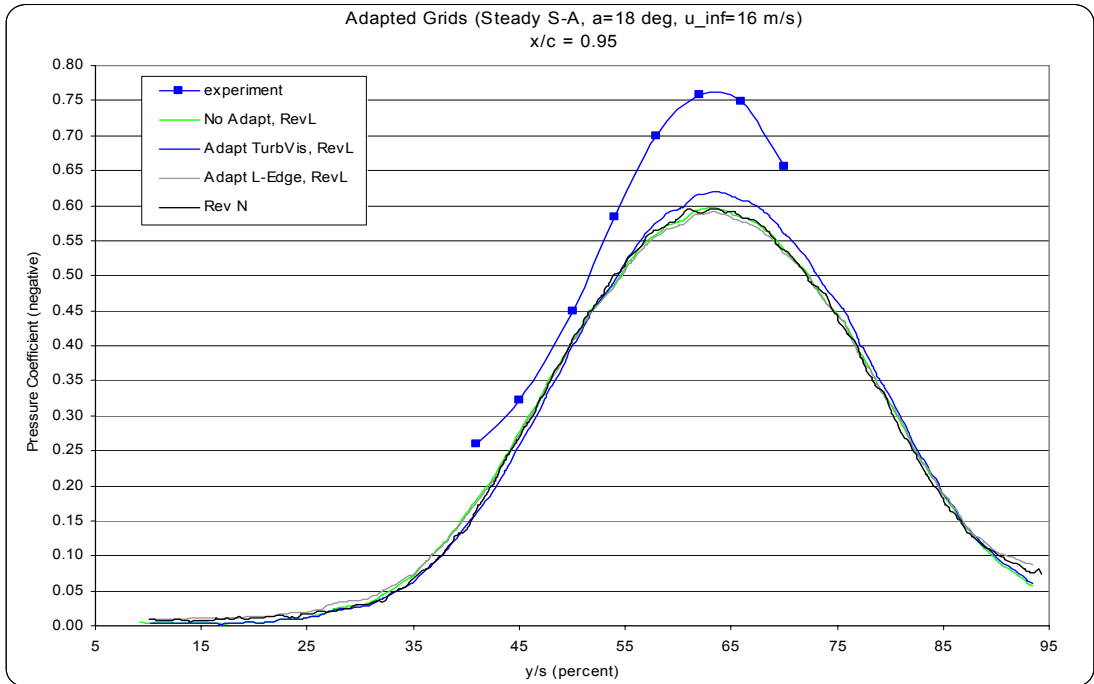


Figure 3.59 – C_p Comparison of Mesh Revision N and Adaptations of Mesh Revision L at $x/c = 0.95$ (Steady S-A, $\alpha = 18^\circ$, $V_\infty = 16$ m/s)

In retrospect, it was a poor decision to not proceed at least with Mesh Revision N, because it was later learned that the secondary vortex breakdown appears to affect and perhaps feed into the primary vortex breakdown (Cummings, Morton, Siegel, 2003). With that revelation, it would be prudent to use a model which predicts and adequately resolves the secondary vortex flow properties, as well as those of the primary vortex. Whereas in this study, improved resolution of the secondary vortex was deemed an academically interesting but non-essential exercise, and its resultant improvement in the overall solution was weighed unfavorably against the required additional computation time and resources.

Effect of Turbulence Model with Time Accurate Flow

This section discusses some pros and cons of using an unsteady and hence more accurate solver for this highly unsteady problem and comparison of the S-A, RNG k- ϵ , and RSM turbulence models using Mesh Revision L with $\alpha = 18^\circ$ and $V_\infty = 16$ m/s. Inviscid and laminar models were not evaluated in the unsteady domain due to the turbulent nature of the flow within and aft of vortex breakdown. While the LES model (unsteady by default) was used preliminarily, its results and poor correlation with experimental data confirmed the requirement for a fine numerical mesh (with $y^+ \approx 1$ along all surfaces of interest); due to limitations on time and computing resources in this study, the fine computational grid was not completed. Adapted meshes were not evaluated in time accurate flow, though that is a recommended improvement for future work.

Using an unsteady solver for this problem had certain advantages over using a steady solver. As expected it predicted flow physics which were considerably more

consistent with theoretical assertions and experimental findings. Once flow was fully developed (after roughly 2 sec in dimensional time), Figure 3.60 shows with streamlines through the vortex core, using the RSM turbulence model, that there was notable fluctuation over time in the flow structure within and following vortex breakdown – in radial extent of the core and in local flow direction within the core. A steady solver has

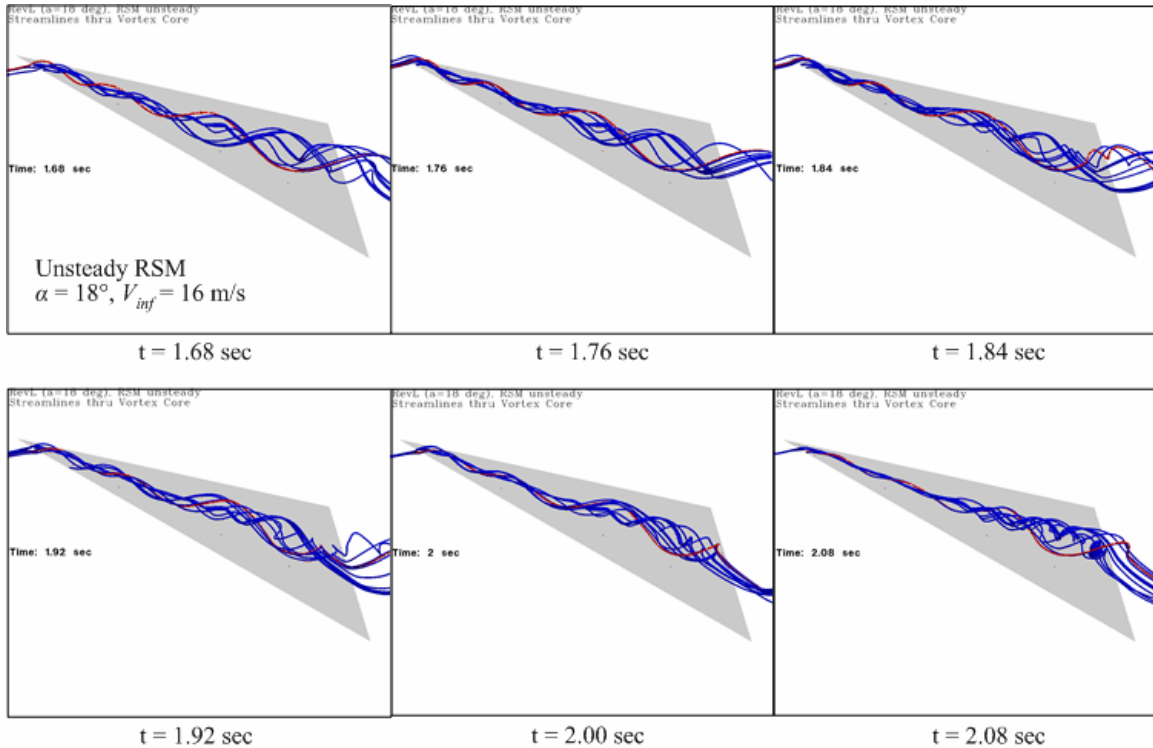


Figure 3.60 – Streamlines through Vortex from Unsteady RSM Turbulence Model (Revision L, $\alpha = 18^\circ$, $V_\infty = 16$ m/s)

not the capacity to predict temporal fluctuations in flow structure. However, Figure 3.61 shows with streamlines through the vortex core, using the k- ϵ turbulence model, that there was no fluctuation over time in the flow structure and that the unsteady solution is essentially equivalent to the time averaged solution (top left image in the figure). The S-A model yielded also a time independent vortex structure and one which failed to adequately predict vortex breakdown, just as it failed to do in steady state. Its

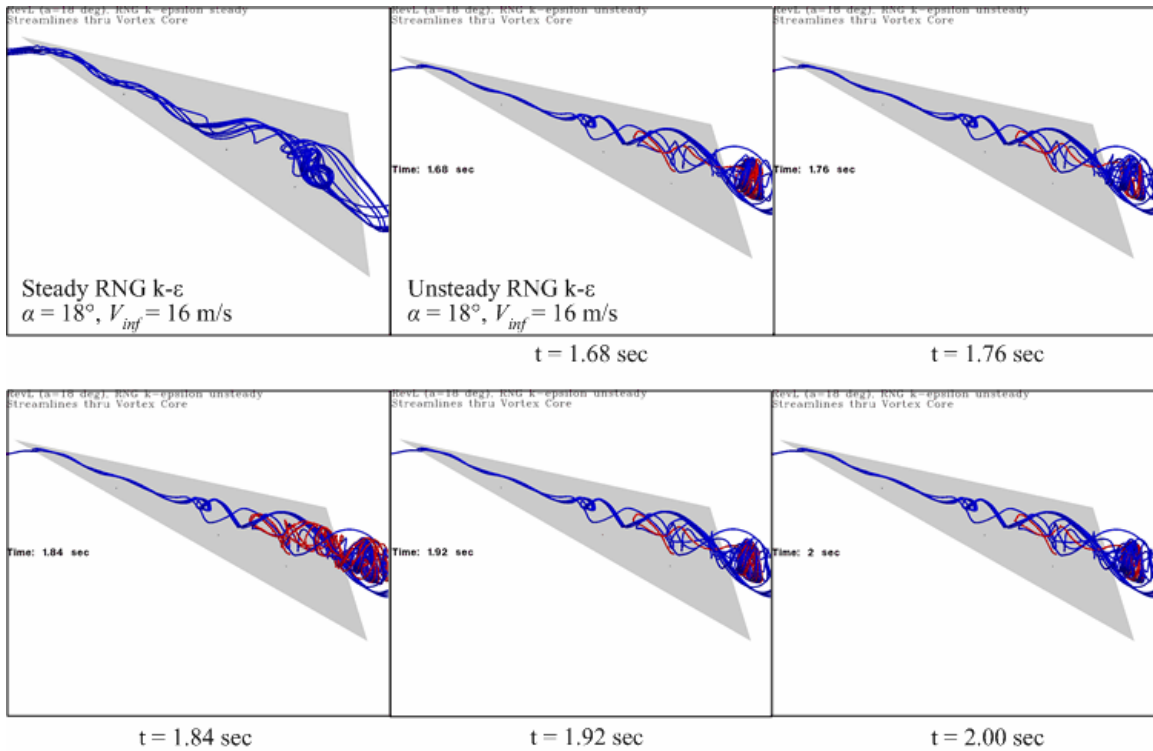


Figure 3.61 – Streamlines through Vortex from Unsteady RNG k-ε Turbulence Model (Revision L, $\alpha = 18^\circ$, $V_\infty = 16$ m/s)

nondimensional velocity contours through the vortex core after flow was fully developed, not included here for brevity, are virtually identical to those in the top right image in Figure 3.45. These unsteady turbulence models' (S-A and k-ε) inaccurate predictions disqualify them as candidates for a suitable unsteady solver for this problem.

Again from the unsteady RSM model, Figure 3.62 compares C_p values at eight different time steps between $t = 1.52$ and 2.08 sec and shows this model failed to accurately predict C_p values comparable to the experimental data. At $x/c = 0.35$ and 0.55 , these data indicate that the flow was fully developed since C_p magnitude and peak locations did not change with time. At $x/c = 0.75$, it appears there was fluctuation in vortex strength, though not to a significant degree. At $x/c = 0.95$, which has an exploded view in Figure 3.63, there is cyclic variation in vortex strength and in centerline location,

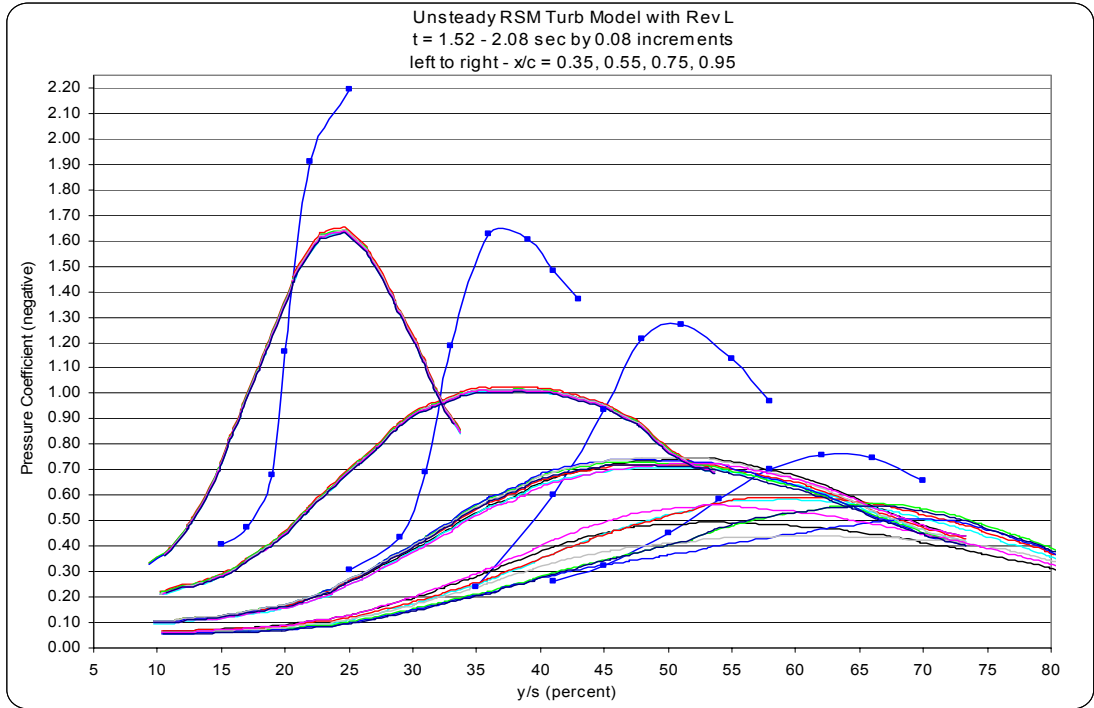


Figure 3.62 – C_p Plots from Unsteady RSM Turbulence Model for $t = 1.52$ - 2.08 sec (Revision L, $\alpha = 18^\circ$, $V_\infty = 16$ m/s)

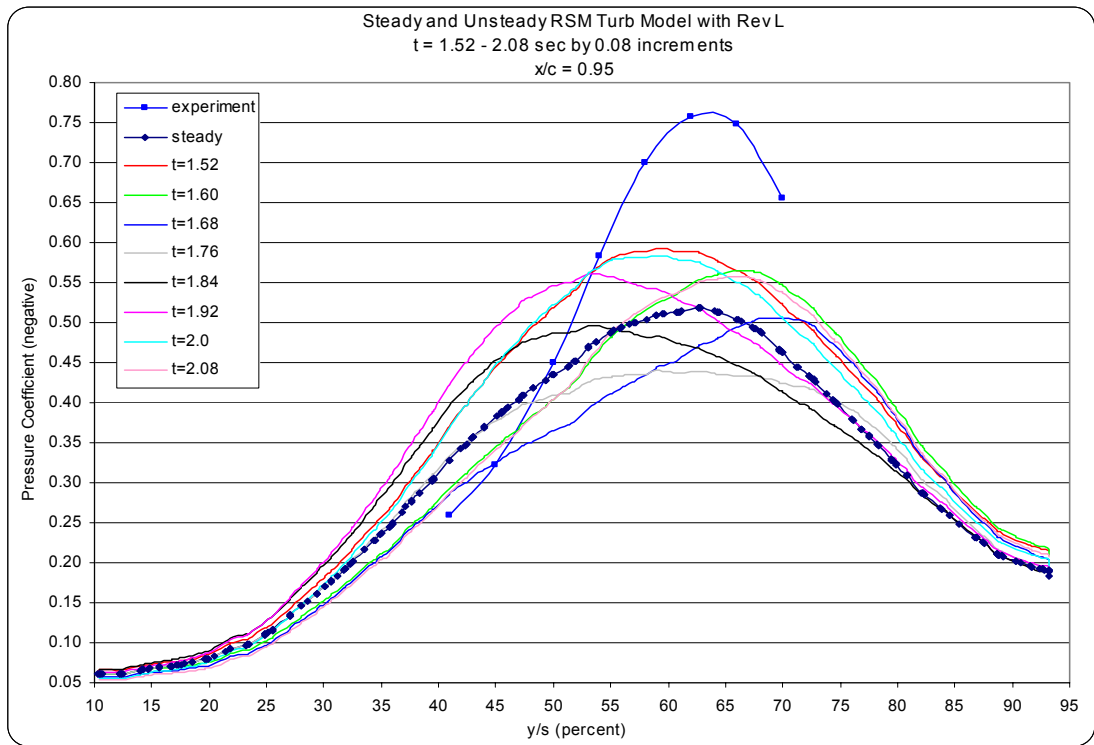


Figure 3.63 – C_p Plots from Steady and Unsteady RSM Turbulence Models for $t = 1.52$ - 2.08 sec at $x/c = 0.95$ (Revision L, $\alpha = 18^\circ$, $V_\infty = 16$ m/s)

where the vortex center wandered between $y/s = 0.53$ and 0.70 , which corresponds to a spanwise range of 3.4 cm. This is consistent with experimental observations that the vortex core meanders several core radii in any given direction. However, the unsteady RSM model did not predict this core meandering farther upstream over the wing.

Inspection of Figure 3.63 also reveals that the vortex core meanders in a cyclic pattern. Following C_P curves by time history on the figure, they translate in an ovular, clockwise direction with a period of about 0.48 sec or frequency of roughly 2 Hz. This is consistent with experimental observations that the vortical structure rotates at 1-2 Hz. This vortical rotation is further evidenced by cyclic variation in C_P magnitude in Figure 3.63; when the vortex core rotates away from the wing surface, static pressure on the surface increases and results in a lower C_P value. Therefore these data show the vortex core rotates outboard and upward over time or in a counter-clockwise rotation, which is consistent with experimental observation that the vortex structure rotates in the same direction with the vortex proper – both are counter-clockwise for the port-side wing when looking downstream. Since data were written every 0.08 seconds (200 time steps or 4,000 computational iterations), it was not possible to show graphically the vortex rotational frequency of several hundred cycles per second. None of this validation with experimental findings was possible using a steady solver. In summary, the unsteady solver is advantageous over steady primarily in predicting several of the dynamic characteristics of the flow. It appears also that the steady RSM model predicted the correct time averaged vortex core centerline position.

Predicting dynamic characteristics of the flow, however, may or may not be important for a given application. The main disadvantages of using an unsteady solver

are the time required to achieve fully developed flow and the arguably insignificant improvement in results. An unsteady solution is obtained in weeks rather than the hours required for a steady solution. There is no question whether time accurate solutions, using the RSM turbulence model, more correctly predict the unsteady phenomena of vortical flow and vortex breakdown, but is prediction of these occurrences critical to the control system which may later be developed with assistance from a numerical flow model and solver? This question of course needs to be addressed by those who will develop the control system.

None of the evaluated unsteady turbulence models were able to predict any variation in vortex breakdown location, which was observed experimentally. Figures 3.64-65 show that flow was fully developed not later than about $t = 1.6$ sec for the unsteady S-A and $k-\epsilon$ models, since the predicted C_p values no longer appreciably

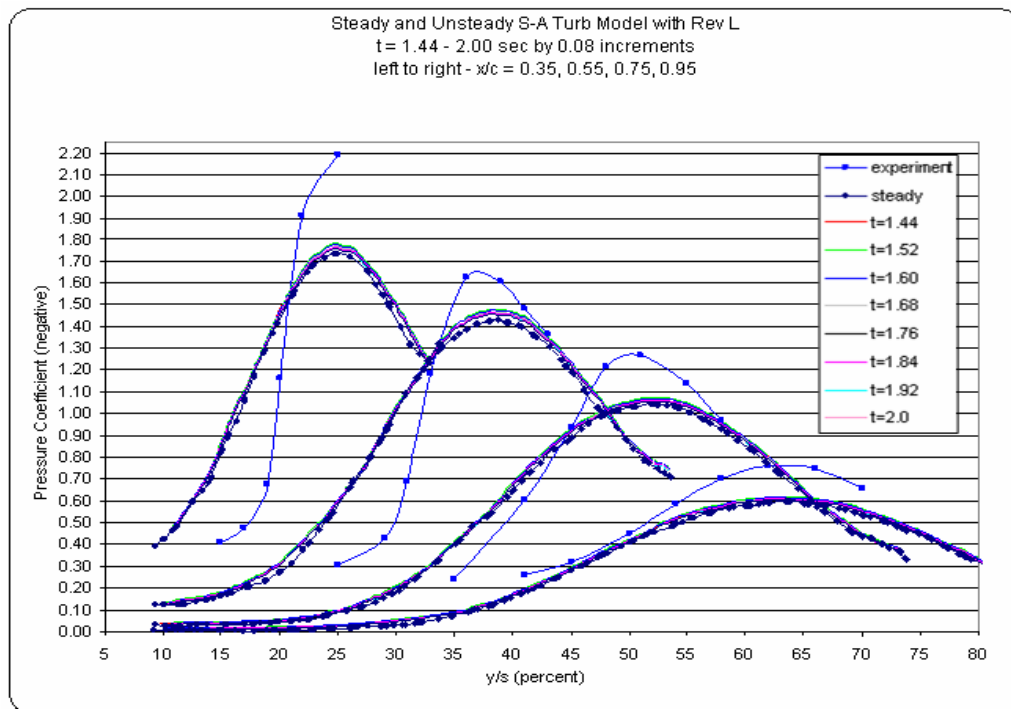


Figure 3.64 – C_p Plots from Unsteady S-A Turbulence Model for $t = 1.44$ - 2.00 sec (Revision L, $\alpha = 18^\circ$, $V_\infty = 16$ m/s)

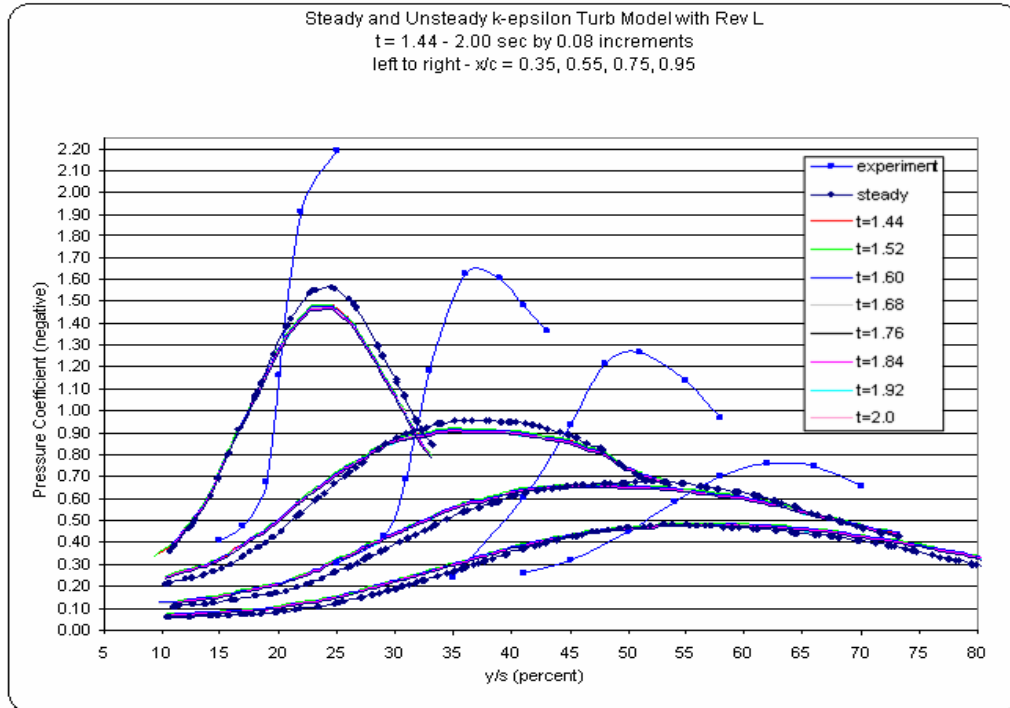


Figure 3.65 – C_p Plots from Unsteady RNG k- ϵ Turbulence Model for $t = 1.44$ - 2.00 sec (Revision L, $\alpha = 18^\circ$, $V_\infty = 16$ m/s)

changed with time. Different from the RSM predicted solution, these models' solutions showed no fluctuation in vortex core location over time. This inability to predict the unsteady flow's physics essentially negates any advantage obtained by using an unsteady solver for these two turbulence models. In fact, unsteady solutions with the S-A or k- ϵ turbulence model give only the great disadvantage of requiring significantly more computation time and resources than the corresponding steady solvers. The RSM turbulence model resulted in a solution with cyclic rotation of the vortex core centerline but aft of vortex breakdown. This result, seen for the RSM case in Figures 3.62, 3.63 and 3.66, is good and bad – good because it may be easier to control breakdown if it is predicted to remain in a steady location, and bad because it failed to accurately model the physical happenings within the bursting vortical flow field.

The steady RSM solution predicted location of vortex breakdown just as well as the time accurate solver, where both solvers showed its occurrence at $x/c = 0.45$. Figure 3.63's dark blue line with diamond markers shows the steady RSM prediction, which appears to be an excellent averaged value of the unsteady predicted C_p values, though it does not show local extrema. Figures 3.64-65, which also indicate the steady C_p curves via dark blue lines with diamond markers, show that the steady S-A and k- ϵ models adequately averaged the unsteady flow properties.

Total pressure contours in Figure 3.66 show that the RSM steady solution (top left) closely matches any of the unsteady snapshots of the solution, where the small variations occur along the secondary vortex and aft of $x/c = 0.65$ for the primary vortex. Nondimensional velocity contours in Figure 3.67 are quite similar for steady and unsteady RSM predictions everywhere except within the vortex core between $x/c = 0.70$ and 1.20, which may be a region of little significance for vortex breakdown control. Figure 3.68 shows nondimensional velocity contours predicted by k- ϵ steady and unsteady solvers and indicates that both predict the same basic vortex and vortex breakdown structures. Figures 3.67 and 3.68 further indicate that neither the S-A nor k- ϵ models predicted any fluctuation in vortex core location over time and that their steady-state solutions were essentially equivalent. It is worth repeating that none of the turbulence models evaluated in this study adequately predicted wing surface pressure values and vortex strength and size, when compared to the UC experimental data.

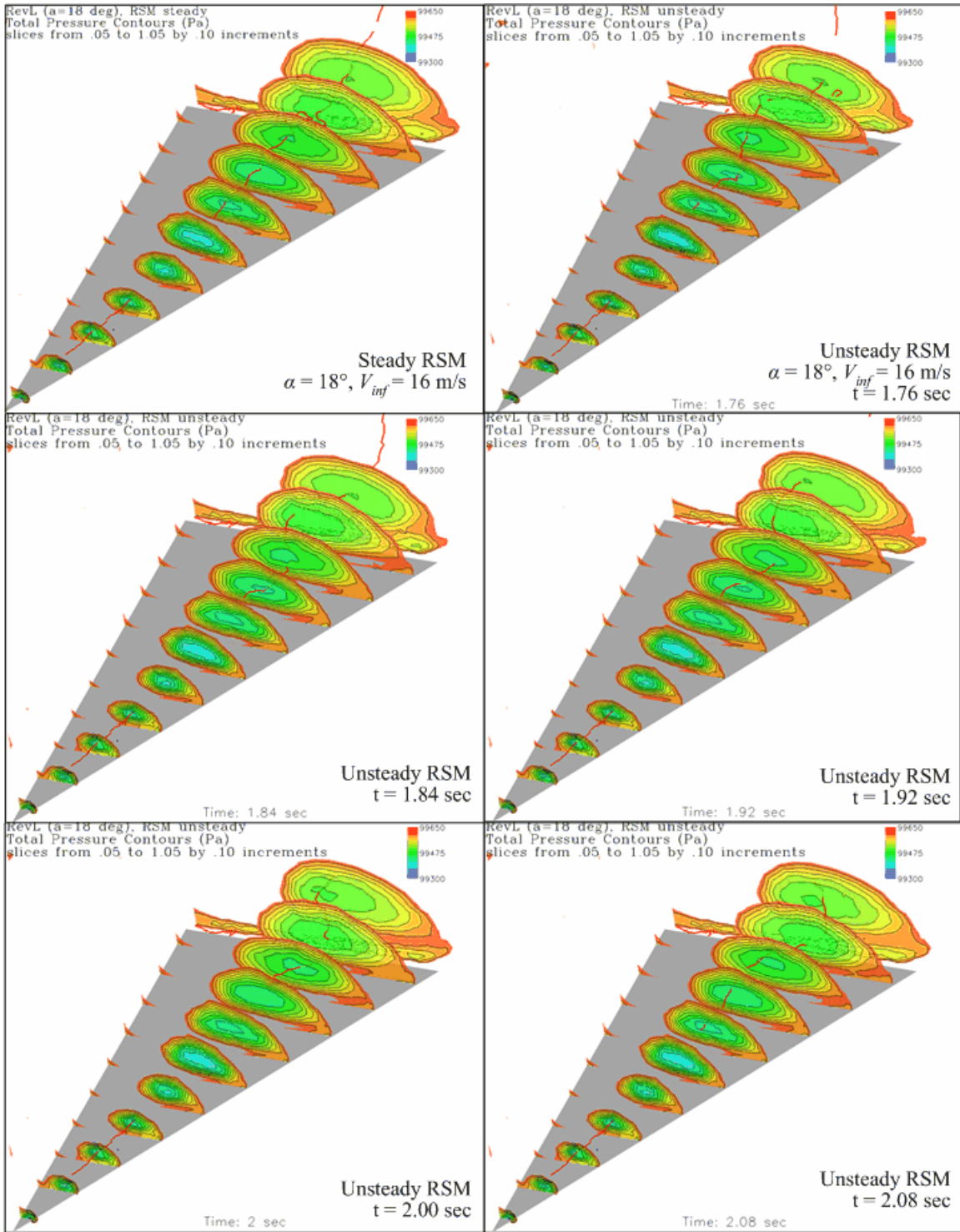


Figure 3.66 – Total Pressure Contours from Steady and Unsteady RSM Turbulence Models (Revision L, $\alpha = 18^\circ, V_\infty = 16 \text{ m/s}$)

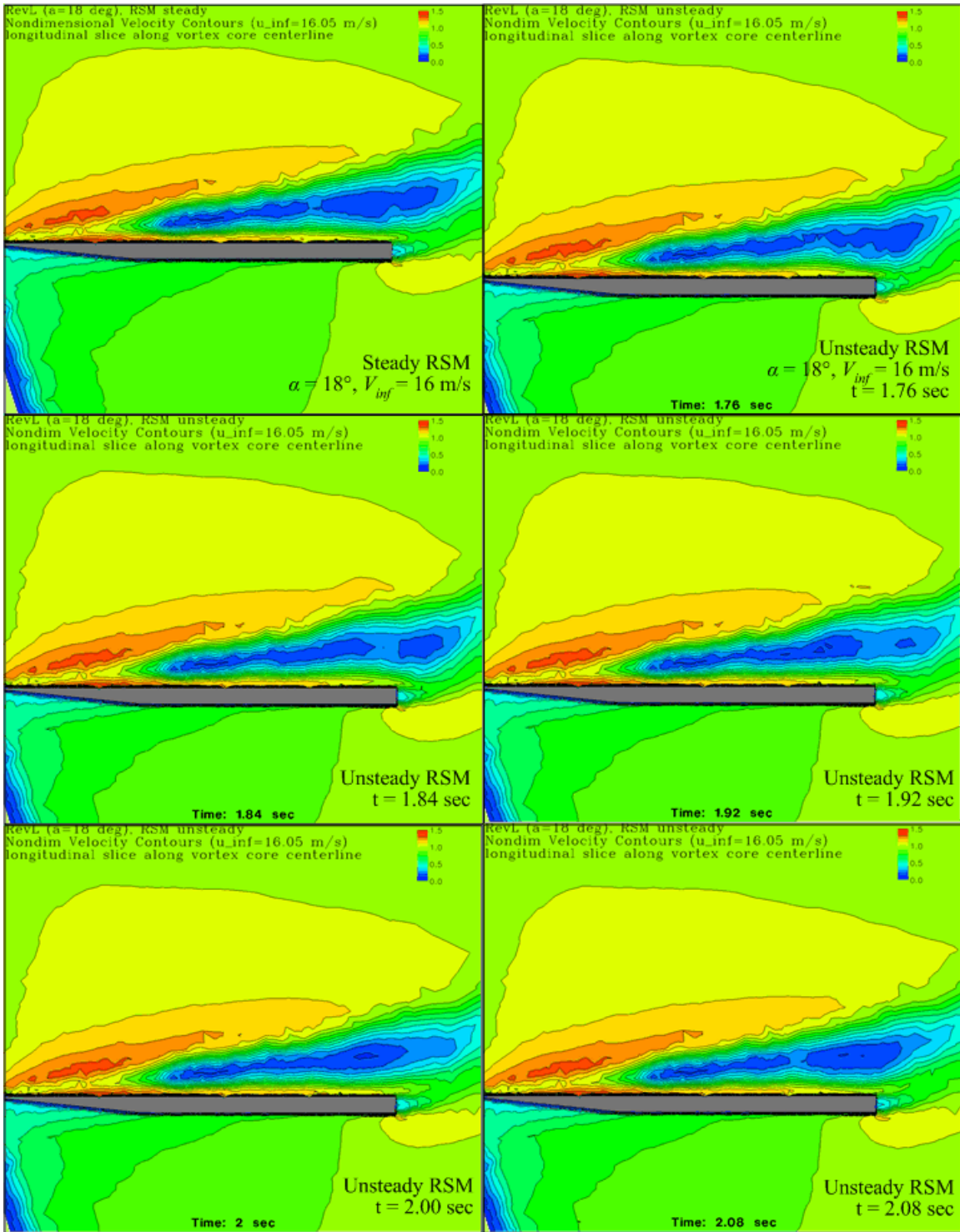


Figure 3.67 – Nondimensional Velocity Contours through Vortex Core from Steady and Unsteady RSM Turbulence Models (Revision L, $\alpha = 18^\circ, V_\infty = 16$ m/s)

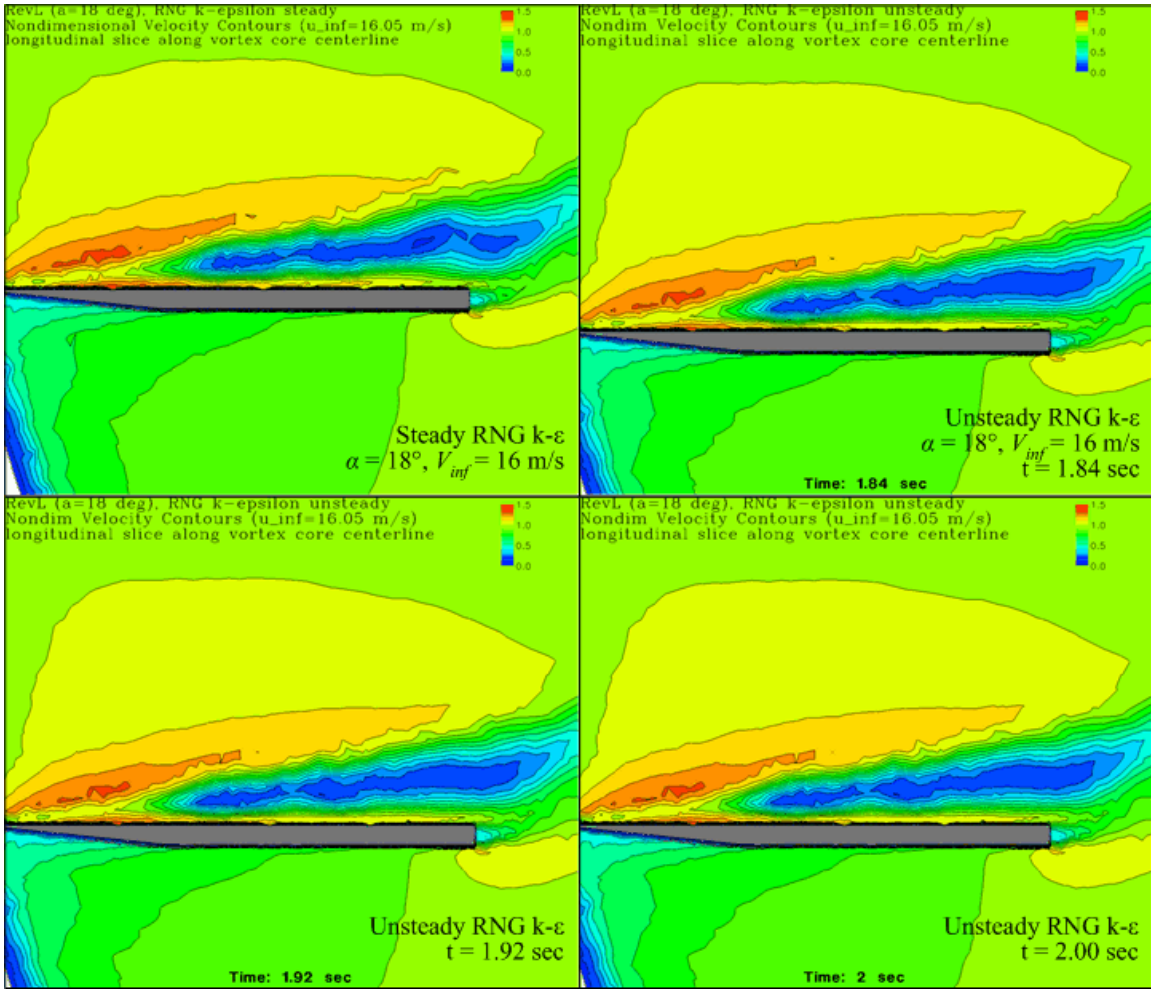
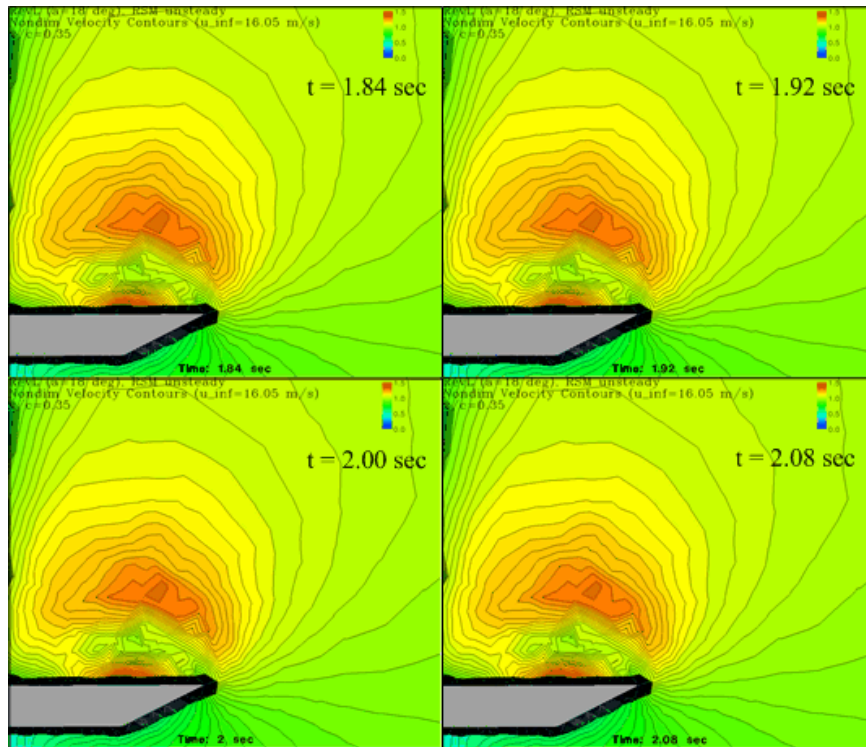
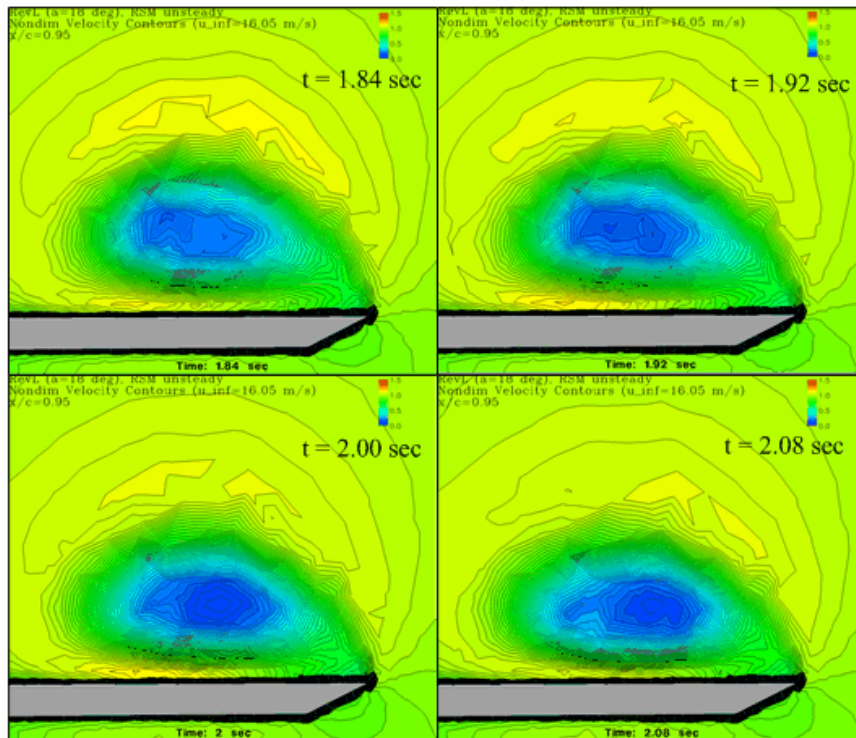


Figure 3.68 – Nondimensional Velocity Contours through Vortex Core from Steady and Unsteady RNG k- ϵ Turbulence Models (Revision L, $\alpha = 18^\circ$, $V_\infty = 16$ m/s)

Figure 3.69 was included primarily to show that computational solutions may be closely compared against experimentally determined velocity contours within the vortical flow field (Guillot, 1999: 41). This figure also shows that the vortex was steady over time at $x/c = 0.35$ but that its higher pressure core varied considerably over time at $x/c = 0.95$.



Unsteady RSM, $\alpha = 18^\circ$, $V_{inf} = 16$ m/s, $x/c = 0.35$



Unsteady RSM, $\alpha = 18^\circ$, $V_{inf} = 16$ m/s, $x/c = 0.95$

Figure 3.69 – Nondimensional Velocity Contours at $x/c = 0.35$ and 0.95 from Unsteady RSM Turbulence Model (Revision L, $\alpha = 18^\circ$, $V_\infty = 16$ m/s)

Comparing performance of the three unsteady turbulence models – S-A, RNG k-ε and RSM, Table 3.4 shows the unsteady S-A model predicted a C_L value closest to the experimental value, while the k-ε and RSM predictions were within 6-8% of that value. The S-A and RSM unsteady solvers predicted C_L values which improved upon the steady prediction by 1.0 and 1.6%, respectively, while the k-ε prediction varied only by 0.1% between steady and unsteady solvers.

Table 3.4 – Comparison of C_L for Steady and Unsteady (at $t = 2.0$ sec) Turbulence Models (Revision L, $\alpha = 18^\circ$, $V_\infty = 16$ m/s)

Turbulence Model	C_L	
	steady	unsteady
S-A	0.797	0.805
RNG k-ε	0.738	0.737
RSM	0.740	0.752
Experiment	0.8	-

Figure 3.70 shows predicted C_P values at the four chordwise locations at $t = 2.00$ sec, where flow was fully developed in each case. These results are quite similar to steady results seen in Figures 3.41-44, effectively casting doubt upon the unsteady solvers' utility for this problem. At each chordwise location plotted in Figure 3.70, the unsteady S-A turbulence model most closely predicted peak experiment C_P values (or vortex strength), C_P curve slopes (or extent of the generated vortex), and peak C_P location (or location of vortex core centerline). Since the unsteady S-A model failed to predict vortex breakdown or any unsteadiness within the vortex structure, however, it is an unacceptable numerical model. Further, based on results in Figure 3.70, neither the unsteady k-ε nor RSM models predicted acceptable pressure values over the wing surface, excluding them also as viably acceptable numerical models.

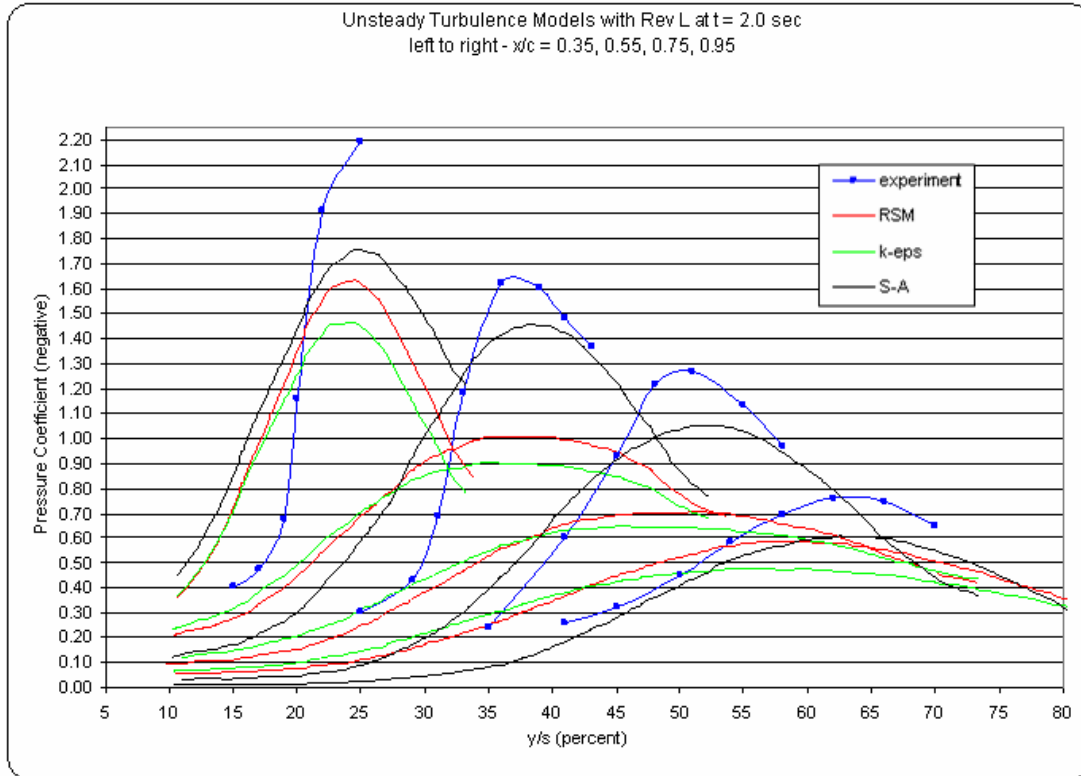


Figure 3.70 – C_p Plots from Unsteady Turbulence Models at $t = 2.00$ sec
(Revision L, $\alpha = 18^\circ$, $V_\infty = 16$ m/s)

In summary, as was the case with the steady turbulence models, none of the time accurate models adequately predicted vortex strength or dimensional extents, when compared with testing data from UC. Each of them under-predicted strength of the vortex and over-predicted its size. While the unsteady S-A model again came closest in predicting C_p and C_L values, it failed to unquestionably predict occurrence of vortex breakdown and certainly failed to correctly predict pressure and velocity gradients within the vortex. The unsteady RSM turbulence model predicted cyclic meandering of the vortex core position, though not as far upstream as was noted experimentally, and predicted no variation in vortex breakdown location. Unsteady S-A and RNG k- ϵ models categorically failed to predict any of the unsteady characteristics of vortical flow and vortex breakdown over a delta wing.

There are no clear answers to whether a steady model may suffice for this control problem; it will depend largely on user requirements, which as yet are unspecified. One possible course of action would be to use an unsteady solver with a given turbulence model to validate accurate correlation with the flow physics then use its corresponding steady (quicker) solver to predict vortex breakdown position given various initial conditions.

IV. Numerical Simulation with Flow Control

This chapter presents results for along-core blowing to control vortex breakdown over the half delta wing numerical flow model. In the following sections, the numerical mesh generation and adaptation as well as the selected flow solver parameters will be discussed before presenting results.

Mesh Generation and Adaptation

While some along-core blowing trial runs were performed on earlier grid models, the final configuration utilized Mesh Revision L, discussed in Chapter III. However, it is worthwhile to include discussion of a modification to the initial Revision L, a mesh adaptation of Revision L's blowing axis, and creation of Revision M.

All of the initial meshes included the wing's three blowing ports, though they were set as a wall boundary condition; thus they served both as placeholders for later blowing and as markers to verify that predicted location of the vortex core centerline aligned with the experimentally identified centerline. From these early solutions, it appeared the vortex core was not properly aligned, so when one of the ports was activated to provide blowing, it affected neither the vortex nor its breakdown. This result agreed with an observation in the experimental LSU study that when blowing is angled to miss the vortex core, the jet's mass flow joins the larger, swirling vortex flow and does not affect breakdown (Guillot, 1999).

Before moving port locations to better align with the vortex core to generate qualitative results – as experimental configuration would have been violated, negating

quantitative assessment – a close comparison was made between wing drawing, which was not the fabrication drawing, and a digital image of the actual wing. Since they did not agree, the ports in grid Revision L were moved to locations determined from the image; consequently, these locations proved to be aligned with the vortex core centerline. The ports were numbered such that port 1 was closest to the wing apex, located at $x/c = 0.30$ and $y/s = 0.209$ (where s is the wing half span or 19.8 cm); port 2 was located at $x/c = 0.60$ and $y/s = 0.409$; and port 3 was closest to the trailing edge, located at $x/c = 0.80$ and $y/s = 0.543$. The spanwise locations would not be valid for different wing angles of attack, though jet angles could be appropriately modified to compensate for a different vortex location.

With this corrected configuration, blowing still failed to affect vortex breakdown. It was not discovered until later that this failure occurred in part because the degree of vortex breakdown was not significant enough to merit affectation. That is, the S-A turbulence model failed to sufficiently predict vortex bursting, or pressure and velocity gradients within the core, for the blowing to take effect any more than it would affect a vortex with no breakdown. Nonetheless at that time, in hopes of better resolving jet blowing into the vortex core, Mesh Revision L was adapted in FLUENT by refining cells in the region defined by a cylinder 0.5 cm in radius and 6.0 cm in length, where the leading end or cylinder top was centered on the port and aligned normal to the blowing vector, as shown in Figure 4.1. Adaptation was performed twice on this region and created an additional 11,000 nodes and 56,000 tetrahedral cells.

After the adapted mesh did not improve results, still before realization of error in turbulence model selection, and after noting minute mass flow loss at the port, Revision

M modified the numerical mesh to allow for blowing normal to the port surface. Figure 4.2 shows a shaded visualization of the grid at and around a blowing port; this revision modeled more precisely the test article's blowing ports. Building this numerical model required great attention to ensure the port was set perfectly normal to the three-

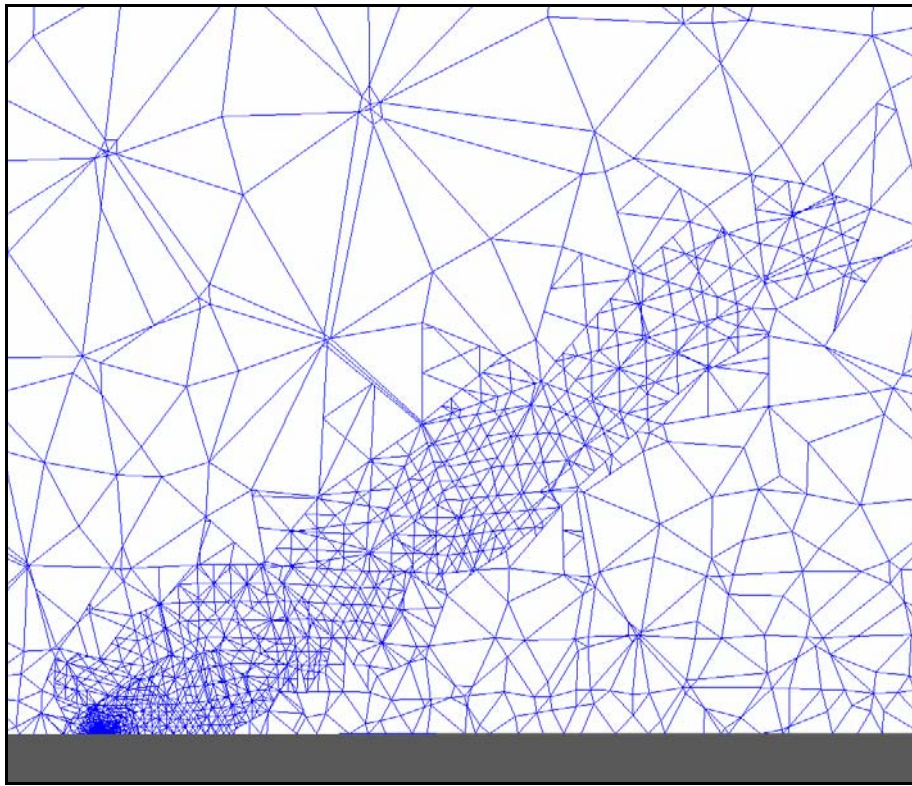


Figure 4.1 – Mesh Adaptation to Revision L in Jet Blowing Region

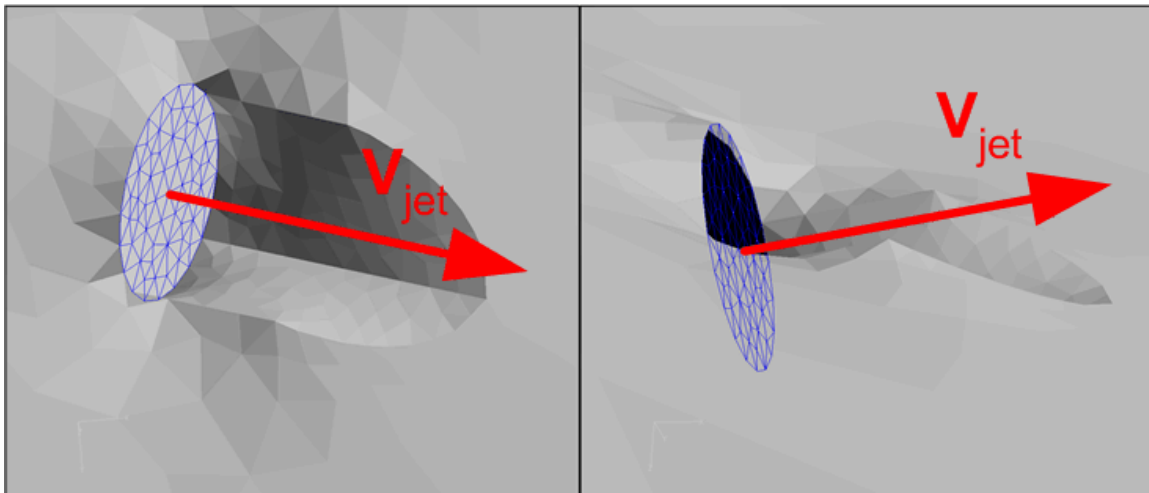


Figure 4.2 – Mesh Generation, Revision M: Views of Recessed, Angled Blowing Port

dimensional blowing vector. Since the final model from this study may ultimately be used to show vortex breakdown sensitivity to different blowing angles, this revision was abandoned due to the need to carefully rebuild a grid for each variation of blowing angle. On the other hand for Revision L, the user need only alter the directional components for each blowing port boundary condition. The final answer was that mesh Revision L was suitable for the blowing cases. However, due to apparent dissipation of the jet momenta, as shown later in this chapter, it would be prudent to investigate further refinement of the numerical mesh's port blowing regions.

Solver Parameters

For blowing cases, the same final model configuration was used except the active port's boundary condition was changed from impermeable wall to either velocity or pressure inlet in the FLUENT *define*→*boundary conditions* menu. Specifying a velocity inlet was preferred because it required no translation between pressure and velocity values; the user need only input the desired velocity, combined with directional components. While FLUENT warns, “This [velocity inlet] boundary condition is intended for incompressible flows, and its use in compressible flows will lead to a nonphysical result because it allows stagnation conditions to float to any level” (FLUENT, 2001: 6.4), the user may circumvent the issue of uncontrolled stagnation conditions by specifying an outflow gauge pressure (99.34 kPa for Port 1) which corresponded to the experimentally measured pressure near the blowing port. If those data were unavailable, the user would likely need to use the pressure inlet boundary

specification. Additionally, since most of the flow within the numerical wind tunnel was indeed uncompressed, using the incompressible-preferred velocity inlet at the port was not a poor assumption.

Other required inputs at the blowing port boundary included temperature, set at 298 K, either or both of turbulent viscosity ratio (TVR) and turbulence intensity, depending on turbulence model used, and Cartesian components for the blowing vector. TVR was set at 1 and turbulence intensity was 0.05%, both indicating laminar flow at the blowing port. Components for the blowing vector were calculated using the transformation matrix found in Appendix D. For $\alpha = 18^\circ$, jet elevation angle = 35° and jet azimuthal angle = 155° , they were determined to be *x-component* = 0.883313, *y-component* = 0.346189, and *z-component* = -0.316088. The resultant blowing vector was angled precisely into the center of the vortex core. All steady and unsteady blowing cases were partitioned to compute in parallel on between 12 and 18 processors.

A sub-study was performed to assess any adverse ramifications of using a velocity inlet instead of the FLUENT-recommended pressure inlet for compressible flow. For each case the steady solver with S-A turbulence model was used, with $\alpha = 18^\circ$ and $V_\infty = 16.05$ m/s. Comparisons were made for blowing velocities of 200 and 250 m/s. For the pressure inlet cases, initial pressure was set at 99.56 kPa and total gauge pressures were set at 126.8 and 146.1 kPa, corresponding to the respective velocities. Comparison of C_L in Table 4.1 shows that difference between using pressure or velocity inlet is negligible. Further, comparison of C_P in Figure 4.3 shows no difference between the two inlet conditions for the case with blowing at 250 m/s; the case with blowing at 200 m/s had comparable results.

Table 4.1 – Comparison of C_L from Varied Inlet Specification and Port Blowing Velocity

Case	V_{jet} (m/s)	C_L
Pressure Inlet	200.0125	0.8054
Velocity Inlet	200	0.8091
Pressure Inlet	250.0017	0.8048
Velocity Inlet	250	0.8079

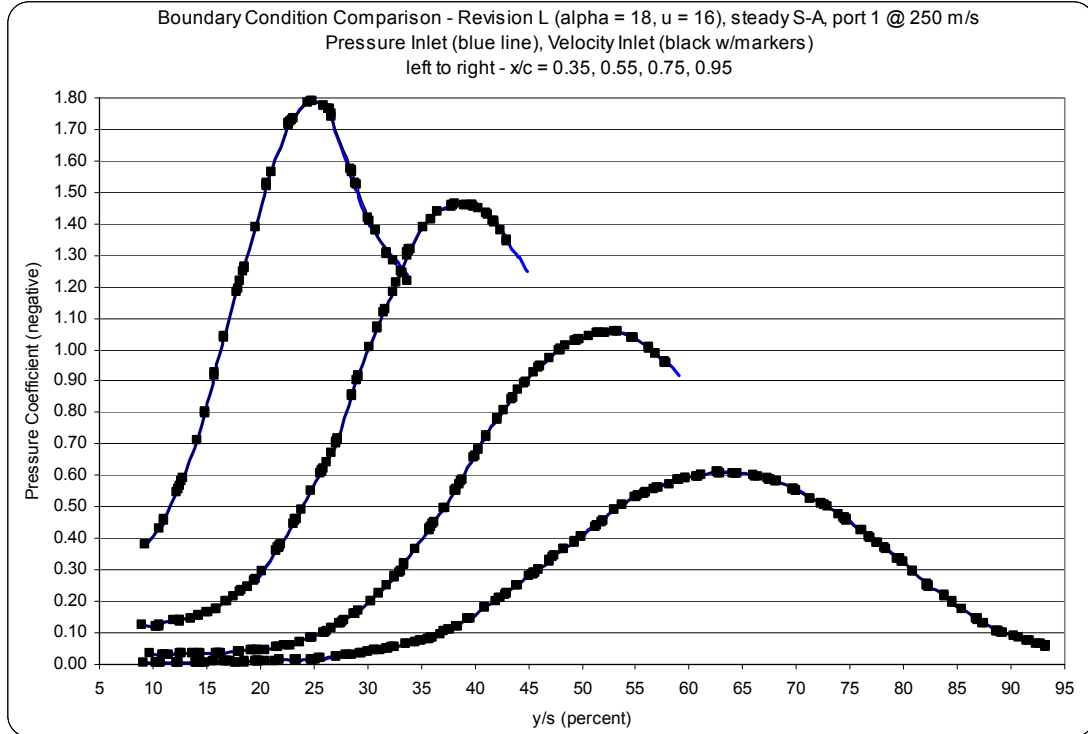


Figure 4.3 – C_P Comparison from Velocity and Pressure Inlet at Blowing Port 1 (Revision L, Steady S-A, $\alpha = 18^\circ$, $V_\infty = 16$ m/s)

Because the S-A turbulence model did not adequately predict vortex breakdown and because the two-equation RNG $k-\epsilon$ model was lower in fidelity by definition, the seven-equation, time accurate RSM turbulence model was used to evaluate effects of along-core blowing into the vortex. Since this turbulence model previously demonstrated its inability to accurately predict vortex strength and size or shifting of the vortex breakdown location, its predicted solutions were compared qualitatively rather than quantitatively with experimental data from UC and LSU.

Computational Plan of Attack

With the exception of the sub-study and numerical mesh assessments discussed above, it was determined that blowing cases were to be evaluated using a time accurate flow solver due to the inherently and highly unsteady nature of the vortical flow and breakdown. All blowing cases used second-order temporal and spatial discretization with CFL = 5; for the unsteady cases, $\Delta t = 0.0004$ sec, which was the same step-size used for non-blowing cases. Two basic strategies were attempted with the unsteady blowing cases: initialize and run the case with blowing active, and run the case using an initial, fully-developed-flow solution from a no-blowing case. Both strategies proved unsuccessful because the blowing momenta of the jets were numerically overwhelmed by the primary vortex momentum as will be shown.

Results

Bottom line for the numerical cases with along-core blowing is that all three-dimensional attempts to affect vortex breakdown were unsuccessful. In Figure 4.4, nondimensional velocity contours from a two-dimensional, steady S-A model showed effects from blowing; that is, vortex breakdown was not necessarily eliminated, but its effects were clearly changed to give a smaller region of vortical flow. Interestingly, the S-A model predicted vortex breakdown in the two-dimensional numerical case but not in the three-dimensional case. Expanding to three dimensions introduced numerical issues which were not resolved.

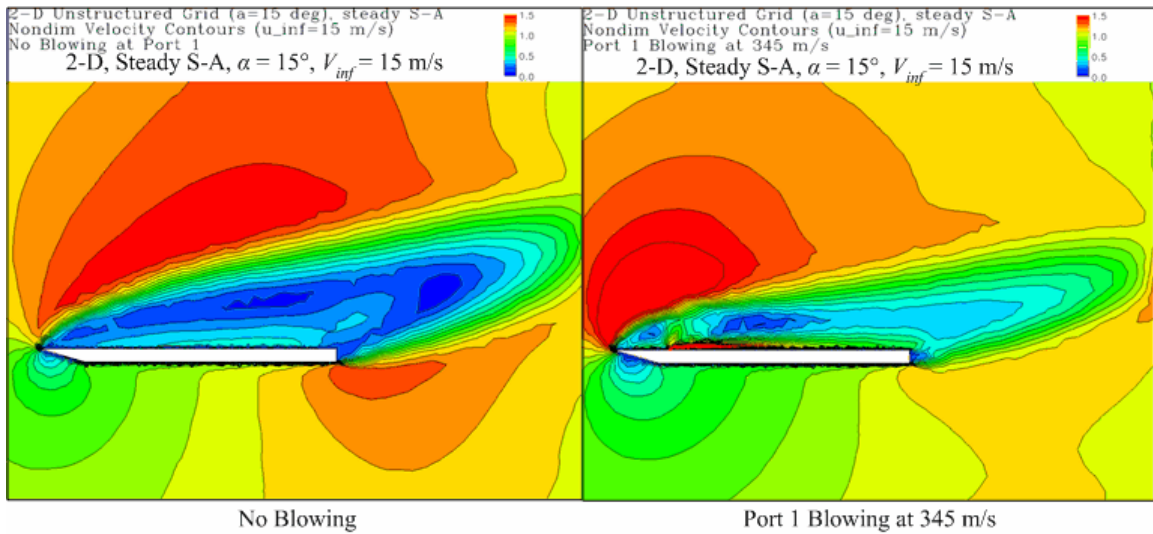


Figure 4.4 – Two-Dimensional Solution with and without Blowing at Port 1 (Steady S-A, $\alpha = 15^\circ$, $V_\infty = 15$ m/s)

Figure 4.5 shows streamlines (blue lines) and vortex core centerline identification (red line) from Mesh Revision L's unsteady, RSM turbulence cases with and without blowing. The left column shows the predicted solution with no blowing at $t = 0.08, 0.16$ and 0.24 sec. These images indicate that the flow solution was far from being fully developed, since the vortex breakdown position continued to move upstream along the wing surface over time, moving from $x/c = 0.75$ to about 0.55 . The middle column of images shows the predicted solution with sonic blowing (345 m/s) at Port 1 – all other conditions, models and solvers being the same as those from the left column – and the right column shows the results with sonic blowing at all three ports. The case with blowing from all three ports was attempted in an effort to introduce more blowing momentum into the primary vortex core. Inspection of these three columns of images reveals that there are so significant differences between the cases at the same time snapshots. Each predicts vortex breakdown at the same location, indicating failure to delay breakdown.

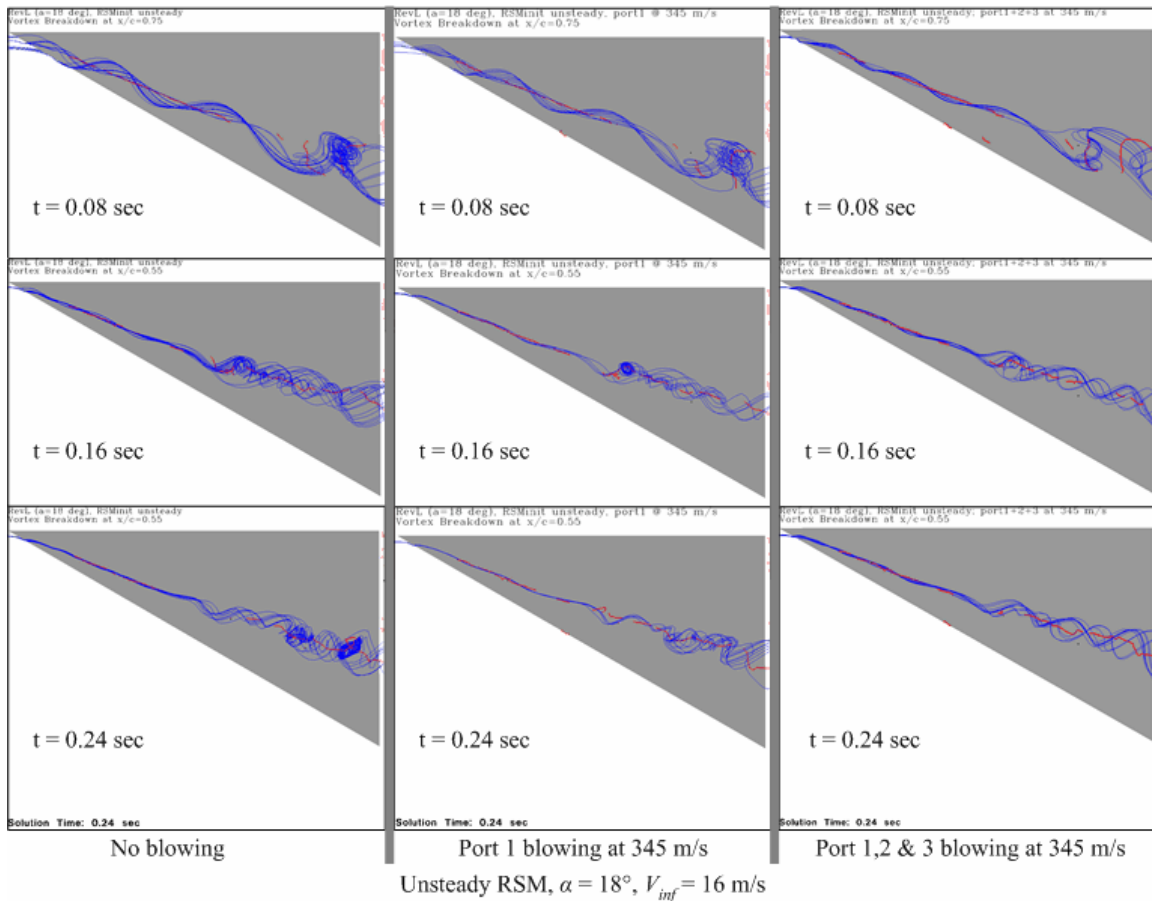


Figure 4.5 – Vortex Breakdown via Streamlines for Unsteady RSM Model at No Blowing and Blowing Configurations (Revision L, $\alpha = 18^\circ$, $V_\infty = 16$ m/s)

Figure 4.6 shows the unsteady RSM solution with sonic blowing from all three ports at $t = 0.24$ sec. Nondimensional velocity contours and blue streamlines through the vortex core indicate that vortex breakdown was not delayed by introducing blowing momentum. Nondimensional velocity vectors were included to show that each port's blowing vector was precisely aligned with the vortex core centerline; by rotating this graphic and inspecting from above (image not included here), it was observed that the blowing vector lines actually bisected the core streamlines. Red and purple streamlines emanate from the blowing ports and show that mass flow from the jets was swept around the vortex instead of entering its core, thus negating their effect. This indicates that the

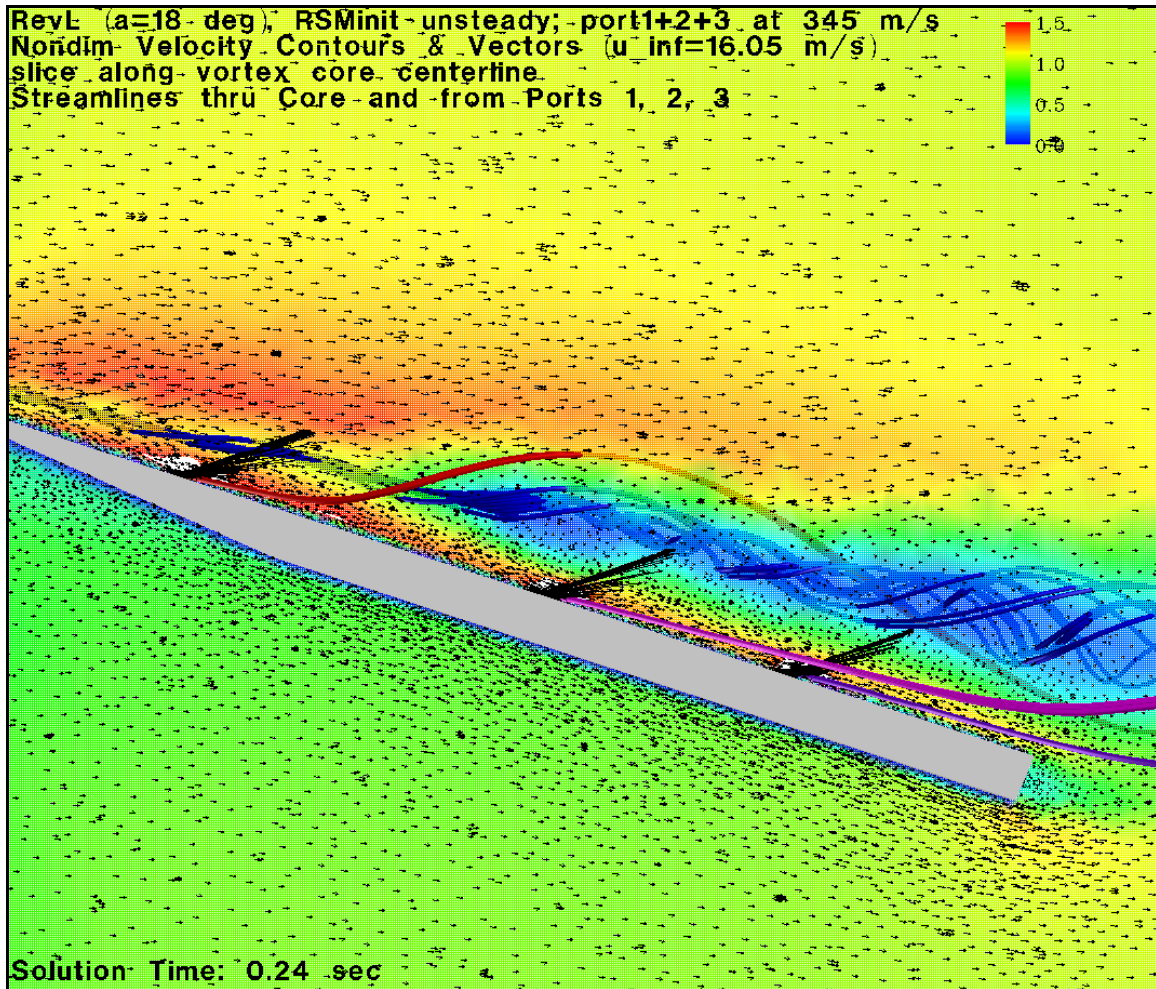


Figure 4.6 – Effect of Port 1+2+3 Sonic Blowing on Unsteady RSM Solution
(Revision L, $\alpha = 18^\circ$, $V_\infty = 16$ m/s)

jet momenta were either overwhelmed by momentum of the primary vortex or dissipated before reaching the vortex core.

Figure 4.7 compares C_p curves at the four chordwise positions for cases with no blowing and with sonic blowing from Ports 1, 2 and 3, using Mesh Revision L, unsteady RSM turbulence model at $t = 0.24$ sec. Blowing resulted in no notable improvements at $x/c = 0.35$ and 0.95 . Peak C_p magnitudes increased by 8.2% at $x/c = 0.55$ and 6.1% $x/c = 0.75$. Without continuing computation of this blowing case to roughly $t = 1.6$ sec, it is uncertain whether these improvements would be maintained. Also these improvements

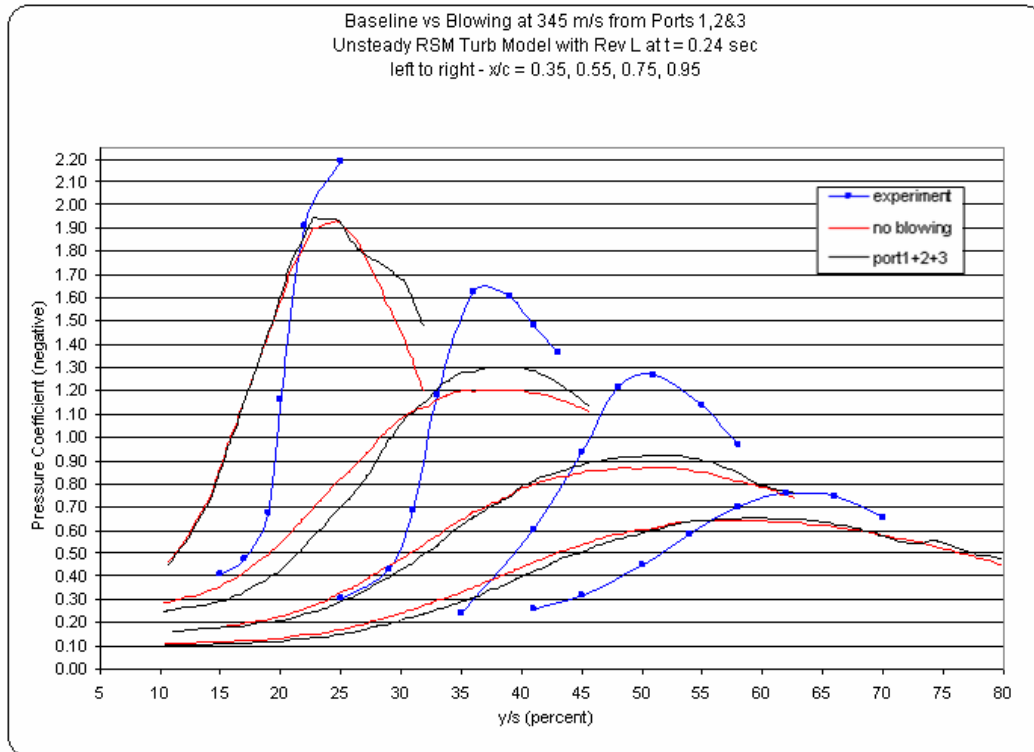
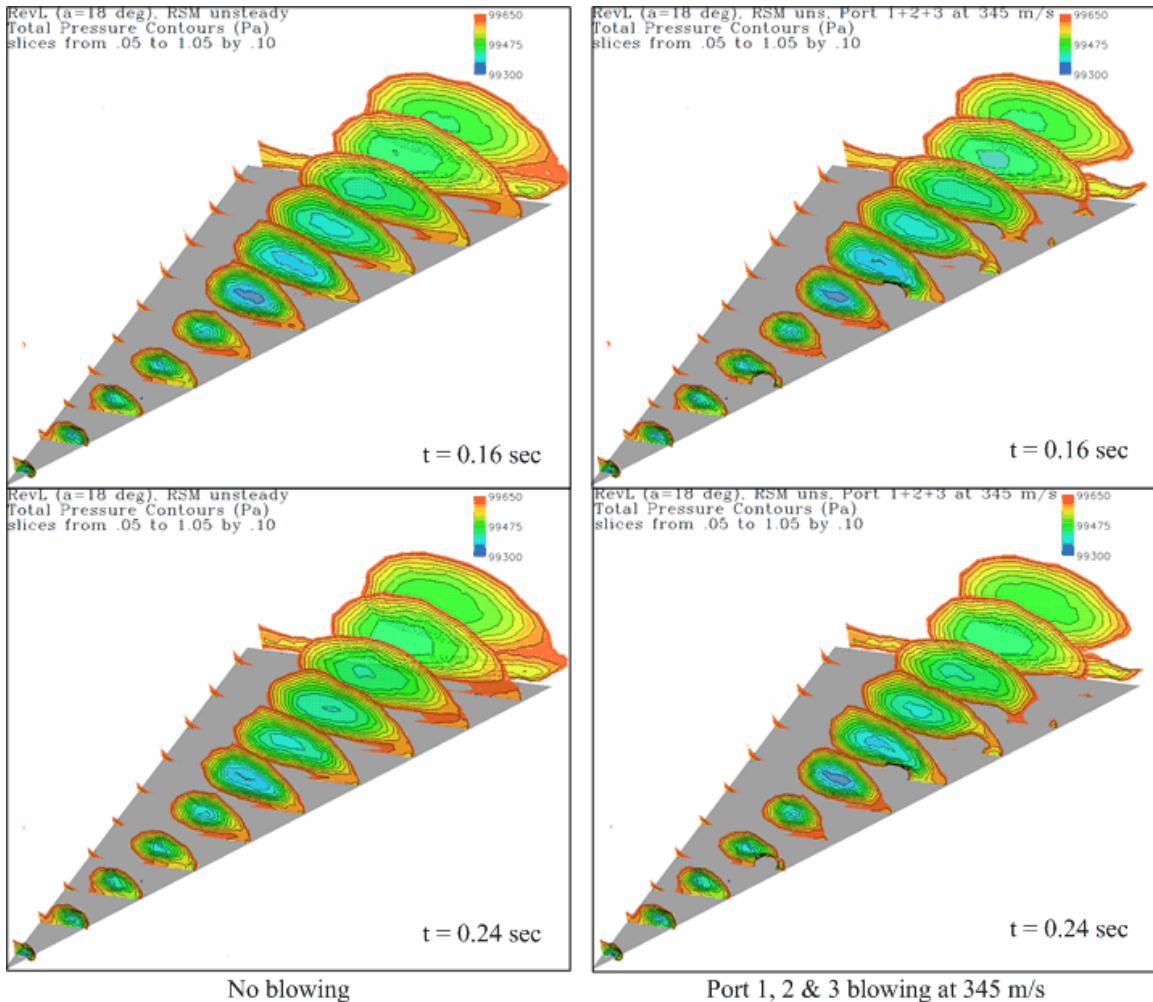


Figure 4.7 – C_p Comparison of No Blowing vs Sonic Blowing at Ports 1, 2, and 3 at $t = 0.24$ sec (Revision L, Unsteady RSM, $\alpha = 18^\circ$, $V_\infty = 16$ m/s)

are insignificant in comparison with those obtained in experimental testing at UC, where peak C_p magnitudes increased over the baseline values by as much as 17, 11, 36 and 63% at $x/c = 0.35, 0.55, 0.75$ and 0.95 , respectively (May, 2002.a).

Figure 4.8 compares contours of total pressure at $t = 0.16$ and 0.24 sec for cases with no blowing and with sonic blowing from Ports 1, 2 and 3, using the unsteady RSM turbulence model. These images show that the vortex core remains essentially unaffected by the blowing. The images from the blowing case (right column) show “holes” or small regions of higher pressure downstream of the blowing ports and close to the wing surface. This is an additional indication that while blowing does affect the flow, it dissipates prior to reaching the vortex core and is swept into the vortex’ momentum.



Unsteady RSM, $\alpha = 18^\circ$, $V_{inf} = 16$ m/s

Figure 4.8 – Contours of Total Pressure for Cases with No Blowing and Sonic Blowing at All Ports (Revision L, Unsteady RSM, $\alpha = 18^\circ$, $V_\infty = 16$ m/s)

Since altering the wing angle of attack would likely have little effect on improving this issue with blowing jet momentum, the next attempt was to increase the freestream velocity to perhaps ease the computational complexity of predicting flow at low freestream velocity. Figure 4.9 compares results from four cases – no blowing and blowing with $V_\infty = 16$ m/s (top row); and no blowing and blowing with $V_\infty = 103.8$ m/s or $M_\infty = 0.30$ (bottom row). These images show there was no effect from Port 1 blowing at two different freestream velocities.

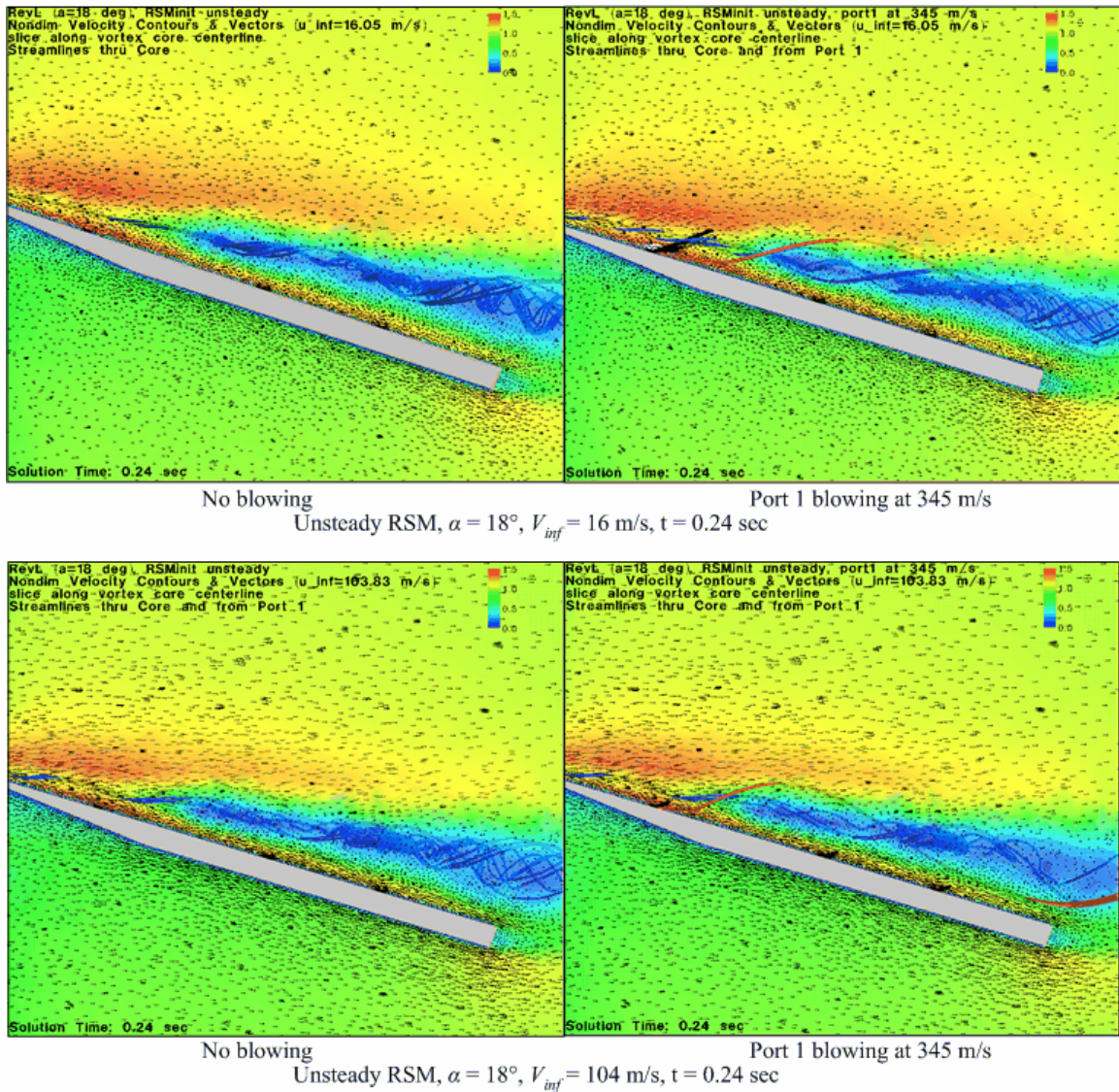


Figure 4.9 – Effect of Port 1 Sonic Blowing on Unsteady RSM Solution for $M_\infty = 0.04$ and 0.3 (Revision L, $\alpha = 18^\circ$)

All of the above cases initialized blowing at $t = 0$ sec. In another sub-study to show any effect from introducing blowing jet momentum, the unsteady, RSM case with blowing from Port 1 was initialized at $t = 2.12$ sec from the case with no blowing. Initializing sonic blowing from a solution with fully developed flow also had no effect on the vortex or on location of vortex breakdown. After running the case for 0.08 sec (4,000 iterations or 200 time steps), the solution appeared nearly identically to the top right

image in Figure 4.9, again indicating that vortex momentum may have overwhelmed momentum introduced by the blowing jet. Predicted C_P and C_L values changed by tenths of a percent, where the LSU study showed that blowing from Port 1 increased lift by 60%, or from $C_L = 0.8$ to 1.28 (Guillot, 1999: 32, 50).

In another case, freestream velocity was decreased to 5 m/s, where blowing was sonic from jet Port 1, using a steady S-A model. An attempt with zero freestream velocity was numerically unstable, but using a low velocity demonstrated more the inadequacy of the jet blowing model rather than the possibility of numerically overwhelmed flow momentum. As with Figures 4.6 and 4.9, Figure 4.10 shows that the blowing momentum appeared to not reach the vortex structure but was either immediately swept into its rotating flow or quickly dissipated before affecting even this

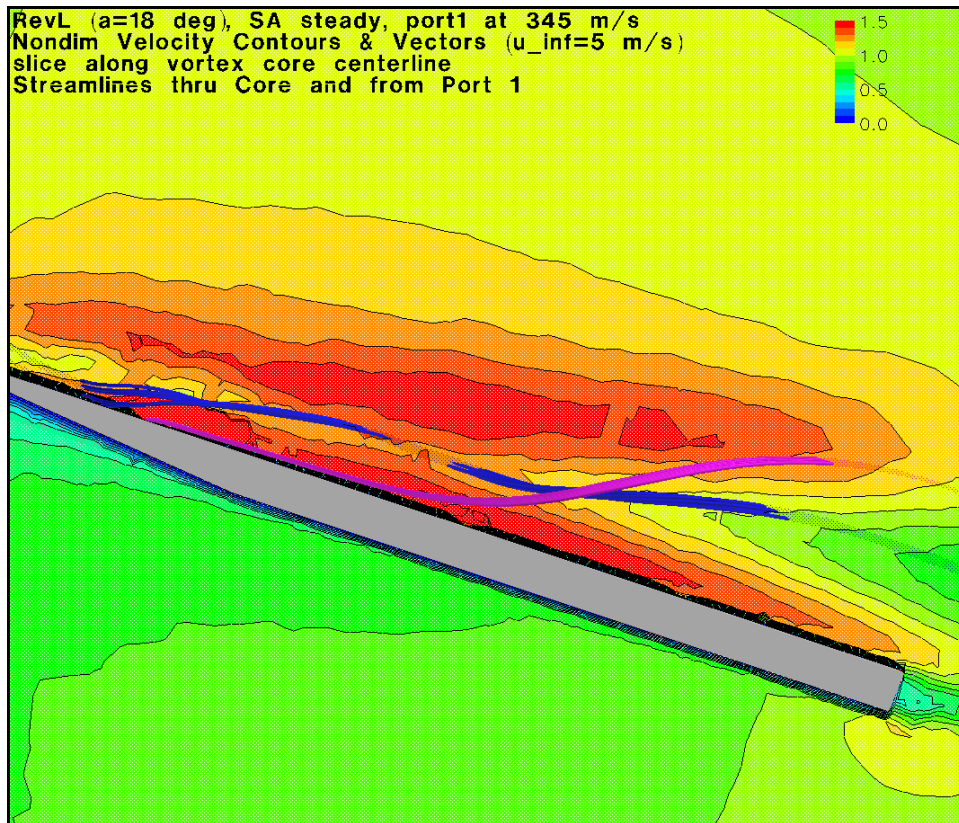


Figure 4.10 – Port 1 Sonic Blowing for $M_{\infty} = 0.01$ (Steady S-A, Revision L, $\alpha = 18^{\circ}$)

low-energy vortex. With this low freestream velocity, it is unlikely that the jet flow was overwhelmed by the vortical structure; this is perhaps a greater indication that the jet's boundary conditions were inadequately specified or that the numerical mesh in the region of blowing was not sufficiently refined. Hence, additional investigation into the jet blowing profile, boundary condition parameters, blowing region mesh refinement to include resolution for LES and secondary vortex is merited.

Thus no three-dimensional attempts in this numerical study successfully predicted delay of vortex breakdown from along-core blowing into the vortex.

V. Conclusions

Final Configuration

The final numerical mesh for this study (Mesh Revision L) modeled the half delta wing mounted at $\alpha = 18^\circ$, flush against a boundary layer refresher plate, which was flush against the wind tunnel wall. The numerical or virtual wind tunnel maintained the same dimensions as the test section of the tunnel used during testing and data generation at the University of Cincinnati. The wing's angle of attack, which was reported to be 15° during physical testing, was increased in the numerical model to give better correlation between its predicted solution and experimental data. This study has shown that there was likely error in the reported α . Freestream velocity for the numerical study was 16 m/s, which was increased within an acceptable tolerance of the reported $V_\infty = 15.4$ m/s in an effort to improve data correlation. The physical boundary layer refreshing plate was offset by 1.27 cm from the tunnel wall, but this study showed that it was acceptable to make the computationally simplifying assumption of placing it flush against the tunnel wall.

Numerical results were investigated and compared using FLUENT Version 6.0.20's steady and unsteady, second-order accurate flow solvers, and the following flow models: inviscid, laminar, and turbulence models, Spalart-Allmaras (S-A), Renormalization Group k- ϵ , Reynolds Stress (RSM), and Large Eddy Simulation (LES). While used preliminarily, the LES model resulted in an unacceptable solution because the numerical mesh was inadequately refined for the LES wall y^+ requirement.

Conclusions

This study revealed no combination of FLUENT flow solver and turbulence model that predicted a completely acceptable or adequate solution. Time averaged solutions generally converged within hours and predicted quantitative results relatively close to experimental data, but they did not predict most of the unsteady characteristics of vortical flow and vortex breakdown. Time accurate solutions attained fully developed flow typically within a couple weeks and only the RSM turbulence model predicted some of the unsteady flow physics; further, their quantitative predictions were not an improvement over those of the steady solver. Regarding flow models in unsteady and/or steady time, laminar, k- ϵ , RSM and LES each predicted vortex breakdown but not to an acceptable quantitative degree for vortex size and strength; the S-A turbulence model gave relatively close quantitative prediction of the solution but failed to predict vortex breakdown. A recent numerical study also confirmed that the S-A model failed to predict vortex breakdown; however, that study also revealed that modifications to the S-A model, which cater to flow issues associated with vortex breakdown, did successfully predict the highly unsteady phenomenon (Morton, Forsythe, Mitchell, Hajek, 2002). Those modified S-A models are not currently available in FLUENT.

No three-dimensional numerical case, regardless of flow solver, turbulence model or freestream velocity, successfully controlled or in any way affected vortex breakdown. This was due to one or all of the following: along-core jet blowing momentum was numerically overwhelmed by momentum of the primary vortex; boundary condition for the jet was inadequately specified and resulted in rapid dissipation into the vortex

structure; or the numerical grid in the regions of blowing was insufficiently refined to prevent the rapid blowing dissipation.

The numerical grid used for the majority of cases predicted solutions adequate for comparative analysis. However, the mesh was not sufficiently refined to give optimal solutions, particularly in the regions over the forward half of the delta wing, along the wing's leading edge, within and immediately surrounding the primary vortex, and in the regions of jet blowing.

A likely candidate for most of the numerical problems in this study was the wing mounted flush against the tunnel wall. Since there were no data for comparison, no numerical study was performed with a full wing model inside the wind tunnel. That would eliminate impact of boundary layer flow on vortex generation and breakdown and is the current focus of wind tunnel research at UC.

Future Work

Using a numerical mesh or developing a full wing numerical model with greater resolution in the regions mentioned above, one option for future work is to use a different flow solver software, such as Cobalt. Two numerical studies of a delta wing at high angle of attack have obtained solutions with Cobalt which compared closely to experimental data and which adequately predicted the unsteady properties of vortex breakdown (Cummings, Morton, Siegel, 2003; Morton, Forsythe, Mitchell, Hajek, 2002). Another option is to develop three-dimensional CFD code specific to this problem and which implements one of the modified S-A transport solvers suggested by Morton et al.

If better computational resources become available, a DNS solver would be best, but that is likely not a reasonable option for many years hence.

If work is to continue with the FLUENT flow solver, following are some recommendations. Develop a full delta wing computational model, including wind tunnel geometry for wall effects; UC experimental data for comparison should be available within the year. Refine the numerical mesh for compatibility with the unsteady LES turbulence model and divide the computational load among a sufficient number of processors to generate a solution within a reasonable amount of time. Investigate FLUENT's other turbulence models – Realizable k- ϵ , Standard and Shear-Stress Transport k- ω , and LES with RNG-Based Sub-Grid Scale model (FLUENT, 2001: 10.4.3, 10.5.1-2, 10.7.2). Dynamic maneuvering through a number of angles of attack may be simulated by creating a user-defined function for the pressure farfield boundary condition (refer to *FLUENT 6.0 UDF Manual*); this would require modeling the wing at $\alpha = 0^\circ$ with a farfield boundary. As part of troubleshooting the blowing cases, create a user-defined function for the velocity profile at the blowing port boundaries, giving it the more correct parabolic form; consider significantly greater refinement of the numerical mesh in the blowing regions; and conduct more research into blowing jet boundary conditions.

Appendix A: Experimental Data

Following are the tabulated experimental data obtained during wind tunnel testing at University of Cincinnati (UC). Ambient conditions were reported at $T = 25^\circ \text{ C}$ (298 K) and $p = 29.4 \text{ in. Hg}$ (99.56 kPa). Wing $\alpha = 15^\circ$ and $V_\infty = 15.4 \text{ m/s}$. Baseline data, without along-core blowing, were sampled at 100 Hz for a period of 5 sec then averaged for the values in Table A.1. As no numerical model predicted the effects of along-core blowing into the vortex core, those corresponding experimental data are not provided.

Table A.1 – Baseline C_p Data over Wing Surface, No Blowing

x/c	y/s	sensor	static P (Pa)	dyn P (Pa)	C_p
0.35	0.15	1	-58.516	139.683	0.419
	0.17	2	-67.633	139.993	0.483
	0.19	3	-97.310	139.886	0.696
	0.20	4	-166.452	139.886	1.190
	0.22	5	-273.960	140.121	1.955
	0.25	6	-314.272	140.110	2.243
0.55	0.25	7	-43.956	140.228	0.313
	0.29	8	-61.847	140.345	0.441
	0.31	9	-99.160	140.665	0.705
	0.33	10	-169.803	140.313	1.210
	0.36	11	-232.605	140.750	1.653
	0.39	12	-229.654	141.775	1.620
	0.41	13	-212.346	140.857	1.508
	0.43	14	-195.944	141.113	1.389
0.75	0.35	15	-34.196	141.487	0.242
	0.41	17	-86.265	141.081	0.611
	0.45	18	-133.785	141.839	0.943
	0.48	19	-173.874	141.668	1.227
	0.51	20	-181.919	141.263	1.288
	0.55	21	-162.829	141.850	1.148
	0.58	22	-139.113	141.199	0.985
0.95	0.41	23	-37.118	141.540	0.262
	0.45	24	-46.050	142.074	0.324
	0.50	25	-64.438	141.807	0.454
	0.54	26	-83.499	141.529	0.590
	0.58	27	-100.232	142.138	0.705
	0.62	28	-108.530	142.010	0.764
	0.66	29	-107.235	141.924	0.756
	0.70	30	-93.804	142.362	0.659

Since the dynamic pressure appeared to fluctuate in these data, the C_P values were normalized for comparison with computational data by providing a constant dynamic pressure, based on lab ambient density and tunnel freestream velocity – such that dynamic pressure became 143.206 Pa. Table A.2 shows the data which were then used to compare with numerically predicted values.

Table A.2 – Normalized Baseline C_P Data over Wing Surface, No Blowing

x/c	y/s	sensor	static P (Pa)	dyn P (Pa)	C_P
0.35	0.15	1	-58.516	143.206	0.409
	0.17	2	-67.633	143.206	0.472
	0.19	3	-97.310	143.206	0.680
	0.20	4	-166.452	143.206	1.162
	0.22	5	-273.960	143.206	1.913
	0.25	6	-314.272	143.206	2.195
0.55	0.25	7	-43.956	143.206	0.307
	0.29	8	-61.847	143.206	0.432
	0.31	9	-99.160	143.206	0.692
	0.33	10	-169.803	143.206	1.186
	0.36	11	-232.605	143.206	1.624
	0.39	12	-229.654	143.206	1.604
	0.41	13	-212.346	143.206	1.483
	0.43	14	-195.944	143.206	1.368
0.75	0.35	15	-34.196	143.206	0.239
	0.41	17	-86.265	143.206	0.602
	0.45	18	-133.785	143.206	0.934
	0.48	19	-173.874	143.206	1.214
	0.51	20	-181.919	143.206	1.270
	0.55	21	-162.829	143.206	1.137
	0.58	22	-139.113	143.206	0.971
0.95	0.41	23	-37.118	143.206	0.259
	0.45	24	-46.050	143.206	0.322
	0.50	25	-64.438	143.206	0.450
	0.54	26	-83.499	143.206	0.583
	0.58	27	-100.232	143.206	0.700
	0.62	28	-108.530	143.206	0.758
	0.66	29	-107.235	143.206	0.749
	0.70	30	-93.804	143.206	0.655

Appendix B: Traub's Simple Prediction of Vortex Breakdown Location

Following is Traub's sequence of equations used to predict location of vortex breakdown. Since this model is based upon curve-fitting to experimental data for delta wings with sweep angle, $\Lambda = 65, 70, 75$ and 80° , the results in this case for $\Lambda = 60^\circ$ were only valid for ensuring the predicted results were within an acceptable range or "ballpark" estimate of what they should be (Traub, 1996).

The first of three steps was to determine α_{BD-TE} , the angle of attack for a delta wing at which vortex breakdown occurs at the trailing edge:

$$\tan \alpha_{BD-TE} = 13.47 \cdot \tan \varepsilon \cdot e^{-6.9 \cdot \varepsilon} \quad (\text{B.1})$$

where ε is *wing apex half angle* or 0.5Λ . For $\Lambda = 60^\circ$, $\alpha_{BD-TE} = 11.848^\circ$.

Second, the nondimensional circulation must be determined. It is defined as

$$\frac{\Gamma}{V_\infty \cdot c_r} = 4.63 \cdot \tan^{0.8} \varepsilon \cdot \tan^{1.2} \alpha \cdot \cos \alpha \quad (\text{B.2})$$

where Γ is *circulation*, α is *wing angle of attack*, c_r is *wing root chord length*, and V_∞ is *freestream velocity*. This nondimensional quantity must be determined using $\alpha = \alpha_{BD-TE}$, as well as using the angle of attack of interest. For the α_{BD-TE} determined above and for $\alpha = 15$ and 18° , the nondimensional circulation values become 0.44824, 0.59339 and 0.73633, respectively.

Finally, the predicted breakdown location is determined by

$$\left(\frac{x}{c_r}\right)_{BD} = \left(\frac{\Gamma_{BD-TE}}{\Gamma_{\alpha>BD-TE}}\right)^n \quad (\text{B.3})$$

where n is an empirically determined curve-fit constant. Traub used $n = 3$ to fit the data for $\Lambda = 65^\circ$, so that value was also used for this case with $\Lambda = 60^\circ$. Thus the final answer or predicted locations for vortex breakdown for $\Lambda = 60^\circ$ at $\alpha = 15$ and 18° were 0.431 and 0.226, respectively.

Appendix C: Gridgen Lessons

Following are some lessons learned from creating a numerical mesh using the Gridgen software and from interfacing Gridgen and FLUENT. One, the user must follow the default directional indicators in the graphical user interface display when selecting lines to create borders for a domain, else it may result in a negative volume for the associated block; FLUENT will not accept a mesh with negative volumes. An exception to this is for creating a domain with an embedded form, where the user must select lines in the direction opposite to that used for the domain exterior. Two, when declaring boundary conditions for a problem with confined flow, if any of them are inflow (e.g., pressure gradient, velocity, or mass flow rate, and not farfield pressure), the exit must be an outlet (pressure, velocity, or mass flow) rather than a simple outflow condition. Three, when interfacing structured and unstructured volumes, Gridgen creates “Type I” boundaries by default; the user should not specify/change that boundary condition to be an interface, else FLUENT will not correctly import it.

Last, if two or more boundaries within a given block have the same boundary condition, FLUENT will automatically group them, such that they must then have the same initial condition. For example, if two blowing jets on the wing surface are specified as velocity inlet boundary conditions, they must both be active or inactive, both have the same blowing angle and velocity, and so on. Similarly for another example, if the wing and tunnel walls are all specified with a wall boundary condition, FLUENT will group them and compute quantities such as C_L and C_D based on the entire surface area and not just the wing. To avoid this pitfall, in Gridgen the user must specify related but different

boundary conditions for any boundary that needs to be distinct; then in FLUENT, the user may specify/change those boundaries to what they need to be.

Appendix D: Matrix of Transformation to Determine Jet Blowing Angles

Following is the development of the matrix of transformation used to determine correct blowing angles for the momentum jets on the half delta wing's upper surface. This transformation allows for any variation in orientation of the wing or its blowing jets. The matrix in Equation D.1 uses Euler angles for yaw (ψ), pitch (θ) and roll (ϕ) to transform body (wing) reference frame to a Cartesian fixed reference frame (in that order of rotation), which is then used as FLUENT boundary conditions for the blowing jets.

$$\begin{bmatrix} \dot{x}_f \\ \dot{y}_f \\ \dot{z}_f \end{bmatrix} = [A] \cdot \begin{bmatrix} u \\ v \\ w \end{bmatrix} \quad (\text{D.1})$$

where \dot{x}_f , \dot{y}_f and \dot{z}_f are fixed reference Cartesian velocity components, A is defined as

$$\begin{bmatrix} \cos\theta \cdot \cos\psi & \sin\phi \cdot \sin\theta \cdot \cos\psi - \cos\phi \cdot \sin\psi & \cos\phi \cdot \sin\theta \cdot \cos\psi + \sin\phi \cdot \sin\psi \\ \cos\theta \cdot \sin\psi & \sin\phi \cdot \sin\theta \cdot \sin\psi + \cos\phi \cdot \cos\psi & \cos\phi \cdot \sin\theta \cdot \sin\psi - \sin\phi \cdot \cos\psi \\ -\sin\theta & \sin\phi \cdot \cos\theta & \cos\phi \cdot \cos\theta \end{bmatrix} \quad (\text{D.2})$$

and u , v and w are *three-dimensional components of the blowing velocity* defined by

$$u = -V_{jet} \cdot \cos\theta_{el} \cdot \cos\theta_{az} \quad (\text{D.3})$$

$$v = V_{jet} \cdot \cos\theta_{el} \cdot \sin\theta_{az} \quad (\text{D.4})$$

$$w = -V_{jet} \cdot \sin\theta_{el} \quad (\text{D.5})$$

where V_{jet} is *velocity magnitude of blowing jet*, θ_{el} is *elevation angle of blowing jet*, and θ_{az} is *azimuthal angle of blowing jet* (measured counter-clockwise from a line parallel to the wing's root, as shown in Figure 2.2); the blowing jets were physically limited to variation in these two degrees of freedom. Equation D.2 came from Nelson (1998: 102). Combining Equations D.1-5 gives the necessary Cartesian jet blowing components.

For this case, $\phi = \psi = 0^\circ$, and **pitch angle θ was negative**, due to orientation of the wing's coordinate axes. Thus Equations D.1-5 simplify to

$$\begin{bmatrix} \bullet \\ x_f \\ \bullet \\ y_f \\ \bullet \\ z_f \end{bmatrix} = V_{jet} \cdot \begin{bmatrix} -\cos\theta \cdot \cos\theta_{el} \cdot \cos\theta_{az} - \sin\theta \cdot \sin\theta_{el} \\ \cos\theta_{el} \cdot \sin\theta_{az} \\ \sin\theta \cdot \cos\theta_{el} \cdot \cos\theta_{az} - \cos\theta \cdot \sin\theta_{el} \end{bmatrix} \quad (D.6)$$

Bibliography

Cummings, Russell M., Scott A. Morton and Stefan G. Siegel. "Computational Simulation and PIV Measurements of the Laminar Vortical Flowfield for a Delta Wing at High Angle of Attack," AIAA Paper 2003-1102, Reno NV: American Institute of Aeronautics and Astronautics, January 2003.

Ekaterinaris, J. A. and Lewis B. Schiff. "Numerical Simulation of the Effects of Variation of Angle of Attack and Sweep Angle on Vortex Breakdown over Delta Wings," AIAA Paper 90-3000-CP, CA: American Institute of Aeronautics and Astronautics, 1990.

Faler, J. H. and Sidney Leibovich. "Disrupted States of Vortex Flow and Vortex Breakdown," *The Physics of Fluids*, Vol. 20 No. 9, September 1977, p. 1385-1399.

FLUENT Incorporated, Lebanon, NH. *FLUENT 6.0 User's Guide*. CD-ROM documentation with FLUENT Version 6.0 software, December 2001.

Guillot, Stephen A. *Flow Control for Highly Swept Wings at High Angle of Attack*. MS Thesis, Louisiana State University, May 1999.

Gutmark, Ephraim J., J. Jim Zhu, Douglas A. Lawrence and David R. Jacques. "High Angle of Attack Flight Control of Delta Wing Aircraft Using Vortex Actuators," Army-NASA Workshop on Advances in GNC Technology, Huntsville AL, November 2000.

Hoerner, Sighard F. and Henry V. Borst. *Fluid-Dynamic Lift* (Second Edition), Chapter 18. Albuquerque NM: Mrs. Liselotte A. Hoerner, 1985.

Hoffman, Klaus A. and Steve T. Chiang. *Computational Fluid Dynamics* (Fourth Edition), Vol. I. Wichita KS: Engineering Education System, August 2000.

----- *Computational Fluid Dynamics* (Fourth Edition), Vol. II. Wichita KS: Engineering Education System, August 2000.

----- *Computational Fluid Dynamics* (Fourth Edition), Vol. III. Wichita KS: Engineering Education System, August 2000.

Intelligent Light. *FIELDVUE Release 8.0 User's Guide*. Lyndhurst NJ: Intelligent Light, November 2001.

Johari, H., D. J. Olinger and K. C. Fitzpatrick. "Delta Wing Vortex Control via Recessed Angled Spanwise Blowing," *Journal of Aircraft*, Vol. 32 No. 4, July-August 1995, p. 804-810.

Kral, L. D. "Recent Experience with Different Turbulence Models Applied to the Calculation of Flow over Aircraft Components," *Progress in Aerospace Sciences*, Vol. 34 No. 7-8, November-December 1998, p. 481-541.

Kral, L. D., Mori Mani and John A. Ladd. "Application of Turbulence Models for Aerodynamic and Propulsion Flowfields," *AIAA Journal*, Vol. 34 No. 11, November 1996, p. 2291-2298.

Kuethe, Arnold M. and Chuen-Yen Chow. *Foundations of Aerodynamics: Bases of Aerodynamic Design* (Fifth Edition), Chapter 19. New York: John Wiley & Sons, Inc., 1998.

Leibovich, Sidney. "The Structure of Vortex Breakdown," *Annual Review of Fluid Mechanics*, Vol. 10, 1978, p. 221-246.

Mani, Mori, P. Willhite and John A. Ladd. "Performance of One-Equation Turbulence Models in CFD Applications," AIAA Paper 95-2221, San Diego CA: American Institute of Aeronautics and Astronautics, June 1995.

Mathieu, Jean and Julian Scott. *An Introduction to Turbulent Flow*. Cambridge UK: Cambridge University Press, 2000.

May, Cameron(a). Test Engineer and Graduate Student, University of Cincinnati OH. Personal Electronic Correspondence. 26 August 2002.

-----(b). Test Engineer and Graduate Student, University of Cincinnati OH. Personal Electronic Correspondence. 14 November 2002.

-----(c). Test Engineer and Graduate Student, University of Cincinnati OH. Telephone Conversation. 4 November 2002.

Mitchell, Anthony M. and Jean Détery. "Research into Vortex Breakdown Control," *Progress in Aerospace Studies*, Vol. 37, 2001, p. 385-418.

Morton, Scott, James Forsythe, Anthony Mitchell and David Hajek. "DES and RANS Simulations of Delta Wing Vortical Flows," AIAA Paper 2002-0587, American Institute of Aeronautics and Astronautics, 2002.

Murayama, Mitsuhiro, Kazuhiro Nakahashi and Keisuke Sawada. "Simulation of Vortex Breakdown Using Adaptive Grid Refinement with Vortex-Center Identification," *AIAA Journal*, Vol. 39 No. 7, July 2001, p. 1305-1312.

Nelson, Robert C. *Flight Stability and Automatic Control* (Second Edition). Boston MA: McGraw-Hill, 1998.

Novak, F. and T. Sarpkaya. "Turbulent Vortex Breakdown at High Reynolds Numbers," AIAA Paper 99-0135, Reno NV: American Institute of Aeronautics and Astronautics, January 1999.

Office National d'Etudes et Recherches Aéronautiques. Image showing vortex breakdown over delta wing. <http://www.gj.net/~nmasters/vortex-lift/delta.html>.

O'Neil, P. J., F. W. Roos, R. M Barnett and J. D. Hawk. "Investigation of Flow Characteristics of Developed Vortex," McDonnell Aircraft Company Report, NADC-89114-60, 1989.

Polhamus, Edward C. "A Concept of the Vortex Lift of Sharp-Edged Delta Wings Based on a Leading-Edge Suction Analogy," NASA Technical Notes, TN-D3767, December 1966.

----- "Predictions of Vortex Lift Characteristics by a Leading-Edge Suction Analogy," *Journal of Aircraft*, Vol. 8 No. 4, November 1971, p. 193-199.

Rusak, Zvi and David Lamb. "Prediction of Vortex Breakdown in Leading Edge Vortices Above Slender Delta Wings," AIAA Paper 98-2860, Albuquerque NM: American Institute of Aeronautics and Astronautics, June 1998.

Seginer, A. and M. Salomon. "Performance Augmentation of a 60-Degree Delta Aircraft Configuration by Spanwise Blowing," *Journal of Aircraft*, Vol. 23 No. 11, November 1986.

Snyder, Deryl O. and Robert E. Spall. "Numerical Investigation into Multiple Vortex Structures Formed over Flat End-Cap Wings," *AIAA Journal*, Vol. 38 No. 8, August 2000, p, 1486-1489.

Spalart, P. R. and S. R. Allmaras. "A One-Equation Turbulence Model for Aerodynamic Flows," AIAA Paper 92-0439, Reno NV: American Institute of Aeronautics and Astronautics, January 1992.

The Holy Bible, King James Version. Salt Lake City UT: The Church of Jesus Christ of Latter-day Saints, 1979.

Traub, Lance W. "Simple Prediction Method for Location of Vortex Breakdown on Delta Wings," *Journal of Aircraft*, Vol. 33 No. 2, March-April 1996, p. 452-454.

U.S. Government Printing Office. *U.S. Standard Atmosphere, 1976*. Technical Report, 1976. <http://aero.stanford.edu/StdAtm.html>.

Versteeg, H.K. and W. Malalasekera. *An Introduction to Computational Fluid Dynamics: The Finite Volume Method*. Essex, England: Longman Scientific & Technical, 1995.

Wentz, W.H. Jr. and D.L. Kohlman. "Vortex Breakdown on Slender Sharp-Edged Wings," *Journal of Aircraft*, Vol. 8 No. 3, March 1971, p. 156-161.

Vita

Captain Jacob A. Freeman graduated from Harry S Truman High School in Independence, Missouri. He entered undergraduate studies at Brigham Young University (BYU) in Provo, Utah, and graduated with a Bachelor of Science degree in Mechanical Engineering in December 1997. He was commissioned a US Air Force officer through Detachment 855 AFROTC at BYU.

Capt Freeman's first assignment was at Kirtland AFB, New Mexico, as a satellite engineer and launch and mission operations manager for the MightySat Program, Space Vehicles Directorate, Air Force Research Laboratory (AFRL). In September 2001, he was assigned to Wright-Patterson AFB, Ohio, as a graduate student in the Aeronautical Engineering program, Air Force Institute of Technology. Upon graduation, he will be assigned to AFRL's Munitions Directorate at Eglin AFB, Florida.

REPORT DOCUMENTATION PAGE

Form Approved
OMB No. 074-0188

The public reporting burden for this collection of information is estimated to average 1 hour per response, including the time for reviewing instructions, searching existing data sources, gathering and maintaining the data needed, and completing and reviewing the collection of information. Send comments regarding this burden estimate or any other aspect of the collection of information, including suggestions for reducing this burden to Department of Defense, Washington Headquarters Services, Directorate for Information Operations and Reports (0704-0188), 1215 Jefferson Davis Highway, Suite 1204, Arlington, VA 22202-4302. Respondents should be aware that notwithstanding any other provision of law, no person shall be subject to a penalty for failing to comply with a collection of information if it does not display a currently valid OMB control number.

PLEASE DO NOT RETURN YOUR FORM TO THE ABOVE ADDRESS.

1. REPORT DATE (DD-MM-YYYY) 25-03-2003		2. REPORT TYPE Master's Thesis		3. DATES COVERED (From - To) Jul 2002 - Mar 2003	
4. TITLE AND SUBTITLE COMPUTATIONAL FLUID DYNAMICS INVESTIGATION OF VORTEX BREAKDOWN FOR A DELTA WING AT HIGH ANGLE OF ATTACK				5a. CONTRACT NUMBER	
				5b. GRANT NUMBER	
				5c. PROGRAM ELEMENT NUMBER	
				5d. PROJECT NUMBER	
				5e. TASK NUMBER	
5f. WORK UNIT NUMBER		8. PERFORMING ORGANIZATION REPORT NUMBER AFIT/GAE/ENY/03-3			
7. PERFORMING ORGANIZATION NAMES(S) AND ADDRESS(S) Air Force Institute of Technology Graduate School of Engineering and Management, Bldg 640 2950 Hobson Way WPAFB OH 45433-7765					
9. SPONSORING/MONITORING AGENCY NAME(S) AND ADDRESS(ES) Dr James Myatt AFRL/VACA, Bldg 146 2210 8 th Street DSN 785-8491 WPAFB OH 45433 (937) 255-8491				10. SPONSOR/MONITOR'S ACRONYM(S)	
				11. SPONSOR/MONITOR'S REPORT NUMBER(S)	
12. DISTRIBUTION/AVAILABILITY STATEMENT APPROVED FOR PUBLIC RELEASE; DISTRIBUTION UNLIMITED.					
13. SUPPLEMENTARY NOTES					
14. ABSTRACT Using the commercially available FLUENT 3-D flow field solver, this research effort investigated vortex breakdown over a delta wing at high angle of attack (α) in preparation for investigation of active control of vortex breakdown using steady, along-core blowing. A flat delta-shaped half-wing with sharp leading edge and sweep angle of 60° was modeled at $\alpha = 18^\circ$ in a wind tunnel at Mach 0.04 and Reynolds number of 3.4×10^5 . A hybrid numerical mesh was generated to accommodate blowing ports on the wing surface. Results for cases without and with along-core blowing include comparison of various turbulence models for predicting both flow field physics and quantitative flow characteristics. FLUENT turbulence models included Spalart-Allmaras, RNG k- ϵ , Reynolds Stress, and Large Eddy Simulation (LES), as well as comparison with laminar and inviscid models. Mesh independence was also investigated, and solutions were compared with experimentally determined results and theoretical prediction. These research results show that, excepting the LES model for which the computational mesh was insufficiently refined, none of the turbulence models above, as implemented with the given numerical grid, generated a solution which was suitably comparable to the experimental data. Much more work is required to find a suitable combination of numerical grid and turbulence model.					
15. SUBJECT TERMS Vortex Breakdown, Computational Fluid Dynamics, Turbulence Models, Delta Wing at High Angle of Attack, Control of Vortex Breakdown					
16. SECURITY CLASSIFICATION OF:		17. LIMITATION OF ABSTRACT	18. NUMBER OF PAGES	19a. NAME OF RESPONSIBLE PERSON	
a. REPORT	b. ABSTRACT	c. THIS PAGE	UU	Montgomery C. Hughson, Lt Col, USAF (ENY)	
U	U	U	172	19b. TELEPHONE NUMBER (Include area code) (937) 255-3636 ext 4597	

Standard Form 298 (Rev. 8-98)
Prescribed by ANSI Std. Z39-18

Form Approved
OMB No. 074-0188